공학박사 학위논문

Functional Improvement on Rotational Modulation Collimator Technique for Dual-particle Imaging Capability and Extended Field of View

이중 입자 영상화와 시야각 확대를 통한 회전 변조 집속기 영상화 기법 개선

2019년 8월

서울대학교 융합과학기술대학원

융합과학부 방사선융합의생명전공

김 현 석

Ph. D. Dissertation in Engineering

Functional Improvement on Rotational Modulation Collimator Technique for Dual-particle Imaging Capability and Extended Field of View

이중 입자 영상화와 시야각 확대를 통한 회전 변조 집속기 영상화 기법 개선

August 2019

Hyun Suk Kim

Program in Biomedical Radiation Sciences,
Department of Transdisciplinary Studies,
Graduate School of Convergence Science and Technology,
Seoul National University

ABSTRACT

Functional Improvement on Rotational Modulation Collimator Technique for Dual-particle Imaging Capability and Extended Field of View

Hyun Suk Kim
Program in Biomedical Radiation Sciences
Graduate School of Convergence Science and Technology
Seoul National University

Rotational modulation collimator (RMC) is one of the radiation imaging techniques that make use of mechanical collimation, and it comprises a single detector placed behind two rotating collimator masks. This technique has the advantage of eliminating the need for position-sensitive radiation detectors, offering the possibility of reducing the system complexity and cost. However, the limitations of the existing RMC technique are that it 1) only has single-particle imaging and its 2) narrow field of view (FOV) is determined by the aspect ratio of the cylinder. The objective of this dissertation is to further investigate an RMC technique for localization of the radioactive materials, and it has mainly been improved along the following two viewpoints. First, dual-particle localization system was developed based on RMC coupled with a pulse shape discrimination (PSD) capable scintillator. The design parameters for

RMC system were optimized using Monte Carlo (MC) simulations. To remove the 180° source ambiguity imposed by the conventional bilateral symmetric mask, a new slit and slat design of the mask was proposed. The method for estimating the location of radioactive materials was established using the maximum likelihood expectation maximization (MLEM) algorithm, and the imaging capability of the developed system was verified via measurement experiments. It offered an angular resolution 0.95° and FOV of 18° in the cross-sectional plane. Second, to overcome the limited FOV, a hemispherical collimator was developed to extend the FOV to approximately 2π. The design parameters were optimized using MC simulations, and MLEM algorithm was applied to estimate the radiation distribution. Experiments were conducted to evaluate the imaging capability of the system. The proposed hemispherical collimator was shown to be valid as designed and simulated, and it offered an FOV of 160° in the cross-sectional plane and an angular resolution of 10°. In conclusion, the RMC technique was improved from single particle localization to a dual-particle system, and method to extend the FOV approximately 2π was proposed. If these functional improvements are applied to the RMC technique, it could realize more practical and useful applications in the field of radiation safety and nuclear security.

Keywords: Rotational Modulation Collimator, Localization of Neutron/Gamma-ray Sources, Pulse Shape Discrimination, Hemispherical Rotational Modulation Collimator, Maximum Likelihood Expectation Maximization

Student Number: 2013-23762

TABLE OF CONTENTS

LIST OF TABLES

LIST OF FIGURES

LIST OF ABBREVIATIONS

BPE	Borated polyethylene
CLYC	Cs_2LiYCl_6:Ce
CZT	Cadmium zinc telluride (CdZnTe)
FOV	Field of view
H-RMC	Hemispherical rotational modulation collimator
MC	Monte Carlo
MCNP	Monte Carlo N-Particle
MCNP6.1	Monte Carlo N-Particle version 6.1
MLE	Maximum likelihood estimation
MLEM	Maximum likelihood expectation maximization
Pb	lead
PSD	Pulse shape discrimination
RMC	Rotational modulation collimator
RMSD	Root mean square deviation
SNR	Signal-to-noise ratio
SSIM	Structural similarity
2-D	Two dimensional

Chapter 1. Introduction

1.1. Image-based Radioactive Material Detection Technique

There has been a worldwide increase in general interest and concern around radioactive leaks since the Fukushima nuclear power plant disaster in 2011, which led to an increase in demand for technologies to detect radioactivity or radioactive materials [1-5]. The conventional way to detect radioactive materials is to measure radiation from radioactive materials using a survey meter or a radiation detector. These methods, however, only reveal the presence of radioactivity and do not indicate the precise location of radioactive materials. In addition, if the measured values are not changed even when the positions of radioactive materials are changed or moved, there is a possibility that the position change of the radioactive materials will not be detected and the hotspots' presence may be overlooked. Additionally, to quantify the radiation distribution over a wide spatial range, numerous repeated measurements and extensive use of human, material, and time resources are required.

Radiation source detection technology based on radiation distribution images has been actively researched and developed by academia and industry over the past 20 years as a means to assist or replace conventional methods [6-10]. Image-based detection has the advantage of providing radionuclide information

at a distance and mapping the spatial distribution of the radioactivity with a single measurement corresponding to the field of view (FOV) performance of the imaging device. However, in addition to the radiation emitted from the target object, background radiation always exists in the form of noise against the signal, which serves as an obstacle to accurate imaging. Therefore, it is necessary to increase the signal-to-noise ratio by shielding as much background or ineffective radiation as possible, which requires collimation of incident radiation.

1.1.1. Mechanical Collimation Method

The simplest form of imaging equipment using mechanical collimation is a pinhole camera. The basic principle is that the particles emitted from the object are passed through a very small hole and formed on the imaging plate. The angle of incidence on the pinhole differs depending on the position where each particle is emitted, and this appears as a difference in the arrival position of the particles in the detector [8]. H. O. Anger proposes a pinhole camera for obtaining gamma-ray images, also known as an Anger camera, which is the most basic type of gamma-ray imaging equipment [11]. In this method, a position-sensitive detector is required for image acquisition, and the angular resolution of the imaging system is determined by the spatial resolution of the

detector. There is a limit to the image acquisition due to the low detection efficiency.

To improve the detection efficiency of pinhole cameras, a methodology for acquiring images using multiple pinholes has been studied [12-13]. When the number of holes increases, there is a spreading or interference phenomenon of incident particles. This pattern obtained at the detection plate display a certain modulation pattern, and the modulation transfer function can be defined for the imagers. The imaging method using the modulation phenomenon by the collimator can be divided into two major methods. The first is the temporal modulation pattern formed in the time domain; the other is the spatial modulation pattern formed in the spatial domain. The temporal modulation pattern is distributed in the same space instead of being distributed in the time domain, and the spatial modulation pattern is a distribution of the patterns obtained at the same time.

An example of a methodology using temporal modulation is the rotational modulator (RM) [14,15]. An RM consists of a single collimator with slit spacing of the same width over several detector arrays. As the collimator rotates, the incoming radiation is periodically blocked or passed through over time (i.e. depending on the angle of rotation), and the number of particles measured by each detector varies with time. It is possible to reconstruct the image through

the deconvolution process using the correlation with the pre-calculated pattern, which knows the response of the instrument in the form of this modulation pattern in advance.

Conversely, as a representative example of the imaging method using spatial modulation, there is a methodology of imaging using a coded aperture [10,13]. In this method, the particles emitted from the object is projected to the detector through the aperture designed in the collimator, and each aperture acts like the Anger camera mentioned above to obtain the superimposed image. In the case that the hole through which the particles are transmitted has a certain periodicity, the reconstruction of the image through the decoding process using the correlation to the periodicity can reconstruct the radiation image.

Commonly used mask designs for coded apertures are uniformly redundant array (URA), modified uniformly redundant array (MURA), and hexagonal uniformly redundant array (HURA) [16-18]. The feature of the URA patterns is that the pattern of the image incident through the hole is repeatedly projected evenly. In the case of MURA or HURA patterns, it is possible to obtain a decoded pattern by rotating the mask by a certain angle in a pattern considering the process of decoding an image. In the imaging method using spatial modulation, it is important to obtain the spatial distribution of the modulated image pattern as precisely as possible. Therefore, a position-sensitive detector

is required. Depending on the spatial resolution of the detector, the performance of the imaging system is determined.

1.1.2. Electrical collimation method

Electrical collimation is a method of selecting signals necessary for imaging from all the radiation signals incident on a detector using signal processing and analysis techniques without using a separate mechanical collimator. Considering that the measurement efficiency obtained by using mechanical collimation is less than 50%, electrical collimation can be considered more efficient in principle because all the incident radiation is used due to the elimination of the mechanical collimator [14,15]. However, as the incident radiation signal is not separately screened, the effect of background noise is increased as well, and it is not guaranteed that the required event itself always occurs.

In gamma-ray image acquisition, a Compton camera is typically used, and a neutron-scatter camera is typical system for acquiring fast neutron images using a similar principle [19,20]. In Compton imaging, the scattering of primary particles occurs in the first detection plane recording the position and energy of the recoiled electron, and it continues towards the second detection plane where it is absorbed, recording the energy and the position of scattered gamma [9].

The scattered photon causes a second reaction, which transfers some or all of the remaining energy into the detector. At this time, it is possible to localize the origin of the radiation from the measured interaction positions and deposited energies, and each succession of interactions allows creation of a cone of probable source location. The source location can be estimated as the position where these cones overlap each other.

In summary, the above-mentioned imaging systems require a position-sensitive detector, regardless of the collimation method, and the resolution of the imaging device depends on the spatial resolution of the detector. A typical commercial system is a Polaris camera using Compton imaging, and an iPIX camera using coded aperture imaging [21,22]. The main features are presented in the Table 1 below.

Table 1. The main features of the typical commercial imaging system

H400-Polaris (H3D, USA)	- Compton camera imaging technique (using pixelated CdZnTe detector) - FOV 360 (4π) - Angular resolution 30°
iPIx (MIRION, USA)	- Coded aperture imaging technique (using pixelated CdTe detector) - FOV ~48° - Angular resolution 2.5°

1.2. RMC Imaging System

To assist or even replace a traditional survey meter, localization systems should be developed considering three aspects: 1) sensitivity, 2) weight and portability, and 3) cost. However, most of systems require position-sensitive radiation detectors which exist as an array of several detectors or as an internally segmented structure to form a pixelated type device, not only is the system more complex but also the system fabrication is very costly. In terms of simplicity and cost of the system, the RMC technique is an attractive candidate.

The RMC system mainly comprises two concentric collimator masks and radiation detector. This technique, which is based on temporal modulation of incident radiation signals, does not require position-sensitive radiation detectors and thus, excludes the necessity of complex electronics and reduces the fabrication cost. As the RMC rotates, the number of particles detected at each rotational angle changes which modulates the incident radiation that reaches the detector. Using the intensity of incident particles at each rotation angle of the masks, one can obtain a modulation pattern of detector counts in the angular domain, which is used to reconstruct a radiation image (see Figure 1). Thus, it can turn a non-position-sensitive radiation detector into a radiation imaging system.

Although the geometric efficiency for RMC system (~25%, ratio of visible region to total field of view) is relatively low compared to other techniques such as coded aperture (~50%) or Compton camera (~100%), the RMC system can be constructed at a lower cost compared to other systems [14,15]. Deployment of multiple RMCs can drastically increase the detectable area and the overall geometric efficiency is proportional to the number of RMCs deployed. In addition, if multiple RMCs are used, the distance between the radioactive material and the RMC can be estimated more accurately and quickly. Therefore, the RMC system offers an advantage for radiation localization and monitoring compared with other modalities which require expensive position-sensitive detector.

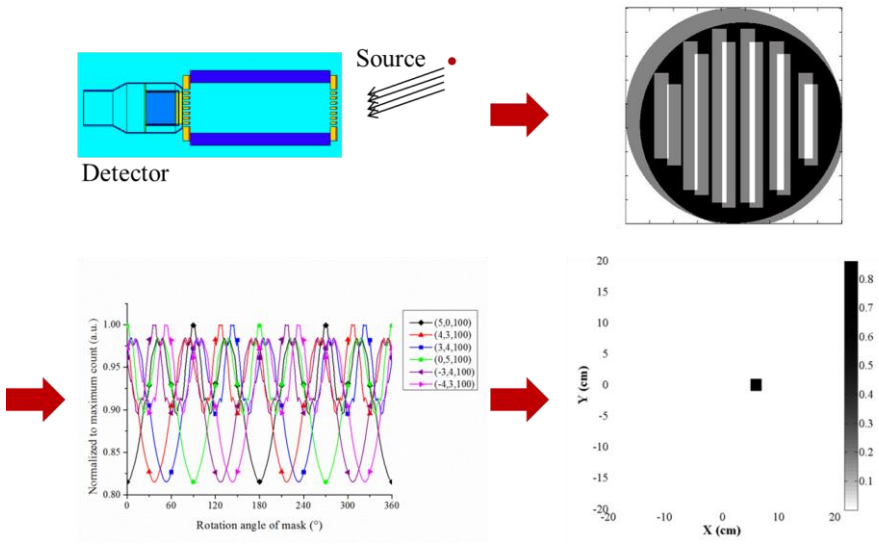

Figure 1. An overview of the RMC imaging technique.

1.2.1. Basic Principle of the RMC Imager

The RMC system estimates the source position based on the difference in the shape of the modulation pattern, the number of ripples, and their shape on the modulation patterns which are in turn determined by the position of the radiation source. For different source positions located at the same distance from the rotation axis, shifting of the modulation patterns in the angular domain was observed [23]. The degree of the rotation of the source to the rotational axis exactly matched the degree of the pattern shift; i.e. there was no difference between the degree of rotation of the source and the degree of pattern shift in the angular domain. The comparison between the rotational degree of source (refer to Figure 2) and modulation pattern shift is shown in Figure 3 and Table 2. In addition, all the modulation patterns have a periodicity of 180° in angular domain due to the bilateral symmetric mask design. Therefore, two sources located symmetrically with respect to the rotation axis will result in exactly the same modulation pattern with each other. Figure 4 shows the concurrence of the modulation pattern between two sources located at the symmetric positions from the rotational axis. Lastly, Figure 5 shows the parallel shift effect of source location from or toward the axis of rotation. The number and the frequency of the ripples in the modulation pattern were increased as the source was placed further away from the rotational axis of masks.

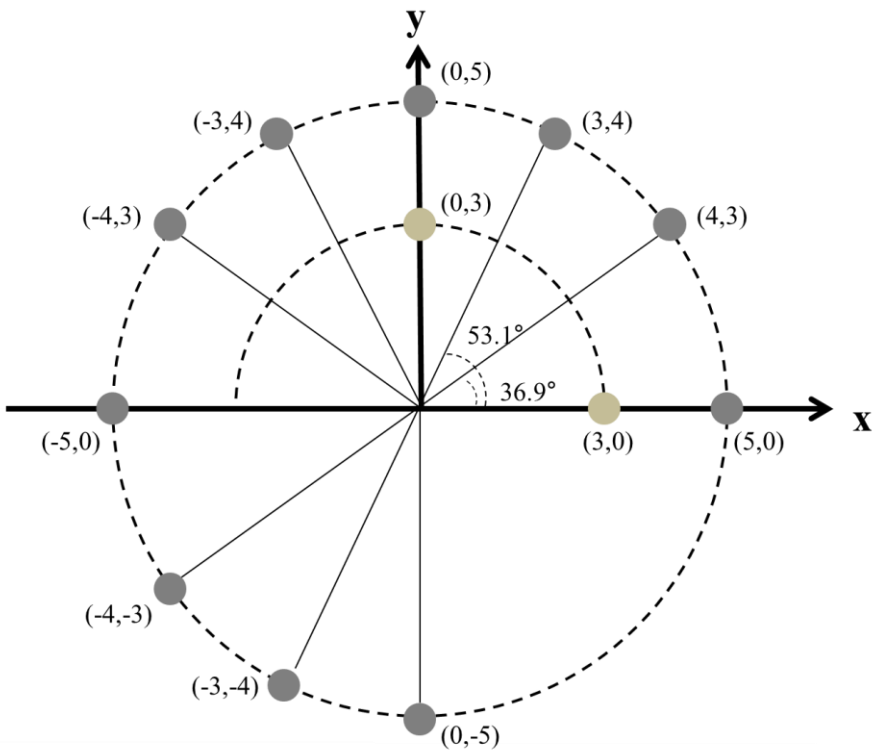

Figure 2. Illustration of source locations simulated to study fundamental characteristic of the modulation pattern.

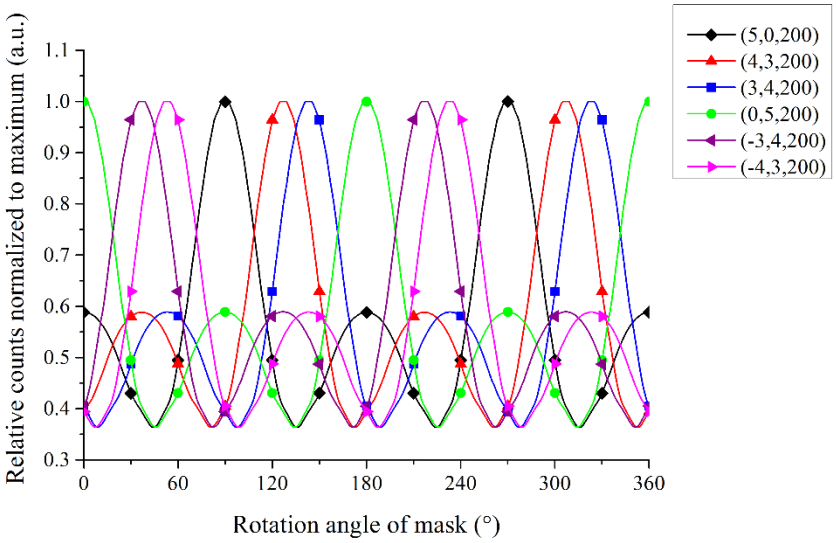

Figure 3. Shifting of modulation patterns in angular domain according to the rotation of source location with respect to the rotational axis of the mask.

Table 2. Comparison between rotation degree of the source and degree of modulation patterns shift

	(5,0,200)	(4,3,200)	(3,4,200)	(0,5,200)	(-3,4,200)	(-4,3,200)
Rotation degree of source	0°	37°	53°	90°	127°	143°
Degree of modulation pattern shift	0°	37°	53°	90°	127°	143°

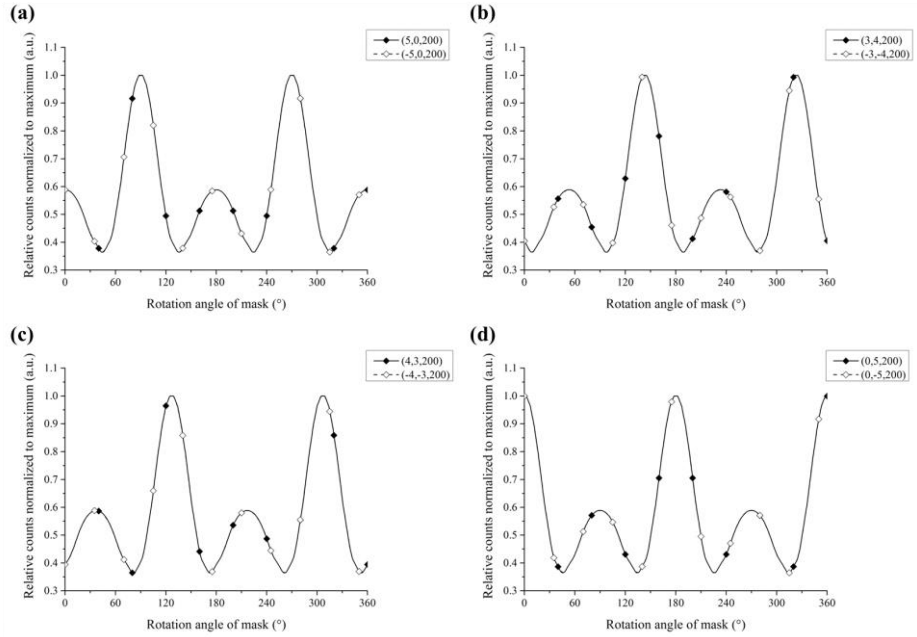

Figure 4. Modulation patterns obtained for pairs of sources located symmetrically at (x,y,z) [cm]: (a) (5,0,200)/(-5,0,200), (b) (3,4,200)/(-3,-4,200), (c) (4,3,200)/(-4,-3,200) and (d) (0,5,200)/(0,-5,200).

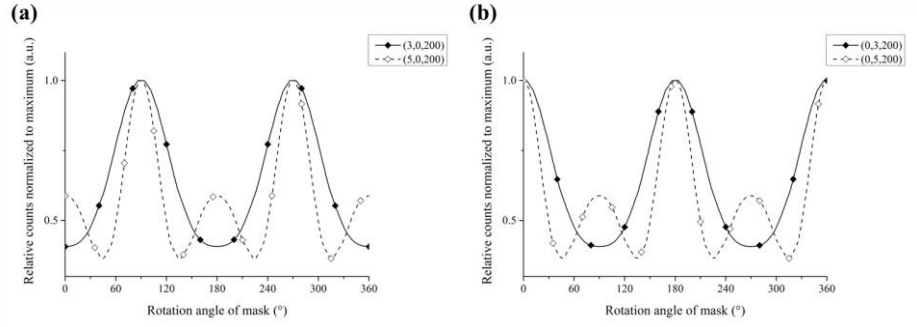

Figure 5. Change in the shape of modulation patterns according to the parallel shift of the source location from or toward the rotational axis of the mask.

1.2.2. Previous Studies of the RMC Technique

RMC technique was first developed by Oda *et al.* to measure space radiation [24]. In the early stages, a single collimator was attached to a rotating sounding rocket or high-altitude balloon. For measurement devices, a Geiger counter and film were used, and scintillation detectors, such as NaI and CsI scintillator, and a gas proportional counter were also used [25-28]. In 1986, Mertz *et al.* proposed a design similar to the current form to obtain the radiation source image from more complex locations [29]. Various lengths of slits and two collimators were used, and specific patterns of the collimators were designed. Fisher *et al.* applied the concept of the Mertz group to the WINKLER spectrometer [30]. WINKLER uses nine independent RMC pairs in high-purity germanium (HPGe) detector with an energy range of 25 keV to 10 MeV and a field of view (FOV) of 20°. The Reuven Ramaty High Energy Solar Spectroscopic Imager (RHESSI) project is the most successful project using RMC, and was designed to provide the same type of high-energy X-ray images that the Sun releases [31]. A total of nine RMC systems were installed in the satellite, and the collimator pattern imitated the WINKLER concept. For each RMC, a high-purity germanium (HPGe) detector was used to generate images related to the solar flare.

Since then, the RMC technique, which was used for far-field imaging in the field of astronomy, has had its application scope expanded to include medical and homeland security since 2000. In 2007, Sharma *et al.* proposed the Neutron Stimulated Emission Computed Tomography (NSECT) using RMC technology and applied it to the medical field. It is a system that distinguishes and quantifies the constituent substances of the human body by irradiating 3-5 MeV fast neutrons in the human body and analyzing gamma rays secondarily emitted in the body by fast neutrons [32]. In 2009, Kowash *et al*. at the University of Michigan developed RMC technique to search for orphan sources [33,34]. Subsequent research has been carried out by Boyce in the United States Air Force Institute of Technology to develop a thermal neutron imaging system using the RMC technique [35]. Wilkox later conducted further research on the collimator mask design and sampling methodology to improve RMC detection efficiency and image quality [36].

In order to solve the intrinsic artifact issue caused by the bilateral symmetric mask referred to in Chapter 1.2.1, several attempts have been made. H.W. Schnopper *et al.* demonstrated that the ambiguity can be resolved by making a second measurement at a different position [25]. Kowash *et al.* suggested the asymmetric mask concept by simply shifting slats and slits of masks by half pitch, so that the collimator masks no longer occupy a bilateral symmetry [33].

Sharma *et al.* utilized four RMC views at once, it was possible to achieve clearer reconstruction, thereby solving the ambiguity [32]. The intrinsic artifacts generated by the symmetric mask design are discussed further in Chapter 2.2.2.

1.2.3. Limitation of Previous Studies and Motivation

The University of Michigan study, which was used in the homeland security field by extending the existing RMC technique used in far-field imaging to the mid-range area, became the basic foundation of this doctoral research. The RMC study conducted by Kowash *et al.* has improved the RMC technique in the following three points, and the research carried out has significance [33,34].

1. A new unified near- and far-field (1-20 meters) system model that can calculate the system response in the near field or mid-range field was developed. In order to improve the accuracy of the model, the system model have accounted for several physical parameters such as mask thickness, mask penetrations by high-energy photons etc.

2. The 180° ambiguity issue caused by the design of the bilateral symmetric mask was resolved by a simple change of mask design that slightly shifts the front mask from the rotation axis. Thus, there is no longer a need to perform two iterations of modulation pattern measurement in a different location with two or more RMCs or one RMC. Essentially, it is possible to estimate the position of the radiation source by a single measurement with one RMC.

3. Using the NaI scintillation detector, an RMC-based gamma-ray imaging system with a field of view of 9° and angular resolution of up to 0.5° was developed. The capability of the developed RMC imaging system was verified experimentally in the near field and mid-range fields.

Based on the above results, Kowash and Boyce (Air Force Institute of Technology) developed a thermal neutron imaging system using the BF_3 detector [35]. Then, in order to improve the measurement efficiency of RMC, Wilkox performed research on the mask design, the sampling method of modulation pattern, with increased measurement time in the sampling location instead of reducing number of sample locations, and the pivot angle for improving the imaging quality [36]. These subsequent studies have been carried out at a level with further room for improvement. Further research and improvements are required for the RMC technique to be utilized in the field of radiation safety, this doctoral research is to be conducted with the following three motivations.

1. In response to the demand for dual-particle imaging devices capable of imaging both neutrons and gamma rays simultaneously, research is needed to develop a dual-particle imaging system based on RMC technique

2. A new collimator design that can eliminate 180° ambiguity issues caused by bilateral symmetric design and improve the performance of the system is needed to explored

3. Compared with other imaging systems, RMC-based imaging system is still lacking in its application for radioactive material detection because of its narrow field of view. Research is needed to improve the field of view of RMC imaging system

1.3. Purpose of this Work and Contributions

The objective of this dissertation is to further the research on the RMC technique for localization of the radioactive materials. The strategies chosen to improve the RMC technique were to study the dual-particle localization system and a method to extend the FOV. Several studies were performed to support this work, and the list of key developments from the studies are presented in this dissertation.

1. A dual-particle localization system using the RMC technique was developed to localize neutron and gamma-ray sources simultaneously. This was the first case of the integration of PSD capable scintillation detector with the RMC technique.

2. The conventional collimator mask design with bilateral symmetry posed an inherent ambiguity issue in the estimation of the source location. The method proposed to resolve this ambiguity showed better performance in terms of modulation efficiency and overall detection efficiency and angular resolution than earlier configurations of the RMC system.

3. As a preliminary step to improve FOV in the RMC system, a hemispherical collimator design was developed using a CZT detector.

Chapter 2. Dual-particle Localization System based on RMC Technique

2.1. Characterization of the CLYC Detector

2.1.1. Description of the CLYC Detector System

With remarkable developments on pulse shape discrimination (PSD)-capable scintillators recently, simultaneous detection of gamma rays and neutrons have become much more practicable [37]. Cs_2LiYCl_6:Ce (CLYC) scintillation detector is one of the scintillators for the "dual-mode", which means that one can detect both neutrons and gammas by a single modality. The detection of thermal neutron is based on $^6Li(n,\alpha)T$ reaction.

The CLYC detector system utilized in this thesis consists of a 2"-height × 2"- diameter cylindrical CLYC crystal, coupled to a R6233-100 photomultiplier tube by Hamamatsu (Shizuoka, Japan), preamplifier circuit, signal processing electronics and firmware that perform PSD, and output connections, packaged altogether in a hand-held size device. The CLYC crystal is enriched to 95% in ^6Li, wrapped by Teflon, and enclosed in an aluminum casing [38]. Measurement experiments were performed using the Trimode v.1.0.16 data acquisition software (Bubble Technology Industries (BTI), Canada), to collect gamma-ray and neutron signals with PSD. The appearance of the Trimode software is shown in Figure 6.

Figure 7 shows a two-dimension PSD plots provided by manufacturer. The data were collected using a moderated ^{239}Pu-Be source (6 cm-thick

polyethylene moderator) at a distance of 5 cm from the front of the system. The source had an activity of 22 GBq in January 1999, and the data were collected for 10 minutes. The CLYC detector utilized in this thesis showed a PSD figure of merit (FOM) of 3.1 using an energy window around the thermal-neutron peak. The shape parameter is related to the decay time of the signal and is therefore different for gamma-ray and neutron events, and it was calculated by comparing the charge collected at different times during each event [39].

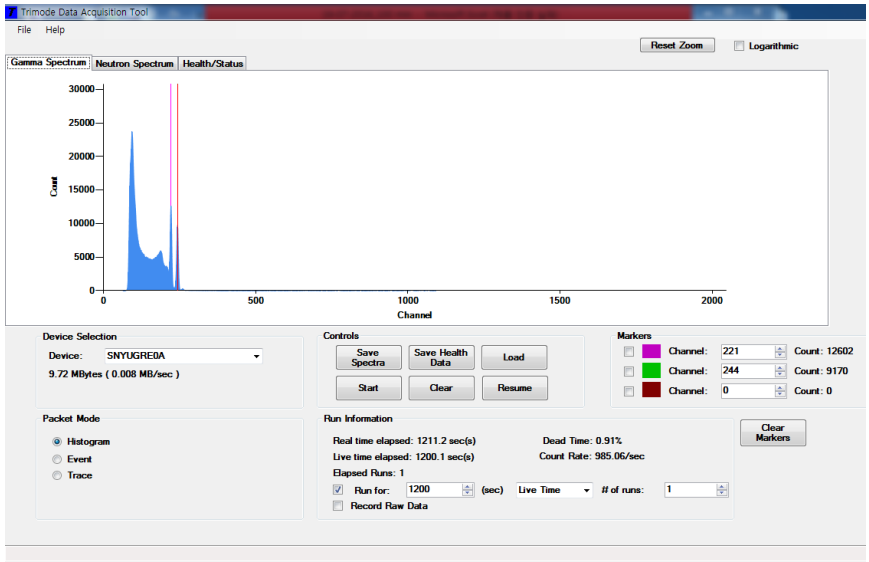

Figure 6. A screenshot of the Trimode data acquisition tool.

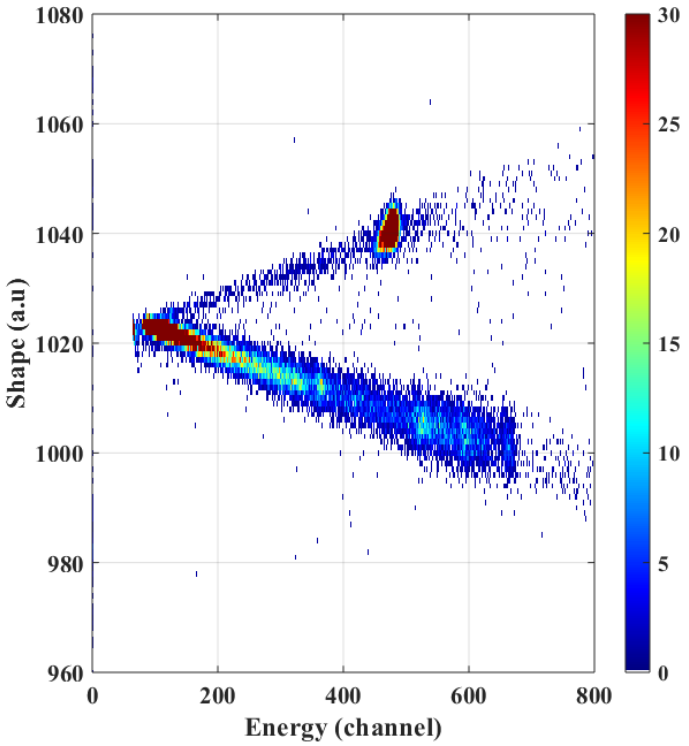

Figure 7. A two-dimension PSD plot from a moderated ^{239}Pu-Be source.

2.1.2. Simulation and Experiments on the Gamma-ray Detection

The geometry of the CLYC detector system supplied by BTI was encoded into a Monte Carlo N-Particle version 6.1 (MCNP6.1) input, as a schematic shown in Figure 8 [40].

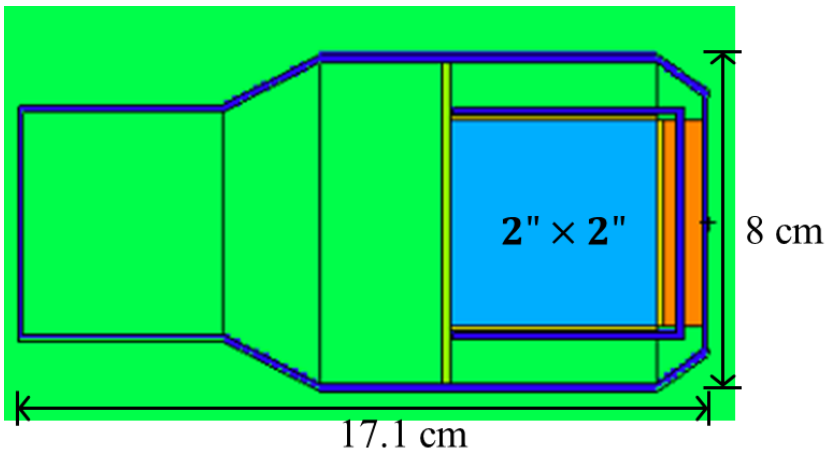

Figure 8. A schematic of the CLYC detector system modeled in MCNP6.1.

Based on the CLYC detector model aforementioned, gamma-ray detection efficiencies of the CLYC detector were simulated for various gamma-ray energies. A point source of gamma rays was assumed, and it located at a distance of 25 cm from the front face of the detector. For each gamma-ray source, 1×10^8 particle track histories were used. In the simulation, gamma rays emitted from ^{137}Cs, ^{60}Co, ^{133}Ba, ^{54}Mn and ^{22}Na nuclides were considered, and the pulse height tally (F8) in MCNP6.1 was used to distinguish full-energy absorption events of the gamma rays in the CLYC detector. Number of tallies obtained for each simulated gamma ray source were used to calculate the absolute full-energy absorption peak efficiency of the CLYC detector. Accordingly, one can also calculate the intrinsic peak efficiency of the detector by compensating the solid angle subtended by the 2”-diameter CLYC detector.

The simulation configuration was further refined by modeling gamma-ray sources which were actually used later in the measurement experiment; Table 3 provides the source information on the gamma-ray sources used in the experiment. The gamma-ray sources are standard calibration sources of R-type rod produced by Eckert & Ziegler in Germany. Radioactive material is contained in a 4.75 mm-diameter hole located in the cap area of a 12.7 cm high $\times$ 1.27 cm diameter plastic rod. Detailed geometry of the rod sources was also modeled and implemented in the Monte Carlo simulations.

The background radiation was measured for 6 hours, and measured ^{137}Cs, ^{60}Co, ^{133}Ba, ^{54}Mn and ^{22}Na sources listed in Table 3 for 20 minutes per source in live time. Sources were located at a distance of 25 cm from the front face of the detector, and the vertical location of the active area of radiation sources were aligned at the same height with the center of the CLYC detector. Figure 9 shows the measurement experiment set-up and a schematic of the MCNP6.1 simulation geometry. The dead time of the measurement was maintained under 1% for all measurements.

Table 3. A list of gamma-ray sources used in the measurement experiment

Source	Activity (Bq)	Reference date	Half-life (day)
^{133}Ba	393680	2016-04-01	3862
^{54}Mn	395160	2016-04-01	312
^{137}Cs	378510	2016-04-01	11012
^{22}Na	358752	2016-04-01	951
^{60}Co	380730	2016-04-01	1924

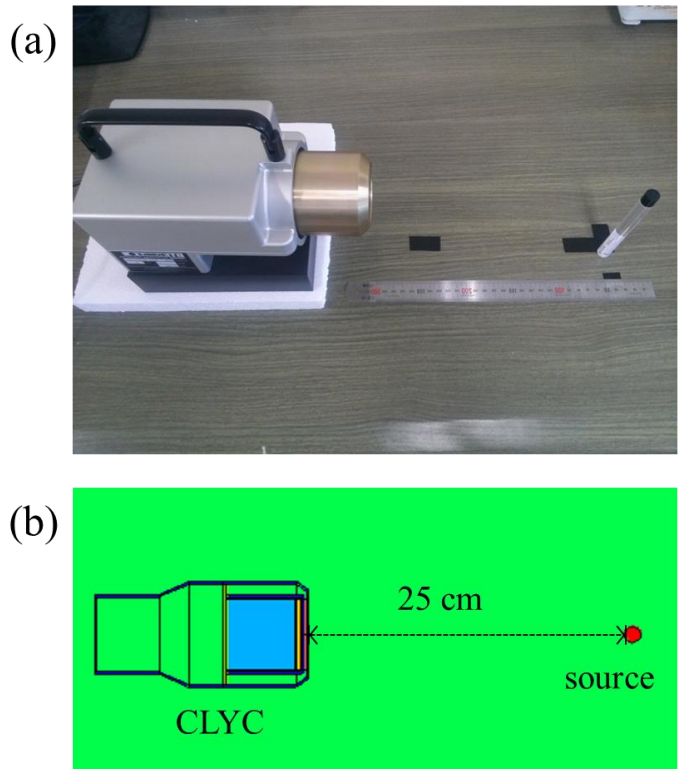

Figure 9. (a) An experimental set-up for the gamma-ray source measurement and (b) a schematic of the MCNP6.1 simulation geometry.

Gamma-ray spectra of each source were obtained and analyzed to calculate the peak area under the full-energy absorption peak. Absolute full-energy absorption peak efficiencies were calculated by the following equation [41]:

$$\varepsilon(E) = \frac{A_i}{\Lambda_i \cdot Y(E) \cdot t} \cdot K_i \qquad \text{Eq. (1)}$$

where A_i is the peak area of the radionuclide i, Λ_i is the reference activity of the radionuclide i, $Y(E)$ is the emission probability of the radionuclide at energy E, t is the spectrum collection time (live time) and K_i is the decay correction factor which is defined using the difference between the reference date of the source and the experimental date.

Gamma-ray energy spectra measured by CLYC detector are shown in Figure 10. Two sets of gamma-ray source measurement experiments were conducted on different days; however, spectral results from both measurements were identical. The energy resolution of full-energy absorption peaks was about 5% for most of gamma-ray sources. In detail, the values were 8.3%, 5.6%, 5.3%, 4.4%, 4.0% and 3.8% for 356 keV, 662keV, 835 keV, 1173 keV, 1275 keV and 1333 keV peaks respectively.

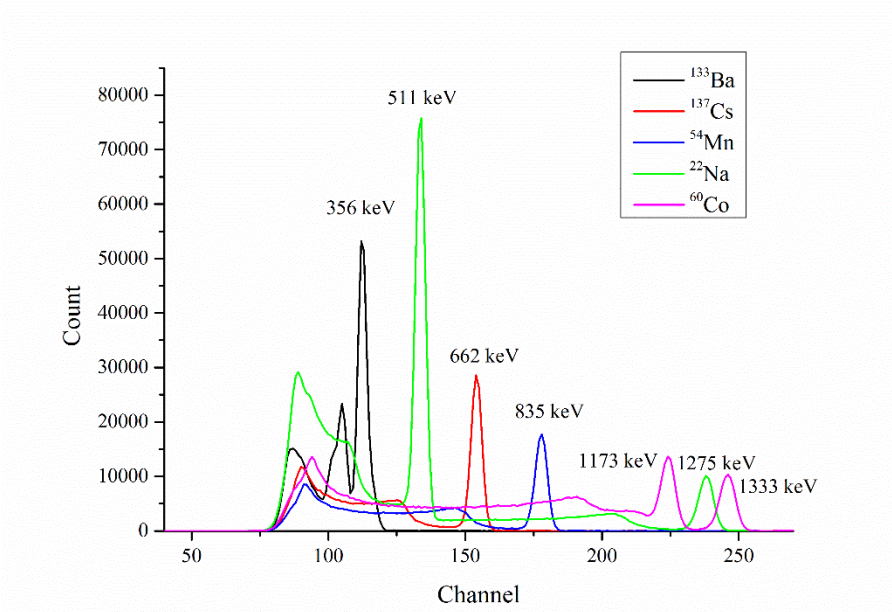

Figure 10. Gamma-ray energy spectra measured by the CLYC detector system.

MCNP6.1 simulation results on the gamma-ray detection efficiency were validated by comparing with detection efficiency simulation results calculated earlier at BTI. These earlier simulations used GEANT4 to calculate the absolute peak efficiency of a bare 2”-height × 2”-diameter CLYC crystal without any packaging, assuming a point source located 200 cm from the crystal face. In MCNP6.1 simulations, the CLYC detector model was able to generate results that are consistent with GEANT4 simulation of bare crystal. Figure 11 shows the comparison between two results, showing good agreement with each other. Slight differences are expected to be related to the internal structure of the CLYC detector model in MCNP6.1, as opposed to the bare CLYC crystal modeled in GEANT4.

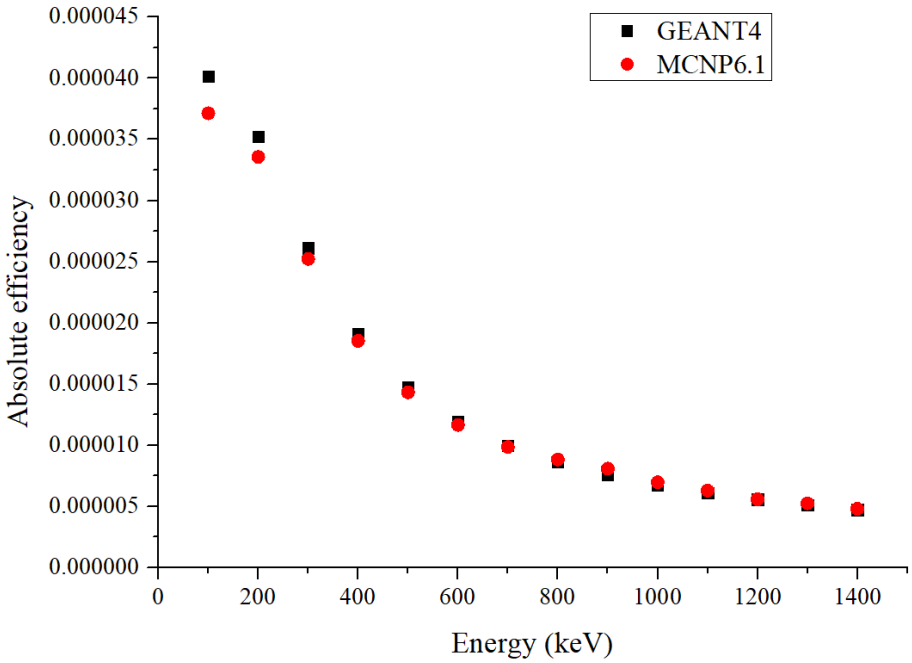

Figure 11. Comparison of absolute efficiencies calculated by BTI (using GEANT4, shown in black squares) and MCNP6.1 simulations.

Figure 12 shows (a) absolute and (b) intrinsic peak efficiencies for various gamma-ray sources simulated with MCNP6.1 and measured with the CLYC detector system modeled in the simulation. Detailed values of simulation and measurement results are given in Table 4. Error bars in Figure 12 indicate 95% confidence intervals on the simulated and experimental results. A relative error of 3% in the gamma-ray source activity, which was indicated in the reference source certificate, was also considered in the error bars via error propagation. Measured peak efficiencies were generally lower than simulated results, showing ~80% values of the simulation results for overall energy range. Simulated absolute efficiency values multiplied by 0.8, are shown as "Modified MCNP" field in Table 4. Modified MCNP values show very good agreements with the first and the second measurement results.

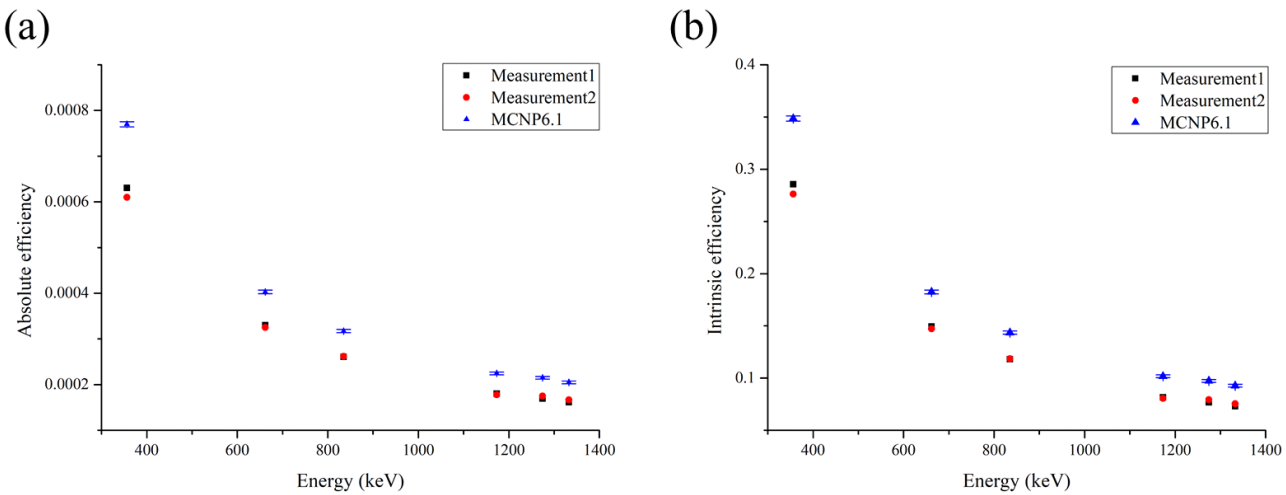

Figure 12. Simulated and measured gamma-ray detection efficiencies of CLYC detector: (a) absolute efficiency and (b) intrinsic efficiency for various gamma-ray energy peaks.

Table 4. Simulation and measurement results on the absolute gamma-ray detection efficiency

Energy (keV)	Measurement1	Measurement2	MCNP6.1	Modified MCNP
356	6.31×10^{-4}	6.10×10^{-4}	7.70×10^{-4}	6.16×10^{-4}
662	3.30×10^{-4}	3.25×10^{-4}	4.03×10^{-4}	3.22×10^{-4}
835	2.61×10^{-4}	2.62×10^{-4}	3.17×10^{-4}	2.54×10^{-4}
1173	1.80×10^{-4}	1.78×10^{-4}	2.25×10^{-4}	1.80×10^{-4}
1275	1.69×10^{-4}	1.75×10^{-4}	2.15×10^{-4}	1.72×10^{-4}
1333	1.61×10^{-4}	1.67×10^{-4}	2.05×10^{-4}	1.64×10^{-4}

The CLYC detector system from BTI utilizes a method that compares the leading edge of each pulse to the total integrated signal, in order to distinguish neutron signals from gammas. For low energy gammas, the pulse amplitude in general is not large enough for appropriate discriminations of the pulse shape, and discrimination of gammas and neutrons becomes difficult.

Figure 13 shows gamma-ray energy spectra of ^{109}Cd and ^{57}Co sources. In the case of ^{109}Cd, any counts were not collected from the 88.04 keV peak (channel # 76) because of the low-energy threshold in the CLYC detector system. When the background spectrum is subtracted from the measured spectrum, there weren't any counts left in the relevant channels that can give any statistical significance to discriminate the gamma peak. This was confirmed by two measurement experiments. In addition, in the case of ^{57}Co, there were enough counts collected in the channels relevant to the 122 keV peak (channel # 81) to discriminate the feature; however, calculated detection efficiency based on the measured counts gave values far below what was expected from the MCNP6.1 simulation. The low-energy discrimination level of the detector system that is internally set to distinguish valid radiation signatures from noise could cut off pulses from low energy gamma rays. Ambiguity in pulse shape discrimination becomes more significant when the pulse amplitude is smaller. In that procedure, the system inevitably has to rule out some portion of valid full-

energy absorption pulses.

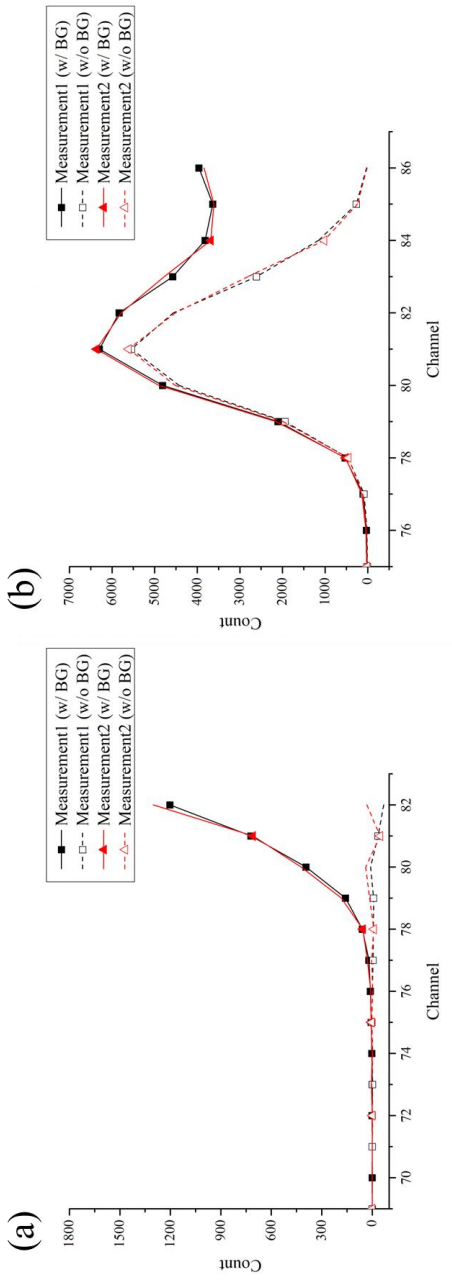

Figure 13. Gamma-ray spectra of: (a) ^{109}Cd and (b) ^{57}Co, measured with the CLYC detector system.

2.1.3. Simulation and Experiments on Neutron Detection

Simulations on behavioral characteristics of neutrons were also performed and verified by the ^{252}Cf neutron source measurement experiments. In the CLYC detector, a triton and an alpha particle are produced by the neutron capture reaction with ^{6}Li; however, reaction libraries for alpha particle production in the neutron capture reaction were not available in the default MCNP data libraries. Therefore, the number of tritons created in CLYC was counted instead, using the cell flux tally with reaction multipliers (F4/FM) tally, to calculate the neutron response by the CLYC scintillator [42]. For each neutron simulation hereafter, 1×10^{8} particle track histories from the source were simulated.

First, the intrinsic detection efficiency of the CLYC detector system was calculated for an ideal thermal neutron source by MCNP6.1. A point source of 0.025 eV thermal neutron located at 25 cm distance from the front face of the CLYC detector was assumed, and the number of thermal neutron capture reactions in the CLYC detector volume was tallied.

Next, the ^{252}Cf source used in the measurement experiment at the Korea institute of nuclear nonproliferation and control (KINAC) was modeled in MCNP6.1. The ^{252}Cf source was an N-252 model (A3014-01 capsule type) produced by Eckert & Ziegler in Germany. The source body was in a cylindrical

shape with 3.63 cm in height and 0.94 cm in diameter, and the radioactive material was contained in the 0.157 cm-diameter region at the center of the rod. The activity of ^{252}Cf source was 3.33 MBq on the reference date of 15 Oct. 2015. The energy spectrum of neutrons emitted from ^{252}Cf was assumed to follow the Watt fission spectrum [43].

Numbers of thermal neutrons measured by CLYC were calculated varying the thickness of the PE moderator, and measurement experiments were performed accordingly as shown in Figure 14. Thermal neutrons from the ^{252}Cf source with 11 different thicknesses of the PE moderator were measured. The dead time of the measurement was also under 1% for all measurements. For the simulation, environmental conditions of the experiment were attempted to be modeled as close as possible to a reasonable content, which include, assuming the workbench table as a 5-cm thick table made of polycarbonate, wood, or concrete, and modeling the polycarbonate source holder shown in the schematic illustrated in Figure 14 (b). Other environmental factors were not considered.

To verify the designed MCNP6.1 approach, the neutron detection efficiency value was compared with those reported in previous literature. Intrinsic efficiency of 76.2% was obtained for bare 2”-height × 2”-diameter CLYC crystal without packaging, and the value was similar to a previous study. In the previous study, CLYC with the Li component enriched to 95% in ^{6}Li provided

around 80% intrinsic efficiency for thermal neutrons [39]. As experimental environments were not considered in this calculation, contributions from the build-up effect could have been ignored, thus, the simulation result may underestimate the intrinsic detection efficiency. Other than this, two results make agreements with differences in a reasonable range; The designed model in MCNP6.1 will deliver reasonable estimations on the detector response to neutrons.

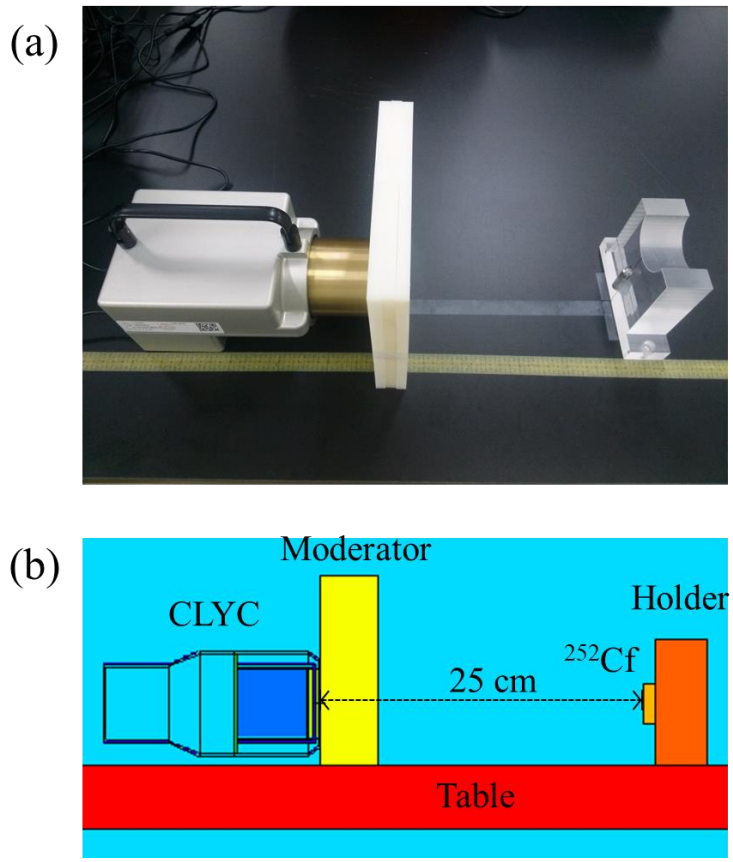

Figure 14. (a) An experimental set-up for the neutron source measurement and (b) a schematic of the MCNP6.1 simulation geometry.

MCNP6.1 simulations and measurement experiments were performed to obtain neutron counts from ^{252}Cf source with PE moderators of various thicknesses. Two sets of measurement experiments were also performed on different days, to verify possible significant dependency of the system operation on the experimental environment; however, results from both measurements were almost the same. Figure 15 shows counts of thermal neutrons (after thermalization by the PE moderator) for various PE moderator thicknesses, normalized to the maximum count obtained by each measurement, and MCNP6.1 simulation. Without consideration of the experimental environment, simulated neutron counts changing over PE moderator thicknesses did not make good agreements with results from experiments, in terms of the overall trend of the curve. The optimal thickness of PE moderator that can give the maximum counts of thermalized neutrons was estimated to be 7.5 cm, based on the simulation without consideration of the environment, whereas the result from the experiment indicated that around 5 cm gives the maximum counts of neutrons. Similar results were obtained in a previous study on the simulation of CLYC detector response to neutrons [44]. The previous study also showed a significant discrepancy between Monte Carlo simulation and measurements on ^{252}Cf source with PE moderators.

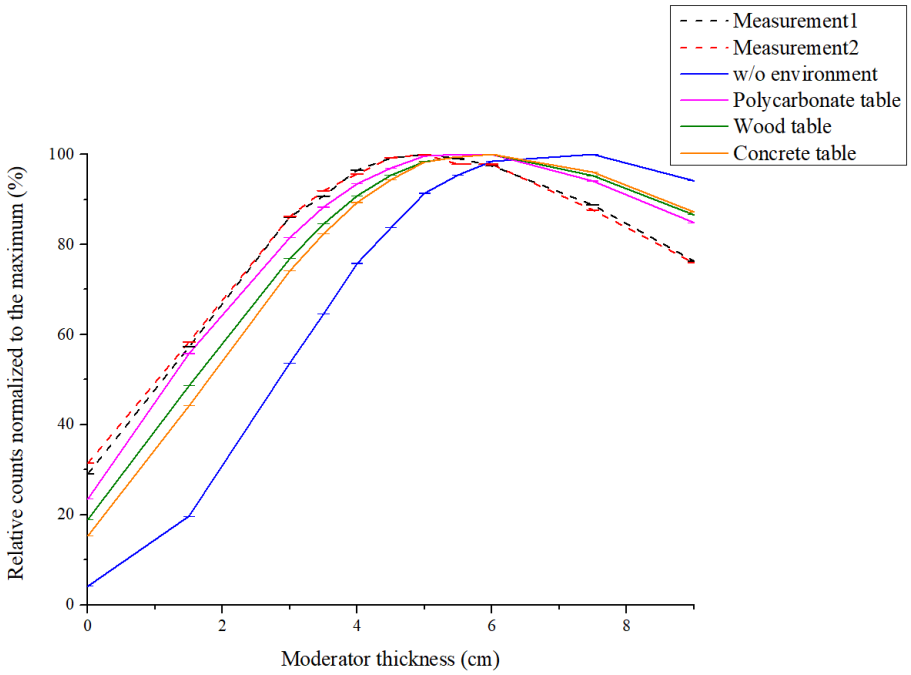

Figure 15. Simulated and measured thermal neutron counts normalized to the maximum count in each set-up, obtained for various thicknesses of PE moderator; w/o environment means the table and the source holder were not considered in the simulation.

Thus, experimental environments were modeled to a reasonable degree. The source holder and table used for the measurement were included into the MCNP6.1 simulation. The source holder was assumed to be polycarbonate, and the table was assumed to be either wood, concrete or polycarbonate. As shown in Figure 16, just a simple implementation of experimental environments made substantial changes on the simulation result, and the simulation result made good estimations on neutron moderation trend. An optimal thickness of the PE moderator for neutron detection was estimated to be around 5 cm. Table 5 shows simulation results on the absolute neutron detection efficiency with and without consideration of the experimental environment, compared with 2 sets of measurement results. Error bars in Figure 16 represent 95% confidence intervals given by the simulation and measurement counts. The absolute efficiency was calculated in a similar way as for gammas. Notably, the measurement results show quite different values from the MCNP6.1 simulations without environment, whereas simulation results with concrete and wood show less deviation from the measurement results. Simulation results with polycarbonate showed relatively higher values than measurement results, however, the overall shape of the curve for the normalized counts showed good agreements with measurement results in Figure 16. Thus, a constant value, 0.8 was multiplied on the polycarbonate results, represented in Figure 16 as

“modified PC”. The results showed good agreements with the measurement result, which reconfirm consistent around 20% discrepancy similar to gamma-ray measurements and simulations.

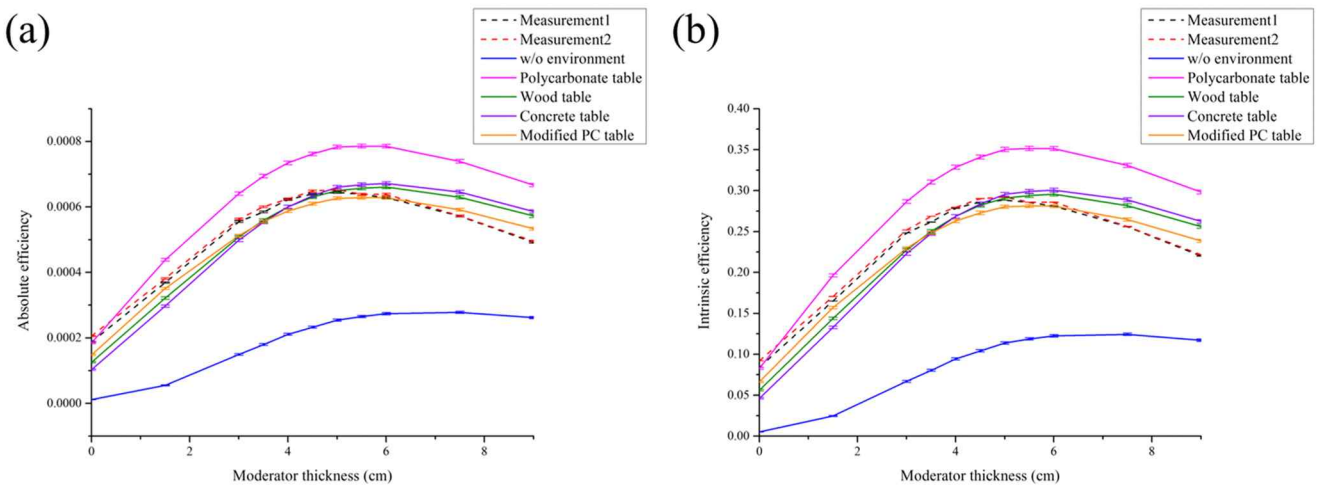

Figure 16. (a) Absolute and (b) intrinsic neutron detection efficiency of CLYC at various moderator thicknesses; w/o environment means the table and the source holder were not considered in the simulation.

Table 5. Simulation and measurement results on the absolute neutron detection efficiency

Moderator thickness (cm)	Measurement1	Measurement2	w/o environment	Polycarbonate	Wood	Concrete
0	1.88×10^{-4}	2.06×10^{-4}	1.17×10^{-4}	1.85×10^{-4}	1.26×10^{-4}	1.03×10^{-4}
1.5	3.69×10^{-4}	3.81×10^{-4}	5.48×10^{-4}	4.39×10^{-4}	3.21×10^{-4}	2.97×10^{-4}
3	5.55×10^{-4}	5.63×10^{-4}	1.49×10^{-4}	6.41×10^{-4}	5.08×10^{-4}	4.98×10^{-4}
3.5	5.85×10^{-4}	6.00×10^{-4}	1.80×10^{-4}	6.94×10^{-4}	5.59×10^{-4}	5.54×10^{-4}
4	6.23×10^{-4}	6.25×10^{-4}	2.11×10^{-4}	7.34×10^{-4}	6.00×10^{-4}	6.00×10^{-4}
4.5	6.39×10^{-4}	6.49×10^{-4}	2.33×10^{-4}	7.62×10^{-4}	6.31×10^{-4}	6.34×10^{-4}
5	6.45×10^{-4}	6.53×10^{-4}	2.54×10^{-4}	7.83×10^{-4}	6.50×10^{-4}	6.61×10^{-4}
5.5	6.39×10^{-4}	6.39×10^{-4}	2.65×10^{-4}	7.86×10^{-4}	6.57×10^{-4}	6.68×10^{-4}
6	6.28×10^{-4}	6.39×10^{-4}	2.74×10^{-4}	7.86×10^{-4}	6.61×10^{-4}	6.72×10^{-4}
7.5	5.72×10^{-4}	5.73×10^{-4}	2.78×10^{-4}	7.39×10^{-4}	6.30×10^{-4}	6.46×10^{-4}
9	4.92×10^{-4}	4.96×10^{-4}	2.62×10^{-4}	6.67×10^{-4}	5.72×10^{-4}	5.86×10^{-4}

2.2. RMC System Design

2.2.1. Structural Design of RMC System

The design of the RMC system is shown in the Figure 17 (a). The RMC system consists of an aluminium support tube, driver tube with two ball bearings, two collimator masks, timing pulley/belt, stepper motor and CLYC detector. On the driver tube, there are 4 pins at the front and rear faces. With these pins, the collimator mask can be easily attached and replaced with another mask, and the distance between two masks was set to be 24 cm in accordance with the previous study [33]. A timing pulley and belt were mounted onto the driver tube and stepper motor which was used to transmit the power from a stepper motor to rotate the RMC. A timing pulley was also designed with the conversion factor from the motor pulley to the driver tube pulley of 4.5 to 1. Therefore, the motor pulley rotates 4.5° to rotate the RMC by 1°. In addition, the detector mount was designed to match the center of the detector and the center of the collimator mask.

The most important part in the RMC system is the collimator mask. The design of the collimator mask has a direct influence on the field of view, detection time, and modulation pattern shape. The common design of collimator mask is the bilateral symmetric slit configuration. However, in the case of a bilateral symmetric mask, there is a 180° ambiguity caused by the

characteristics of modulation patterns and symmetric slit design [23,45]. To remove this ambiguity, collimator mask was optimized with an asymmetric mask design, which is shown in the Figure 17 (b) [46].

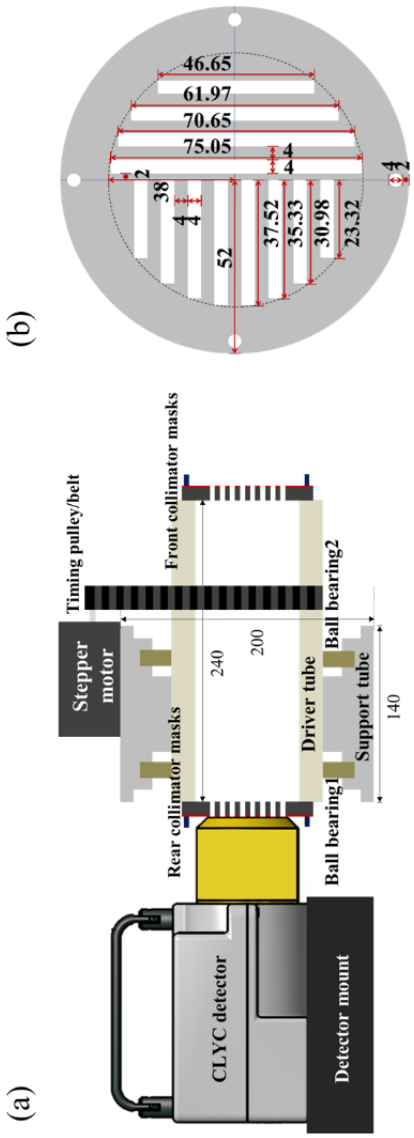

Figure 17. (a) The design of CLYC-based RMC system, and (b) collimator mask (unit: mm).

2.2.2. Optimization of Collimator Mask Design

For the mechanical collimation method, it is desirable that the thickness of the collimators is as opaque as possible. To determine the proper material and thickness of the collimator masks for dual-particle localization system, Monte Carlo simulations were performed using MCNP6.1. In the simulation, the detector was exposed to a point source of gamma rays and 0.025 eV thermal neutrons that was positioned 25 cm away from the center. The gamma response of the detector was calculated using the pulse height tally (F8) tally and, the neutron response in CLYC was counted by the cell flux tally with reaction multipliers (F4/FM) in MCNP6.1. The simulation was conducted with 1×10^{8} source particle histories.

The calculated results are shown in Figure 18. Based on the shielding efficiencies, the mask was designed with a laminated structure which is a combination of 1 cm-thick lead (Pb) and 0.2 cm-thick borated polyethylene (BPE). In the MCNP6.1 simulation, the shielding efficiency of a 1 cm-thick Pb mask was 95.20% for 356 keV gamma rays, and the shielding efficiency for thermal neutron was 100% when 0.2 cm-thick BPE was used.

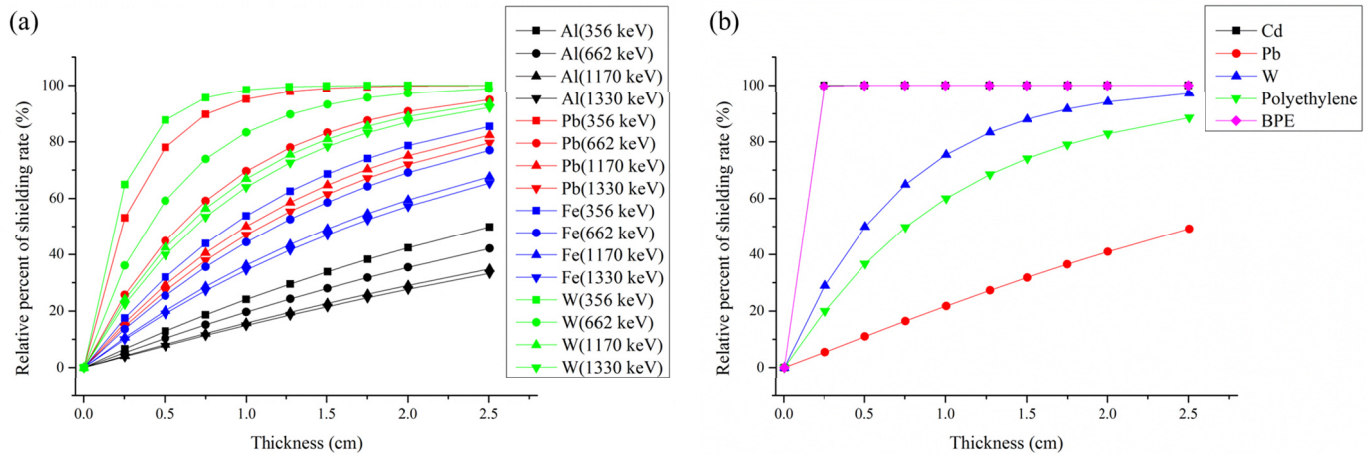

Figure 18. Sheiding efficiencies of gammas and thermal nuetron versus mask thickness.

A typical collimator mask of RMC contains parallel slits that span across the circular area of the mask. As the collimator masks are rotated together, the open area made by the slits of collimator masks changes, and it leads to the modulation patterns of the counts on the detector behind the collimator masks. In this regard, the design parameters of slits are the key factors affecting the morphology of modulation patterns.

To assess the influence on the modulation patterns attributed by the configuration of slat and slit, the modulation patterns were acquired using MCNP6.1, implementing a series of slat/slit configurations. Figure 19 shows the schematic diagram of slat/slit intervals used for the investigation. Modulation patterns were calculated for various slat and slit width combinations. Firstly, both slat/slit width were changed from 0.2 to 0.3, 0.4 and 0.5 cm, and selected one that appears to be optimal. Then, slat width was changed from 0.2 to 0.3, 0.4 and 0.5 cm without changing the slit width to investigate the influence, and the slit width was changed in the same manner fixing the slat width. The radius of masks was kept the same for all the mask designs and each slit stretches over to touch the inner 2.5 cm-radius circle, which is the inner radius of the flight tube of the RMC system.

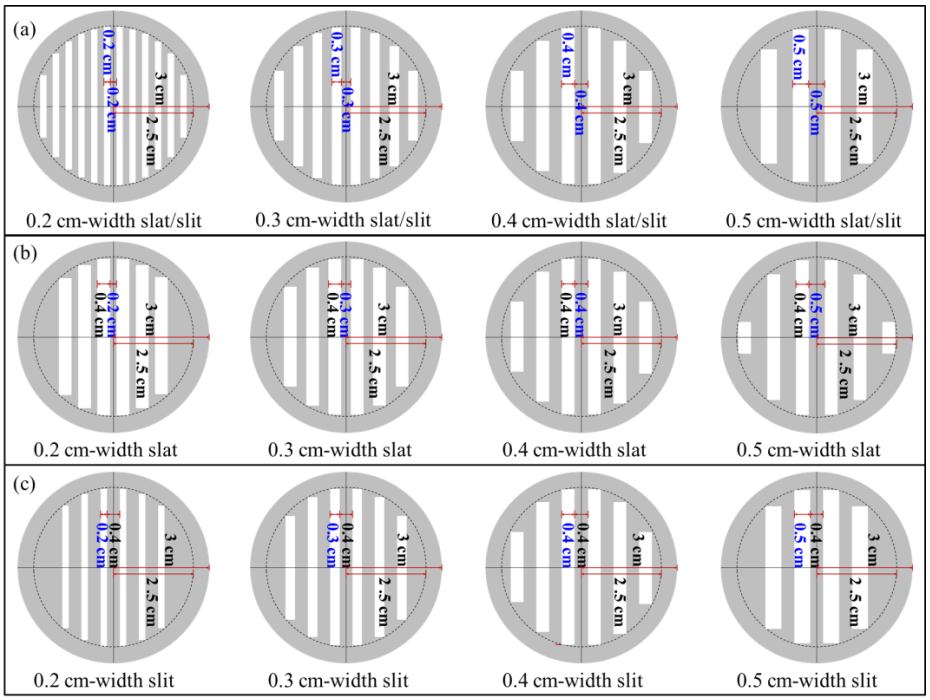

Figure 19. A Schematic diagram of collimator masks with various slat/slit interval combinations used for optimization, changing: (a) the slat/slit widths, (b) the slat width and (c) the slit width.

For better imaging performance utilizing RMC, it would be preferred to have clearly distinguishable modulation patterns constructed per each source location, that is, each modulation pattern can make a fine representation of intrinsic locational properties of the source, and thus it can be unambiguously reconstructed as an image. The analysis of the modulation patterns was mainly conducted by considering the following two factors, modulation efficiency and transmission efficiency, for quantitative evaluation of the modulation patterns. The modulation efficiency is relative magnitude of difference between maximum and minimum counts in the modulation pattern with respect to the maximum count and can be represented as:

$$Modulation\ \ efficiency = 1 - min(y_n)/max(y_n) \qquad \text{Eq. (2)}$$

One can expect to obtain modulation patterns which consist of counts that are significantly different from each rotational angle to angle, by using a collimator mask set of a high modulation efficiency. Distinguishable count differences per each angle will present much clearer modulation patterns in term of the morphology, thus can lead to less source of errors in image reconstruction.

The transmission efficiency represents overall detection efficiency of the RMC system and is desired to be higher for more efficient utilization of incident particles. It is defined as an average number of counts measured in detector between 0° and 360°:

$$Transmission\ \ efficiency = \sum y_n / n \qquad \text{Eq. (3)}$$

where y_n is the number of counts measured at a certain rotational angle in a modulation pattern and n is the number of discrete rotational angles. Since the transmission efficiency is associated with the counting statistics of the modulation pattern, a low transmission efficiency, for example, can impose a high counting uncertainty issues in the formation of the modulation pattern.

Batches of Monte Carlo simulations were performed while varying the slat and slit widths as described above, and data sets varying both slat/slit widths, slat width only, and slit width only were obtained accordingly. Figure 18 shows the modulation pattern results for various slat/slit interval combinations, normalized to the maximum counts for each pattern. Error bars on each data point indicate 95% confidence intervals calculated from the simulation.

As can be anticipated from the inherent properties of the RMC, the

modulation pattern results, in general, tend to show more “features” (peaks and valleys) in the modulation profile as the number of slats/slits increases. Simulation results for 0.2 cm slat/slit interval in Figure 20 (a) show more complexities in overall shape of the modulation pattern, even though the variation of the relative counts in the normalized modulation pattern is not as evident compared to other interval cases. Meanwhile, relative differences between maxima and minima counts become more significant as the system incorporates more collimation, i.e. mask area covered by slats increases, making the features of the modulation pattern much more prominent and distinguishable. Therefore, 0.3 cm, 0.4 cm and 0.5 cm cases in Figure 20 (a) exhibited rather more discernable “features” judged by the appearance of the normalized modulation pattern. However, the total number of counted particles will decrease as more incident radiations are blocked by slats, and the system may end up compromising the efficiency of radiation imaging.

The property of the modulation pattern was evaluated from each slat/slit width condition by calculating the modulation efficiency and the transmission efficiency, of which results are summarized in Table 6. When both slat/slit widths were changed, 0.2, 0.3, and 0.4 cm cases showed similar transmission efficiencies whereas the 0.5 cm case showed a value that was at least 20% lower, while exhibiting quite different modulation efficiencies. In general, the

modulation efficiency increased substantially as slat/slit widths were increased, however the increasing trend was gradually slowing down with respect to the slat/slit widths increase. The ratio between the open area and the total area of the mask, which affects the probability of particles passing through the collimator as well as the ratio of the visible region to the total FOV (sensitivity) for RMC, showed a similar trend with transmission efficiencies, as shown in Table 7. And the theoretical angular resolution decreased as the slat/slit width increased.

The slat/slit widths of 0.4 cm was judged as a good starting point as could be a good compromise between the transmission efficiency and the modulation efficiency, also considering the open-to-total area ratio and the angular resolution. Therefore, the transmission efficiency results were normalized with respect to the 0.4 cm slat/slit case henceforth, for the comparison purpose. The baseline of slat or slit width was set as 0.4 cm and changed each variable to investigate how slat-to-slit size ratio will affect the behavior of the modulation patterns. Comparison of modulation efficiency values for modulation patterns shown in Figs. 20 (b) and 20 (c) indicate that overall property of the modulation pattern can be more sensitively affected by the variation of slat widths than slit widths. The modulation pattern becomes more variable and distinguishable as slat width increases, however, the transmission efficiency deteriorates as the

mask leads to more blocking of incident radiation. Variation of the slit size did not alter modulation efficiencies very much, and the transmission efficiency was kept in the similar range for the slit widths greater than 0.3 cm. Therefore, the 0.4 cm slat/slit setup could be a good combination for the collimator mask design, and chose it as a basic parameter for the mask design followed.

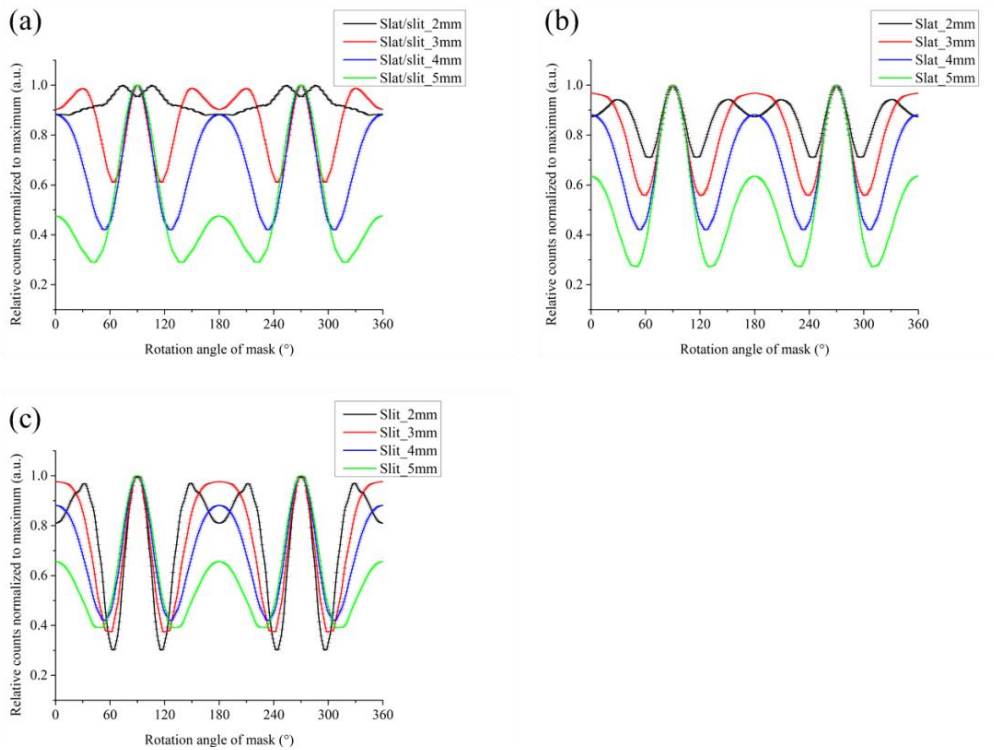

Figure 20. Simulated modulation patterns for various slat/slit widths changing: (a) both slat/slit widths, (b) slat width and (c) slit width.

Table 6. Modulation and transmission efficiency values for various slat and slit configurations. Transmission efficiencies are normalized to the value of 0.4 cm-width slat/slit case

Changing Both Slat/Slit Widths			Changing Slat Width, Fixed Slit Width			Changing Slit Width, Fixed Slat Width		
Slat/Slit Widths (cm)	Modulation Efficiency	Transmission Efficiency	Slat/Slit Widths (cm)	Modulation Efficiency	Transmission Efficiency	Slat/Slit Widths (cm)	Modulation Efficiency	Transmission Efficiency
0.2 / 0.2	0.12	1.01	0.2 / 0.4	0.29	1.58	0.4 / 0.2	0.70	0.50
0.3 / 0.3	0.39	1.11	0.3 / 0.4	0.44	1.32	0.4 / 0.3	0.63	0.82
0.4 / 0.4	0.58	1.00	0.4 / 0.4	0.58	1.00	0.4 / 0.4	0.58	1.00
0.5 / 0.5	0.71	0.77	0.5 / 0.4	0.73	0.67	0.4 / 0.5	0.61	0.96

Table 7. The open-to-total area ratio of masks, the sensitivity and the nominal angular resolution calculated for each slat/slit configuration

Changing Both Slat/Slit Widths			Changing Slat Width, Fixed Slit Width			Changing Slit Width, Fixed Slat Width		
Slat/Slit Widths (cm)	Open area / Total area (sensitivity)	Angular resolution (°)	Slat/Slit Widths (cm)	Open area / Total area (sensitivity)	Angular resolution (°)	Slat/Slit Widths (cm)	Open area / Total area (sensitivity)	Angular resolution (°)
0.2 / 0.2	0.332 (11.02%)	0.477	0.2 / 0.4	0.369 (13.64%)	0.716	0.4 / 0.2	0.189 (3.57%)	0.716
0.3 / 0.3	0.327 (10.67%)	0.716	0.3 / 0.4	0.349 (12.18%)	0.836	0.4 / 0.3	0.266 (7.08%)	0.836
0.4 / 0.4	0.322 (10.35%)	0.955	0.4 / 0.4	0.322 (10.35%)	0.955	0.4 / 0.4	0.322 (10.35%)	0.955
0.5 / 0.5	0.295 (8.70%)	1.193	0.5 / 0.4	0.276 (7.60%)	1.074	0.4 / 0.5	0.306 (9.34%)	1.074

Based on the outcome of the slat/slit width optimization study, several types of asymmetric collimator masks were proposed to overcome limitations of the previous mask design with bilateral symmetry. The width of both slats and slits was set at 0.4 cm and came up with a few possible asymmetric mask patterns. Figure 21 (a) shows the previous symmetric mask pattern for the RMC, and (b), (c) and (d) show asymmetric mask pattern candidates. As an approach to remove bilateral symmetry of the mask design, the following designs were considered: i) removed the half of the slits (Figure 21 (b)), or ii) replaced one slit with different length (Figure 21 (c)), or iii) changed the orientation of the slits for the half of the mask (Figure 21 (d)). Properties of modulation profiles obtained with these mask designs were compared with ones obtained with an asymmetric mask design conceptually proposed in the previous study, which is constructed by simply shifting one of the masks slightly off axis by 0.2 cm [33].

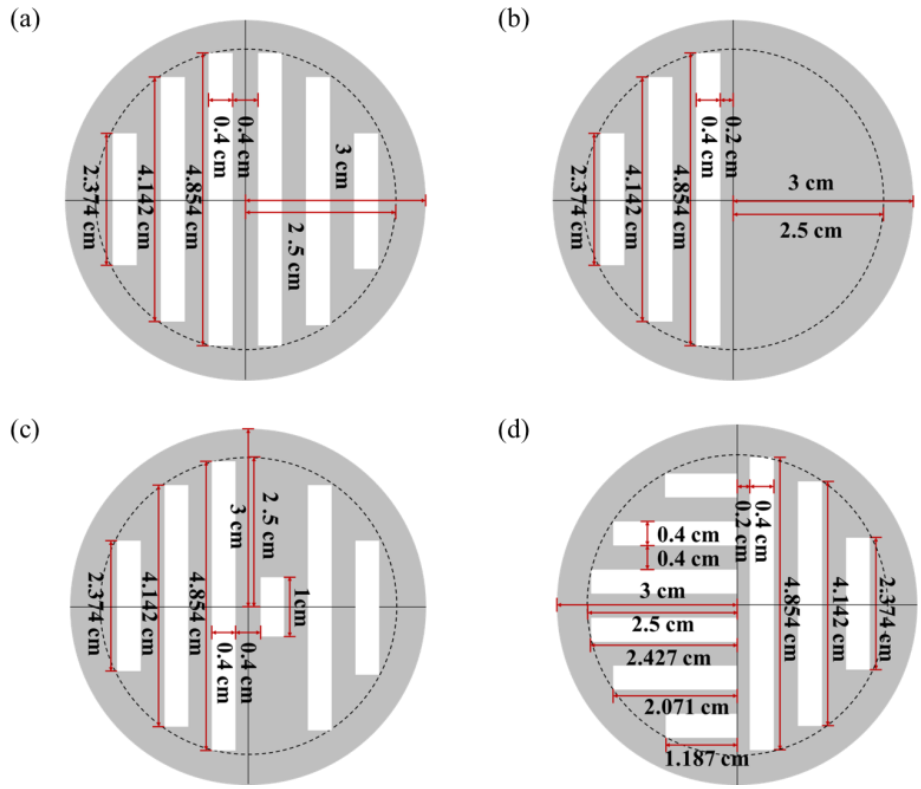

Figure 21. Patterns of collimator masks: (a) symmetric mask (sym), (b) asymmetric-half mask (asym_half), (c) asymmetric-center mask (asym_center) and (d) asymmetric-combination mask (asym_combi).

As a next step, the ambiguity issue of the source location estimation was tried to solve, which originates from the bilateral symmetry of the collimator masks. Figure 22 shows the modulation patterns obtained for each mask design shown in Figure 21. Error bars indicate 95% confidence intervals on the simulated results. Modulation patterns simulated for asymmetric mask designs were compared with ones for the bilaterally symmetric mask design with 0.4 cm slat/slit width from the previous section.

In case of the collimator masks with bilateral symmetry, modulation patterns obtained for each position are repeated with an 180° periodicity, and the ambiguity issue in the estimation of the source position from the modulation pattern obtained for these type of masks is attributed to this periodicity. According to the fundamental nature of the RMC technique, rotational shift of the source location while keeping the source-to-axis distance the same, will cause a parallel translation of the modulation pattern in angular domain with respective rotation angle of the source [23]. Therefore, two sources located symmetrically with respect to the rotation axis such as (5 cm, 0 cm, 200 cm) and (-5 cm, 0 cm, 200cm) will result in exactly the same modulation pattern with each other.

On the other hand, modulation patterns that can be generated by the rotation of collimator mask without bilateral symmetry will not exhibit the 180°

periodicity for the entire rotation, enabling estimation of source location without ambiguity. Modulation and transmission efficiencies of modulation patterns that can be obtained with various designs of asymmetric collimator masks were calculated and compared with ones obtained with the symmetric masks in Table 8. Efficiency values were calculated for 3 source locations – 6, 15 and 25 cm away from the rotational axis – to investigate the source location dependency of efficiency values for each mask design. In terms of modulation efficiency, the asymmetric-half mask showed the most favorable results regardless of the source position, whereas asymmetric-2 mm-shift and asymmetric-combination mask designs showed relatively high transmission efficiency values compared with asymmetric-half and asymmetric-center masks. In the comparison of efficiency values for the asymmetric-2 mm-shift mask and the asymmetric-combination mask depending on the source location, modulation and transmission efficiencies of the asymmetric-combination mask showed less variation depending on the source location than ones of the asymmetric-2 mm-shift mask.

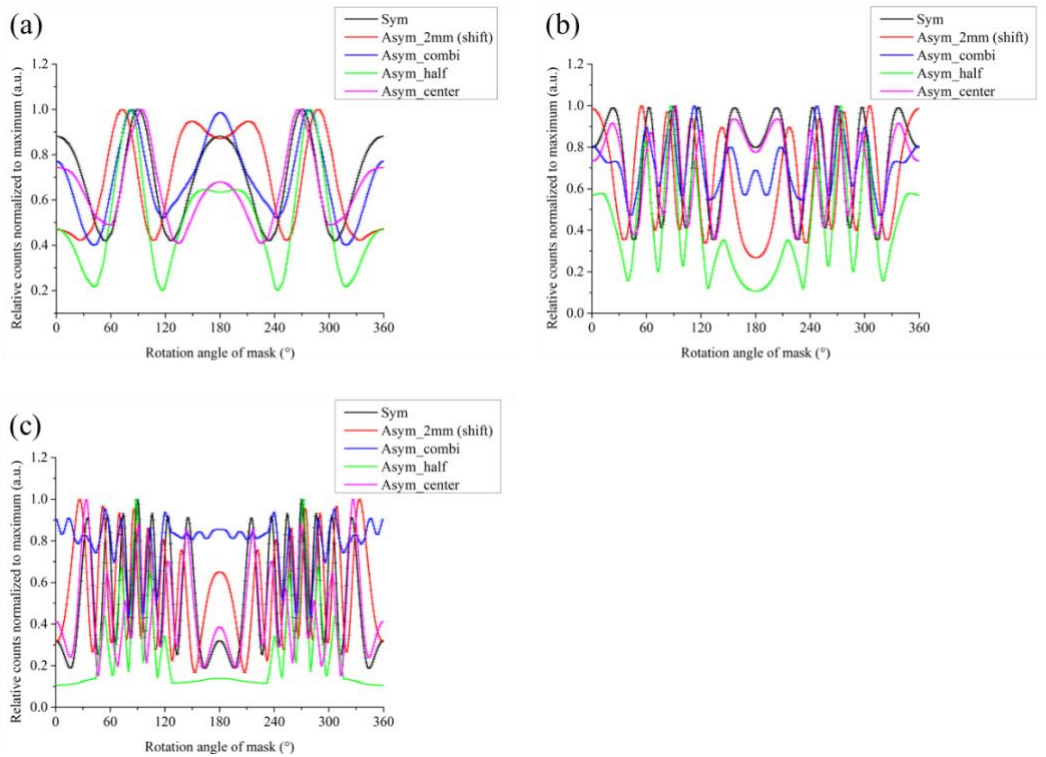

Figure 22. Comparison of modulation patterns obtained with each mask design for various source positions located at (x, y, z) [cm]: (a) (6, 0, 200), (b) (15, 0, 200) and (c) (25, 0, 200).

Table 8. Modulation and transmission efficiencies calculated for various mask designs and source positions. ME and TE stands for the modulation efficiency and the transmission efficiency, respectively, and the transmission efficiency was normalized to the 0.4 cm slat/slit symmetric mask case

	Source position: (6,0,200)		Source position: (15,0,200)		Source position: (25,0,200)	
	ME	TE	ME	TE	ME	TE
Sym	0.58	1.00	0.65	1.00	0.81	1.00
Asym_2mm (shift)	0.58	1.01	0.73	0.90	0.83	1.12
Asym_combi	0.60	1.00	0.53	0.95	0.57	1.07
Asym_half	0.80	0.44	0.89	0.32	0.89	0.26
Asym_center	0.59	0.71	0.64	0.70	0.85	0.67

2.2.3. Fabrication of RMC components

The fabricated components of RMC system were shown in the Figure 23. Each component was manufactured separately and then assembled all together. The driver/support tube was made of A-A-3003 aluminum alloy because of its high strength and it has very good resistance to atmospheric corrosion. The aluminum alloy was cut with lathe machine to make the shape of the driver/support tube design. In addition, considering the driver tube size, a 68-24-ZZ/C3 ball bearing was chose which has 120 mm internal diameter and 150 mm external diameter (NJL Japan, Japan), and the bearings were fixed using NR-145 snap ring (NTN, USA). Furthermore, the bearing housings were constructed in the support tube to prevent the dislocation of the bearings.

For the collimator mask, a laminated structure was designed for dual-particle purpose as mentioned in the previous section, which consisted of 99.96% ultra-pure lead plate (Semyoung metal, Korea) and high-quality borated polyethylene (BPE) plate (Dynex, Korea). The BPE plate has a higher hydrogen content (>115 g/liter) than water and the boron content is over 56 g/liter. Based on these plates, the slits of mask were cut with a lathe and 2D CNC machine tool.

A 22-tooth timing pulley (8 mm in internal diameter and 33.87 mm in external diameter) and a 99-tooth timing pulley (120 mm in internal diameter

and in 156.41 mm in external diameter) were manufactured, since the timing pulley was designed with the conversion factor from the motor pulley to the driver tube pulley of 4.5 to 1. Considering the distance between the center of the driver tube and the stepper motor (i.e., 134.5 mm), the belt was fabricated with length 600 mm and width of 10 mm. Furthermore, in order to prevent tension changes on the belt due to the experimental condition, a stepper motor mount was designed and fabricated which can adjust ± 2 mm of the distance between center of the driver tube and stepper motor.

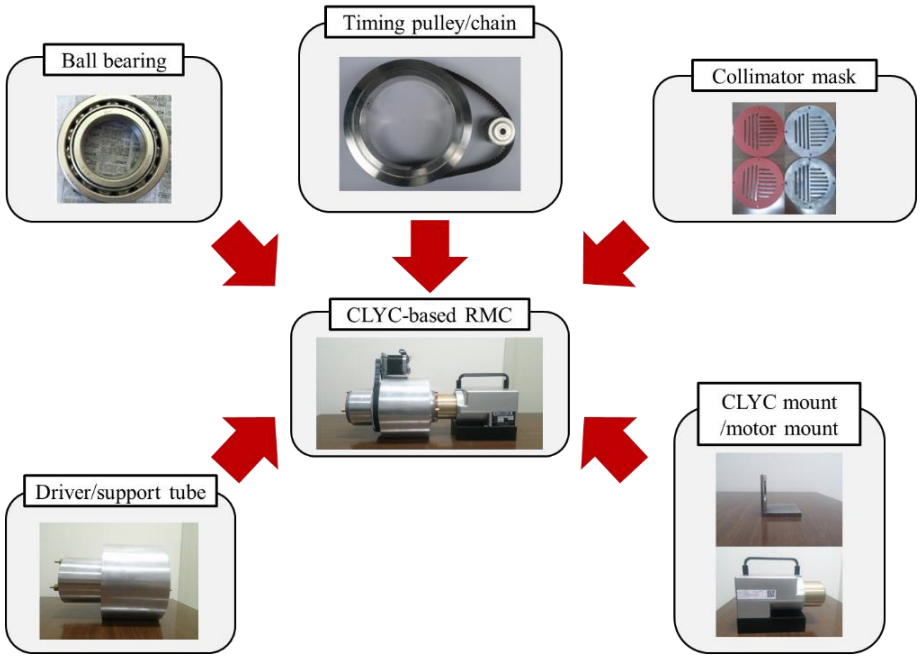

Figure 23. Components of dual-particle localization system.

One of the important considerations for the RMC imager is the rotation control system. To control the RMC rotation, a QSH 6018-86-28-310 stepper motor (Trinamic Motion Control, Germany) was used. The stepper motor is controlled by an Arduino due board with DRV8880 motor driver (Pololu Robotics and Electronics, USA) which is capable of micro stepping with a minimum limit of 0.025° per step. The driver is capable of micro-stepping the motor in increments less than 0.01° per step.

For the circuit protection, improvement on the heating performance in the circuit, and easy control of the RMC, an RMC control console was developed as shown in Figure 24. A control console frame was designed by 3D computer-aided design (CAD) software, solidworks2016 (Dassault Systems SolidWorks Corporation, USA) and was made using a 3D printer (Ultimaker2, Netherlands). With this rotation control console, the RMC rotation can be easily controlled with options on the control mode (automatic/manual) and rotation direction. The control mode can be selected by a toggle switch. First mode is used for manual control which is used for the alignment procedure, and second mode is for the automatic control used in measurement experiments. In the case of automatic mode, the RMC rotates at a designated time period and rotation interval. In addition, the rotation direction (i.e., clockwise or counterclockwise) can also be selected using a tact switch.

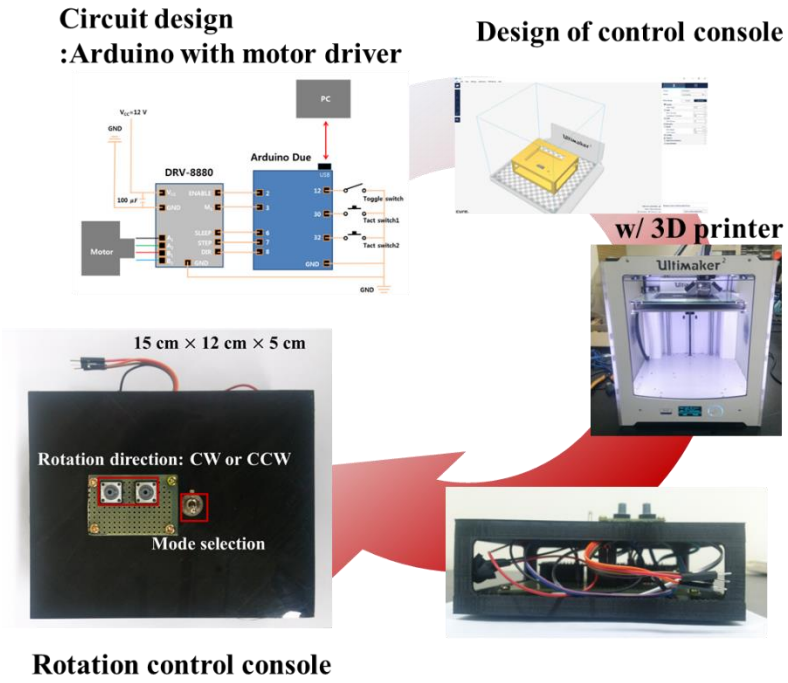

Figure 24. Fabrication process of rotation control console.

Another important consideration is the control software used to provide rotational information of the RMC. In order to operate the Arduino based rotation control console, the control software was developed using Arduino Sketch which is a program written with the integrated development environment (IDE). Moreover, for easy-to-use GUI environment, a serial communication software was developed between Arduino and the computer based on Labview (National Instruments, USA). In the GUI-based software, the rotational information such as current mode, time, rotation direction, rotation interval, and current position is updated in real time, and it is also saved in a text file. A screenshot of the developed rotation control software can be seen in the Figure 25.

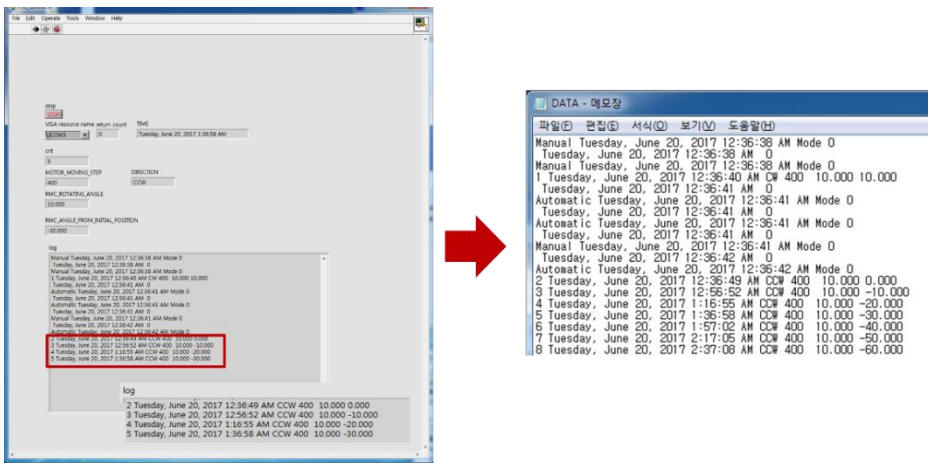

Figure 25. RMC rotation control software.

To validate the rotation control system, the RMC rotation angle was tested physically using a digital protractor and flat bar ($350 \times 70 \times 4$ mm^3) which fits with the mask slit as shown in Figure 26. The flat bar was inserted into a slit at the front mask and was fed through the driver tube and into the corresponding slit on the rear mask. The RMC rotates at a 10° interval, and the indicated angle on the flat bar was measured using a digital protractor at each rotation condition. This test was repeated 5 times, and the rotational system can operate the RMC within 0.1° error.

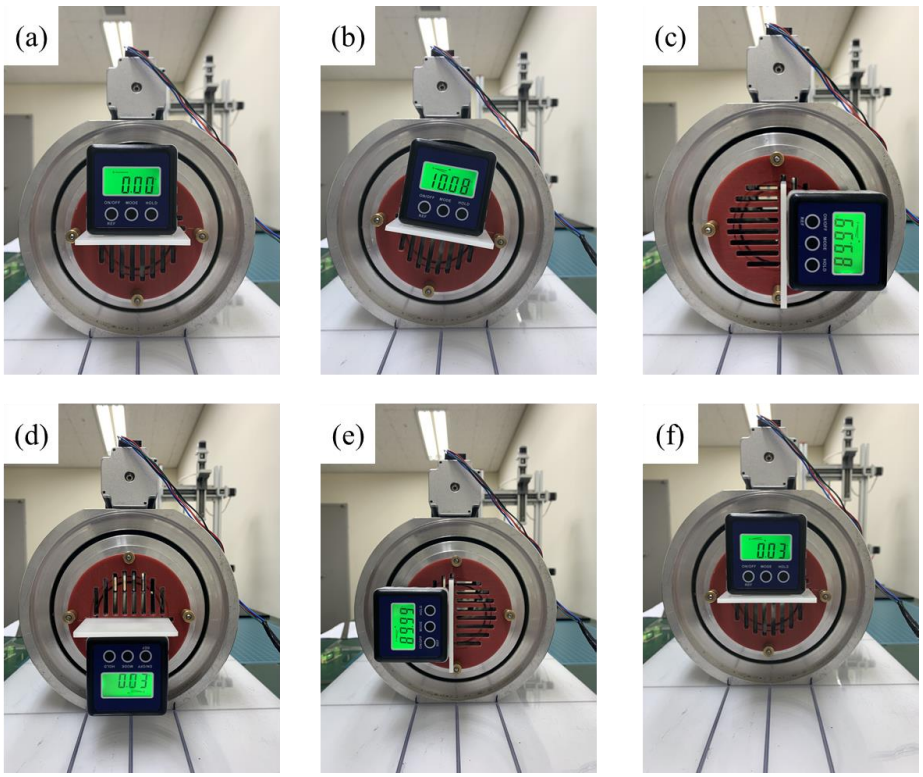

Figure 26. Rotation accuracy test: rotation angle entered in the program (a) 0°, (b) 10°, (c) 90°, (d) 180°, (e) 270° and (f) 360°.

2.3. Image Reconstruction

2.3.1. MLEM based Reconstruction Algorithm

In present study, to convert obtained modulation patterns into 2-D radiation images, the maximum likelihood expectation maximization (MLEM) algorithm was employed. As it uses an iterative method that alternates between expectation and maximization, it is considered to be more robust to high-noise and low-count problems while producing results in a relatively short computing time. For this reason, most of previous RMC works adopted the MLEM algorithm for the image reconstruction [32,33,45].

The MLEM method required a system matrix, which was a pre-determined instrument response for a representation of source distribution. System matrices were generated from the MCNP6.1 simulations or analytical model. The number of pixel was fixed and the pixel interval was determined accordingly to the source-to-mask distances.

The equation for original MLEM is defined as follow:

$$\lambda_j{}^{n+1} = \frac{\lambda_j{}^{n}}{\sum_i a_{ij}} \sum_i a_{ij} \left(\frac{y_i}{\sum_j \lambda_j{}^{n} a_{ij} + b_i} \right) \qquad \text{Eq. (4)}$$

where λ is the value of maximum-likelihood estimation (MLE), a_{ij} is the system matrix (i is the mask position of rotation and j is the source position), y is the measured modulation pattern and b is the background count.

An improved performance of the MLEM-based image reconstruction algorithm using a regularization method has been reported [47]. It could reduce the unnecessary artifacts by assigning an adaptive weight to each pixel.

$$\lambda_j{}^{n+1} = \frac{\lambda_j{}^{n}}{\sum_i a_{ij} + C\frac{1}{\left(\hat{\lambda}_j{}^{*}\right)^{\gamma}}} \sum_i a_{ij} \left(\frac{y_i}{\sum_j \lambda_j{}^{n} a_{ij} + b_i} \right) \qquad \text{Eq. (5)}$$

where $\hat{\lambda}_j{}^{*}$ is the estimated MLE values from the baseline algorithm and C is the tradeoff parameter that controls the sparsity of the solution

For quantitative evaluation of the reconstructed image, the signal-to-noise (SNR) ratio and structural similarity (SSIM) index were calculated [48,49]. The SSIM index can be evaluated from the similarity between two images, and this index lies between 0 and 1. Higher values mean more similarity to the reference

image, indicating better image quality. A noise-free image was set as a reference image, and it has the value of 0 except for only one pixel that has the value of 1 at the actual source location

$$SNR = 10 \cdot \log_{10}\left[\frac{\sum_0^{n_x}\sum_0^{n_y}[t(x,y)]^2}{\sum_0^{n_x}\sum_0^{n_y}[r(x,y)-t(x,y)]^2 \;/\; N}\right] \qquad \text{Eq. (6)}$$

where r(x,y) is the reference image which contains actual source position in the image, and t(x,y) is the test image which contains an expected source position obtained by MLEM and n is the total number of pixels in the image.

2.3.2. Analytical Model of RMC System

As described earlier, the spatial resolution and FOV of the RMC system depends on the system matrix in MLEM algorithm. Therefore, it is important to construct the system matrix widely and densely. To quickly obtain modulation patterns for a wide range of source positions, an analytical model was developed using MATLAB (R 2014a, Mathworks, Inc., Natick, MA, USA) based on design parameters of the RMC system [23]. Analytical patterns for the RMC transmission can be obtained with little computing time, over a wide range of source locations.

The theoretical approach to develop an analytical model follows the similar model presented in the previous study [34]. According to the analytical model, expected counts (y) in the detector can be expressed as an outcome of a Poisson process:

$$\mathrm{y} = Poisson\left\{n \cdot \varepsilon(E) \cdot \frac{\Omega(x,y,z)}{4\pi}\left[P_n(x,y,z) + (1 - P_n(x,y,z)) \cdot e^{-\frac{\mu}{\rho}(E)\cdot\rho\cdot t}\right]\right\} \quad \text{Eq. (7)}$$

where n is the number of particles emitted by the source, $\varepsilon(E)$ is the detector efficiency, $\Omega(x,y,z)$ is the solid angle subtended by the front mask of RMC from the source position, $P_n(x,y,z)$ is the probability that particles will pass

through open slits in the mask at each angle of mask rotation, μ/ρ(E) is the mass attenuation coefficient, ρ is the material density of mask and t is the mask thickness. The detection efficiency $\varepsilon(E)$ was determined from the previous work [38], and the mass attenuation coefficient μ/ρ(E) was taken from the photon cross sections database (XCOM) by National Institute of Standards and Technology (NIST). In order to consider the build-up effect by the complicated attenuation mechanism of photons within the mask, the transmission probability of photons was also calculated using MCNP6.1. Both values turned out to be similar, indicating that contributions from the coherent scattering to the full-energy peak events are negligible. Lastly, $P_n(x, y, z)$ was defined as the ratio of the open slit area made by two masks in accordance with mask rotation, to the total area of the mask.

Modulation patterns obtained with Monte Carlo simulations were compared with the analytic modulation patterns calculated on the basis of the analytical model for the proposed RMC system. Figure 27 shows the results obtained for various source locations. In general, modulation patterns show good agreements between ones that were simulated by MCNP6.1 and ones that were analytically calculated by the analytical model. Better agreements between the two methods can be observed when the source location was assumed to be farther away from the detector face. The results give promises on reconstructing

the modulation pattern, either simulated or experimentally obtained, into an image, using a reconstruction algorithm based on the analytical model.

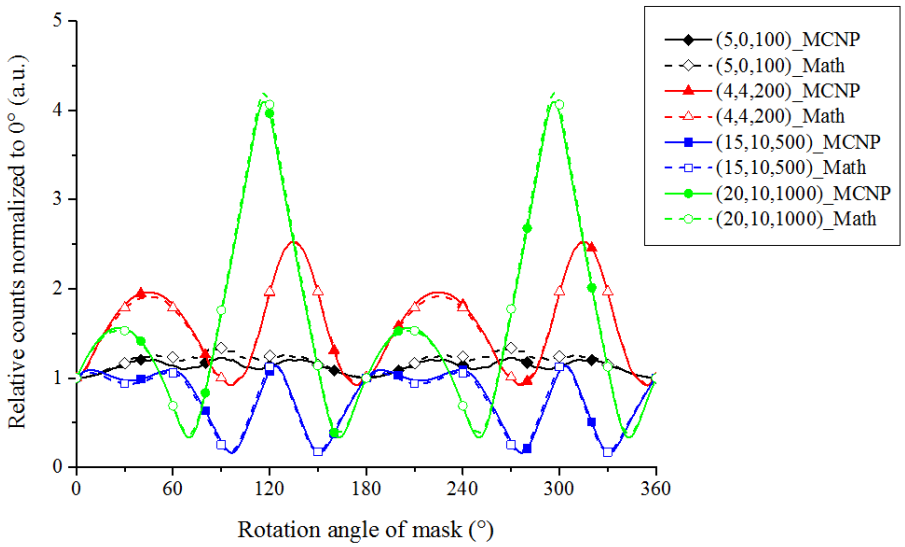

Figure 27. Comparison of modulation patterns obtained by MCNP6.1 and by the analytical (mathematical) model.

On the other hand, slight difference between the MCNP6.1 result and the analytical model result was observed in the modulation pattern for 100 cm (source-to-mask distance) cases. This issue can be explained in terms of the magnification factor (M) [23]. This analytical model is utilizing the universal field model suggested in the previous research. Therefore, when the source is located in the near field region, the projection of rear mask onto the front mask can be de-magnified by a factor of M, thus, the slits size of rear mask are no longer equal to front mask as described in the following equation:

$$M = z \ / \ (z - L) \qquad \text{Eq. (8)}$$

where, z is distance between source to detector, and L is the mask separation distance. If z is far enough or L becomes small, the contribution from magnification factor can be ignored. Meanwhile, spatial resolution (R) of the source location in image reconstruction can be determined by the distance between two slits (s) and the mask separation distance (L) as shown in the following equation:

$$R = \ s \ / \ L \qquad \text{Eq. (9)}$$

Magnification effect and spatial resolution are conflicting factors in

accordance with *L*, thus have to be compromised for optimization. One of other factors affecting discrepancy between the analytic modulation patterns and the MCNP6.1 results is the solid angle. The solid angles subtended by the front mask from the source were 28.15×10^{-4}, 7.06×10^{-4}, 1.13×10^{-4} and 0.28×10^{-4} steradian (sr) for the source positions at (5 cm, 0 cm, 100 cm), (4 cm, 4 cm, 200 cm), (15 cm, 10 cm, 500 cm) and (20 cm, 10 cm, 1000 cm), respectively, and larger solid angle implicates that more particles may be incident on the RMC system in the non-parallel direction. That is, the intensity of parallel beam will be decreased for large solid case, since more portion of the particles are directed to the off-center directions. In case of the analytical model, only a parallel beam was assumed for the simplicity of calculation. Therefore, those two factors mainly have contributed to the disagreement between the analytic modulation pattern and the Monte Carlo simulation results. This presents the limitation of applying the analytical model for the sources located in the near field region. However, this type of localization system is most likely to be used in a mid- to far-field situation. It wouldn't mean too much to use as a radiation imager to find the direction of the radioactive source which is just 100 cm away from the detector. Nonetheless, system matrices in mid-field region (i.e. 100 cm source-to-front mask distance) were constructed using MCNP6.1 simulations.

2.4. Evaluation of the Imaging Capability

2.4.1. Data Acquisition and Image Reconstruction

Before the measurement experiments, the alignment of the collimator mask is important. Slit alignment was accomplished using a flat bar (350×70×4 mm^3) and triangle as shown in Figure 28 (b). The flat bar was inserted into a slit at the front mask and the corresponding slit on the rear mask, and the level was mounted to the flat bar in order to double-check the alignment. The RMC was rotated until the bar was aligned perpendicular to the ground. This configuration was considered to be the initial position of the collimator masks. After setting the initial position, the RMC system measures incoming radiation quanta for a given dwell time, and then, the mask rotates for a certain degree of angle for the next measurement. Using acquired spectra at each rotation angle, the peak area of each characteristic peak specific was calculated to various radionuclides to generate modulation patterns.

For converting the modulation patterns into radiation image of source distribution, the MLEM-based algorithm was used, and the iteration was performed for 5,000 times to assure all calculation were reasonably converge. The original MLEM reconstruction method and MLEM with regularization approach were employed, and regularization method can eliminate the artifact by assigning an adaptive weight to each pixel. System matrices in MLEM were

generated for 11 by 11 pixels, and the pixel interval was set to 2 cm, and they were constructed using MCNP6.1 at 356, 662 keV gamma rays and neutrons, respectively. To calculate the gamma response in CLYC, the pulse height tally (F8) in MCNP6.1 was used to distinguish full-energy absorption events of the gamma rays for 1.0×10^7 histories at each rotational condition with an interval of 1°. For neutron response calculation, the number of tritons created in CLYC was counted using the cell flux tally with the reaction multipliers (F4/FM) tally, and 1.0×10^7 histories at each rotation condition with 1° intervals were simulated. The energy spectrum of neutrons emitted from ^{252}Cf was assumed to follow the Watt fission spectrum, and energy range was set to below the cadmium cut-off energy (0.5 eV).

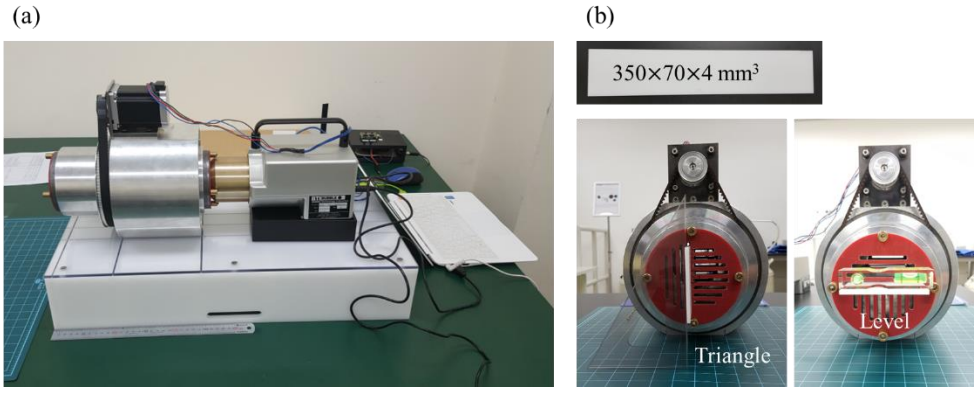

Figure 28. (a) Constructed dual-particle localization system and (b) alignment of the collimator mask.

2.4.2. Localization of Gamma-ray Sources

The reproducibility of source localization was checked using a gamma-ray source. One ^{133}Ba source (R-type, Eckert & Ziegler, Germany) was positioned on the mounting unit, of which the location can be precisely controlled by the program as shown in Figure 29 (a). The rectangular coordinate system is fixed at the front mask face with the x,y plane flush to the front mask face and the z-axis extending out of the mask face. The reference point (0 cm, 0 cm, 0 cm) of the system was set to the rotational axis of the front mask face. The detailed setup information of each experiment are summarized in Table 9.

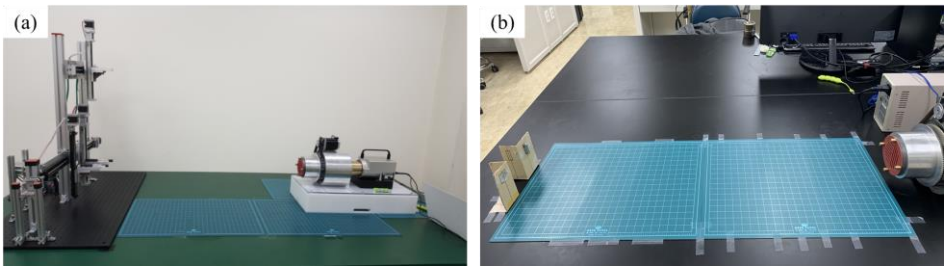

Figure 29. Measurement experiment setup: (a) localization of gamma-ray sources and (b) localization of neutron and gamma-ray sources.

Table 9. Measurement experiment set-up information

Experiment	Used radionuclide	Source position (cm)	Activity (kBq)	Reference date	Dwell time (min)	Rotation interval (˚)
Reproducibility test	^{133}Ba	(2, 0, 0)	393.7	01-Apr-16	20	10
w/ dual gamma-ray sources	^{137}Cs	(5, 0, 0)	378.5	01-Apr-16	40	10
	^{133}Ba	(-5, 0, 0)	393.7	01-Apr-16	40	10
w/ neutron and gamma-ray sources	^{252}Cf	(4,0,100)	3330.0	05-Oct-2015	20	10
	^{137}Cs	(-4,0,100)	1850.0	01-Jan-2018	20	10

Figure 30 shows modulation patterns obtained by MCNP6.1 and by measurements for 356 keV gammas from a ^{133}Ba. In this figure, the dashed line represents MCNP6.1 results, and the solid lines represent measured results. Error bars on each data point indicate 95% confidence intervals calculated from the simulation. Measured modulation patterns showed good reproducibility and well matched with MCNP6.1 simulation results. Reconstructed images also made good estimations on the radiation source location as shown in Figure 31 and Figure 32. The MLEM with regularization provides artifact-free images, and this led to the increase in the values of SNR and SSIM (see Table 10). In reconstructed images, squares show estimated source points obtained by the MLEM algorithm, and the value of MLE is shown in terms of the brightness (black/white). In addition, the black circles indicated the actual source points where the radionuclide was located.

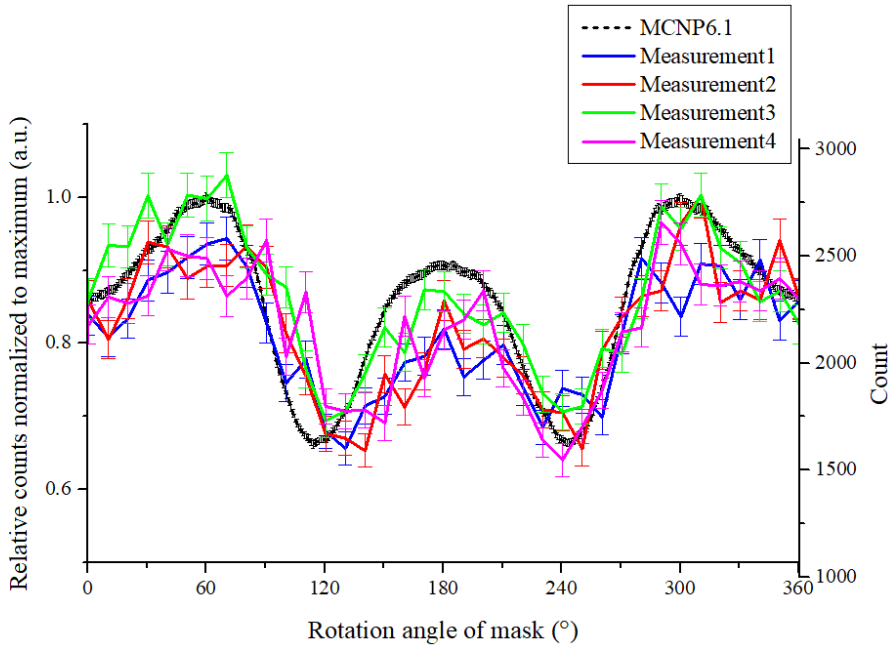

Figure 30. Measured modulation patterns for reproducibility test.

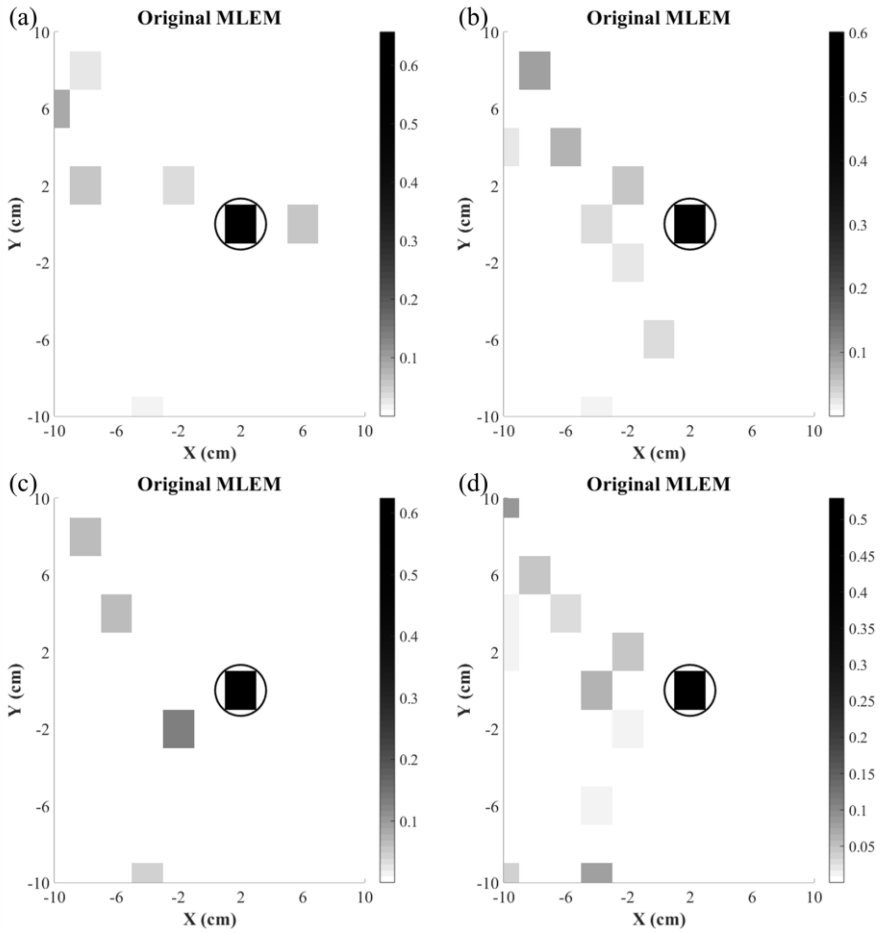

Figure 31. Reconstructed images of measured modulation patterns in Figure 30 using original MLEM: (a) measurement1, (b) measurement2, (c) measurement3 and (d) measurement4.

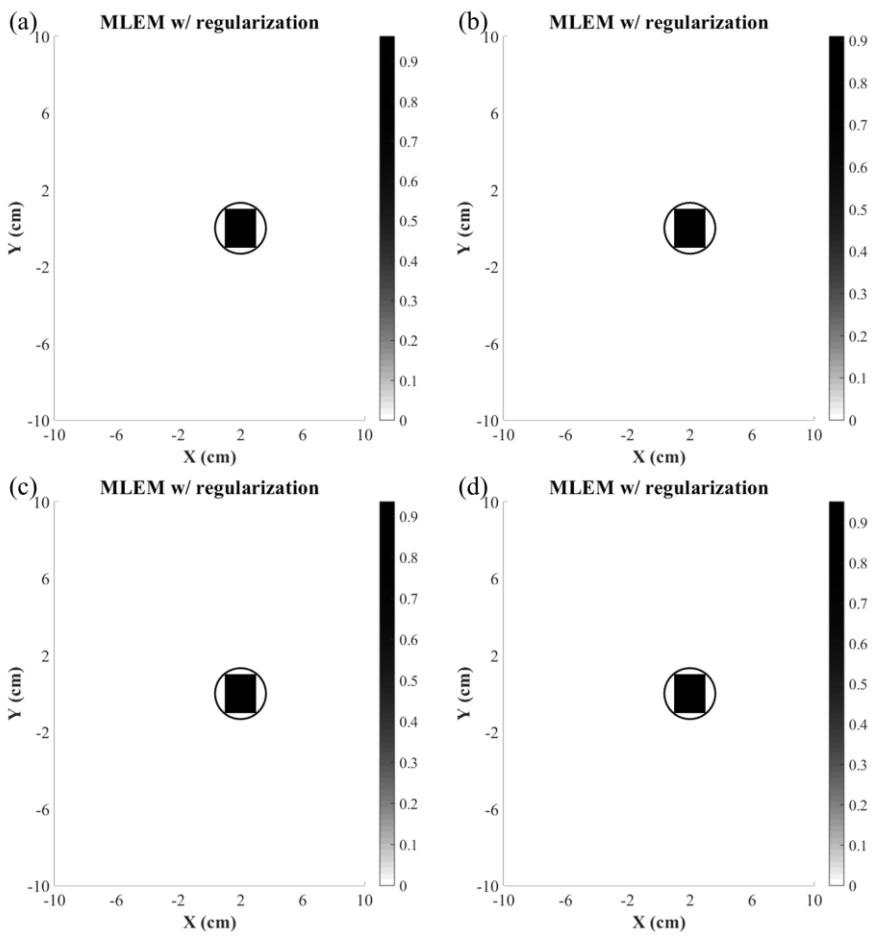

Figure 32. Reconstructed images of measured modulation patterns in Figure 30 using MLEM with regularization: (a) measurement1, (b) measurement2, (c) measurement3 and (d) measurement4.

Table 10. The signal-to-noise ratio (SNR) and structural similarity (SSIM) index results calculated for each case shown in Figure 31 and Figure 32

	SNR		SSIM	
	Original MLEM	MLEM with regularization	Original MLEM	MLEM with regularization
Measurement1	26.06	49.19	0.84	1.00
Measurement2	24.14	40.93	0.82	1.00
Measurement3	24.75	44.01	0.85	1.00
Measurement4	21.75	46.72	0.77	1.00

For further evaluation, two radionuclides were assumed together to test whether they could be visualized in the reconstructed images. Furthermore, a potential possibility to improve spatial resolution was tested by locating the radionuclides in the middle of the pixel interval. In the MLEM approach, the spatial resolution depends on the pixel interval in the system matrix. Since system matrices were constructed with pixel interval of 2 cm, there does not exist pre-determine response at 5 cm apart from reference point (0, 0, 0). However, both algorithm estimated the adjacent position as the true positions, and this indicates that that RMC system has a potential to improve spatial resolution (see Figure 34). In reconstructed images using original MLEM, images of 662 keV show more artifact than 356 keV cases. This is because of the modulation efficiency, which is a relative ratio of the difference between the maximum and minimum peaks in the modulation patterns. As shown in Figure 33, the modulation efficiency of Figure 33 (a) showed ~2.5 times larger than Figure 33 (b) due to superior gamma-ray shielding. When the modulation efficiency is reduced, it will require more counts, because the maxima and minima points in the modulation patterns will be very close together. However, if the MLEM with regularization method was applied, it would be no longer an issue as shown in Figure 34. The quantitative evaluation of images is shown in Table 11 in terms of SNR and SSIM index.

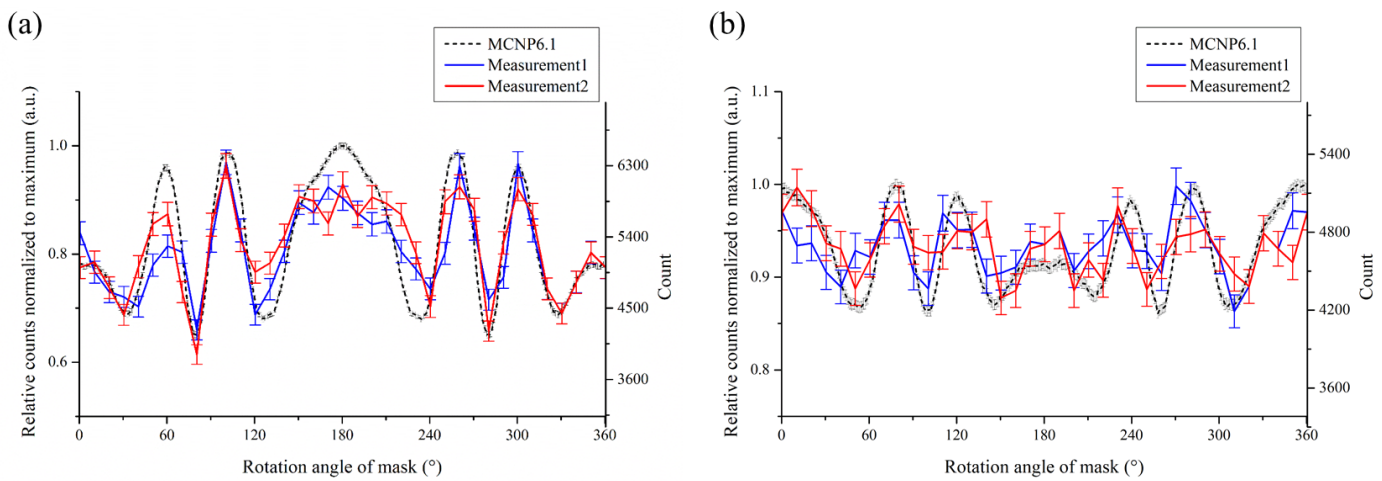

Figure 33. Comparison of modulation patterns obtained by measurement and MCNP6.1 simulation: (a) full-energy absorption peak area of 356 keV gamma ray and (b) full-energy absorption peak area of 662 keV.

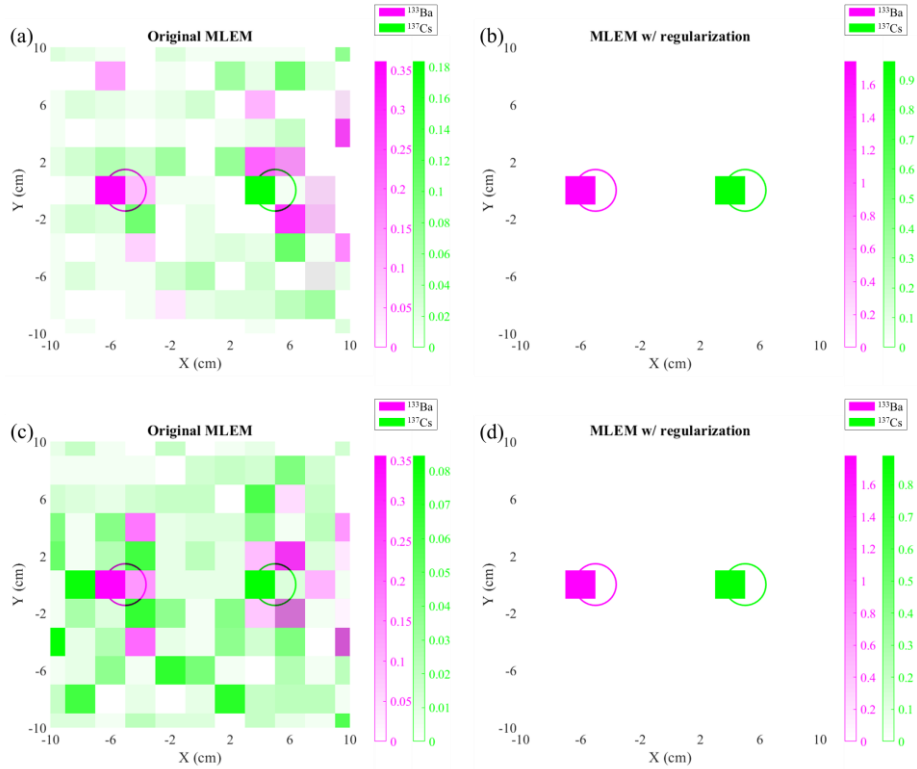

Figure 34. Reconstructed images of measured modulation patterns in Figure 33: (a) measurement1 (original MLEM), (b) measurement1 (MLEM with regularization), (c) measurement2 (original MLEM) and (d) measurement2 (MLEM with regularization).

Table 11. The signal-to-noise ratio (SNR) and structural similarity (SSIM) index results calculated for each case shown in Figure 34

	SNR		SSIM	
	Original MLEM	MLEM with regularization	Original MLEM	MLEM with regularization
356 keV image (Measurement1)	17.04	28.25	0.69	0.98
356 keV image (Measurement2)	16.9	28.00	0.69	0.98
662 keV image (Measurement1)	9.38	49.06	0.63	1.00
662 keV image (Measurement2)	5.98	39.08	0.58	1.00

2.4.3. Localization of Neutron/Gamma-ray Sources

For further evaluation, dual-particle measurement experiments were conducted with a ^{252}Cf and ^{137}Cs radiation sources as shown in Figure 29 (b). The detail setup information of each experiment are summarized in Table 9. Figure 35 shows modulation patterns obtained by MCNP6.1 and by measurements for 662 keV gammas from a ^{137}Cs and thermal neutrons from ^{252}Cf. In this figure, the dashed line represents MCNP6.1 results, and the solid lines represent measured results. Error bars on each data point indicate 95% confidence intervals. As shown in Figure 35, since both measured modulation patterns showed good reproducibility and well matched with one obtained by MCNP6.1, the actual source position was estimated correctly. In addition, the MLEM algorithm with regularization method was able to obtain clear 2-D radiation distribution with no artifacts (see Figure 36). The quantitative evaluation results are summarized in Table 12.

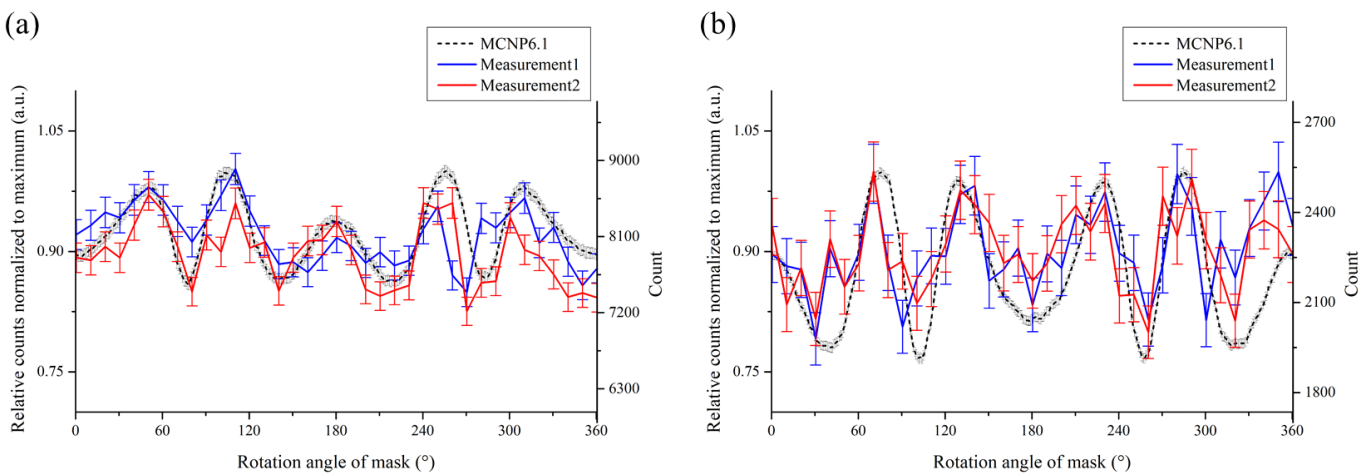

Figure 35. Comparison of modulation patterns obtained by measurement and MCNP6.1 simulation: (a) full-energy absorption peak area of 662 keV gamma ray and (b) thermal neutron peak area.

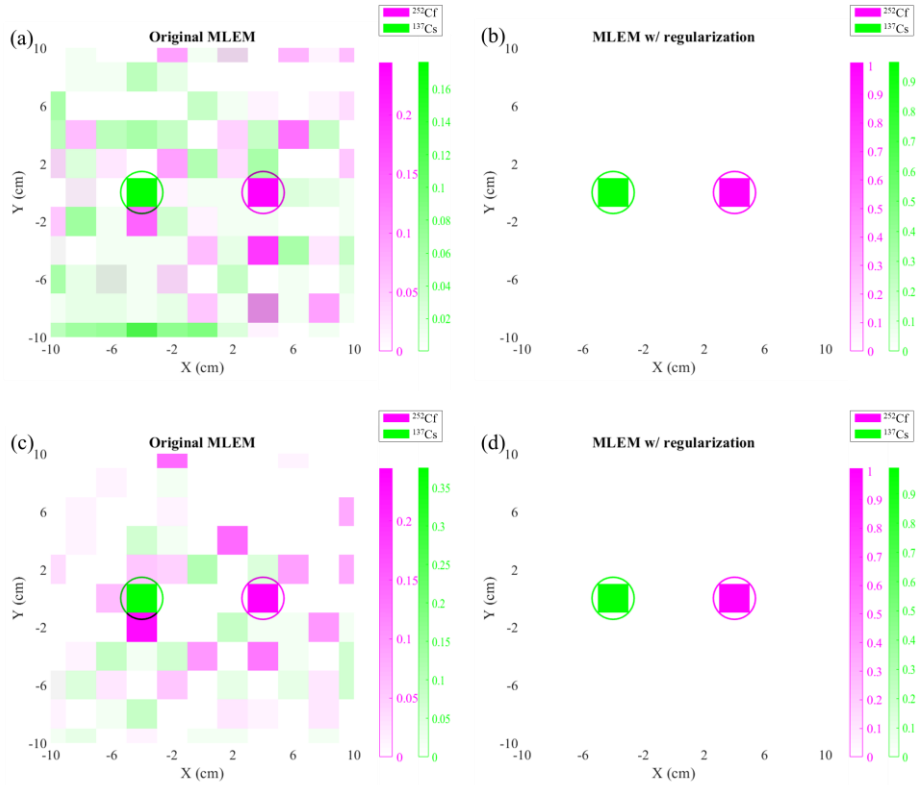

Figure 36. Reconstructed images of measured modulation patterns in Figure 35: (a) measurement1 (original MLEM), (b) measurement1 (MLEM with regularization), (c) measurement2 (original MLEM) and (d) measurement2 (MLEM with regularization).

Table 12. The signal-to-noise ratio (SNR) and structural similarity (SSIM) index results calculated for each case shown in Figure 36

	SNR		SSIM	
	Original MLEM	MLEM with regularization	Original MLEM	MLEM with regularization
662 keV image (Measurement1)	9.12	49.70	0.63	1.00
662 keV image (Measurement2)	16.21	60.70	0.75	1.00
Neutron image (Measurement1)	12.54	59.31	0.68	1.00
Neutron image (Measurement2)	13.14	61.31	0.67	1.00

2.5. Additional Considerations for Practical Applications

Coupled with an appropriate reconstruction approach, RMC-based localization system is capable of achieving 2-D distribution of neutrons and gamma rays, and the specifications of dual-particle localization system are presented in the Table 13 and 14.

Table 13. Specifications of the dual-particle localization system (a)

Performance specification of radiation source localization system			
Field of view		18° × 18° (cross-sectional view × longitudinal-sectional view)	
Angular resolution		0.95°	
Data acquisition time (sensitivity)		Localize point source of ^{137}Cs producing ~50 μR/hr in < 10 min	
CLYC crystal size		5.08 cm (diameter) × 5.08 cm (height)	
Energy range		300 keV – 3 MeV (Gamma ray), thermal neutron	
Energy resolution		5.6% (@ 662 keV gamma ray)	
Intrinsic detection efficiency	Gamma ray	356 keV	28.1%
		662 keV	14.8%
		835 keV	11.8%
		1173 keV	8.1%
		1275 keV	7.8%
		1333 keV	7.4%
	Neutron	thermal neutron: ~80% (provided by Bubble Technology Industries)	
		^{252}Cf: 28% (w/ 6 cm-thick HDPE moderator)	

Table 14. Specifications of the dual-particle localization system (b)

System Specifications / Rotation Control System Performance		
Dimensions		50 cm × 20 cm × 25 cm (including CLYC detector)
Weight		~25 kg (including CLYC detector)
Collimator	Pb	Purity 99.95% (Semyoung metal, Korea)
	BPE	Density 1.11 g/cm^3, higher hydrogen content >115 g/liter, the boron content >56 g/L (Dynex, Korea)
Minimum rotation angle		0.025 °/step
Maximum rotation speed		44.4 step/s
Maximum holding torque		3.1 Nm
Maximum torque		2.4 Nm
Rotation accuracy		< 0.1%
Power supply		-RMC rotation control system: External voltage 12V, USB cable 5V -CLYC detector: External voltage 220V

However, data acquisition time is still one of the issues for practical application. Therefore, further validation was performed by measurement experiment to check sensitivity of the localization system. A ^{137}Cs gamma-ray source with an activity of 962.4 kBq was used to check the morphology change in the modulation patterns according to the dwell time increase, and it was located at (-4 cm, 0 cm, 100 cm) which producing 5.2 uR/hr at the RMC system. As shown in Figure 37, the shorter the dwell time, the greater the difference between the measurement and simulation results; however, if the measurement time is increased, the measured patterns converge similar to the modulation pattern obtained by MCNP6.1. Even when the modulation pattern was obtained with short dwell time, which was set to 2 minutes, the localization system coupled with reconstruction algorithm could provide accurate source position as shown in Figure 38. In addition, MLEM with regularization shows an artifact-free image that can clearly recognize the true source position. However, if the dwell time was reduced to less than 2 minutes, the reconstruction algorithm estimated the wrong source position, and the RMC system could not localize radioactivity correctly (see Figure 39). Thus, by using the experimental results to calculate the sensitivity (i.e. 2 minutes of dwell time), the RMC system was found to be able to localize a ^{137}Cs point source producing 5.2 uR/hr

within 75 minutes and its required time can be reduced proportionally with the exposure rate.

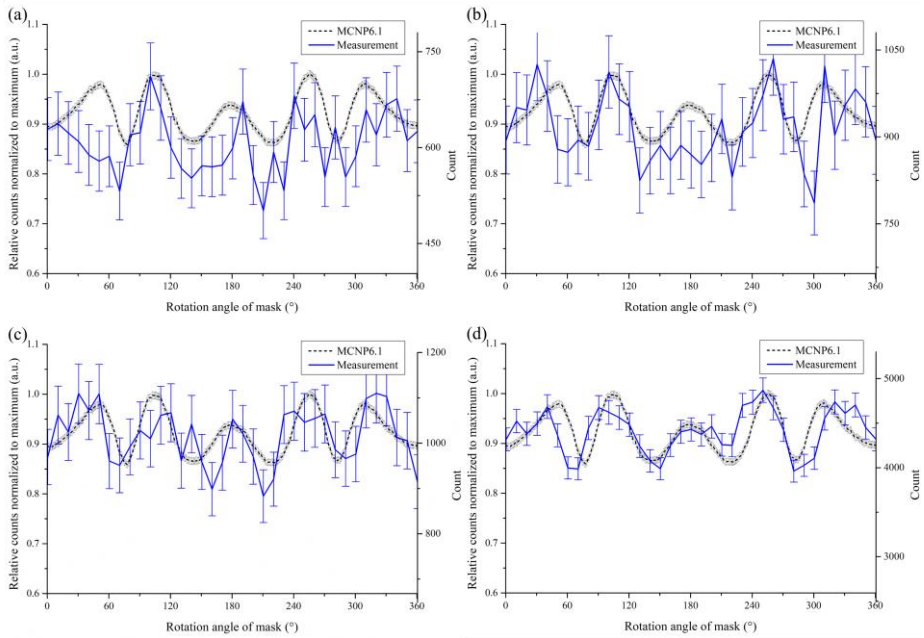

Figure 37. The morphology change in the 662 keV measured patterns with the increase of dwell time: (a) 2 min, (b) 3 min, (c) 5 min and (d) 40 min at each rotation condition.

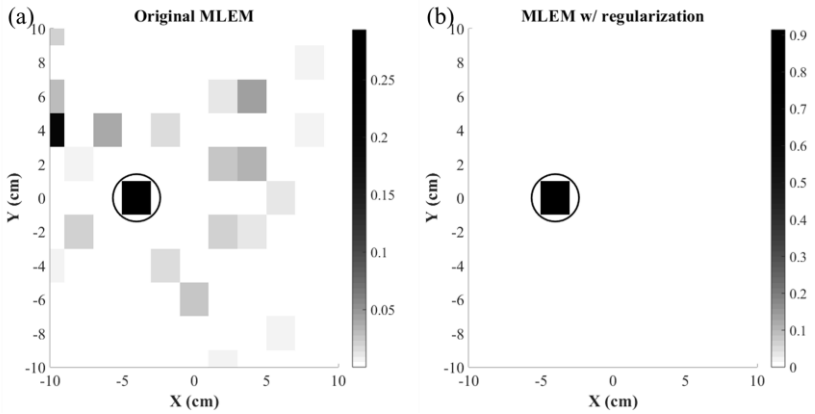

Figure 38. Reconstructed images of measured modulation patterns in Figure 37 (a): (a) original MLEM and (b) MLEM with regularization.

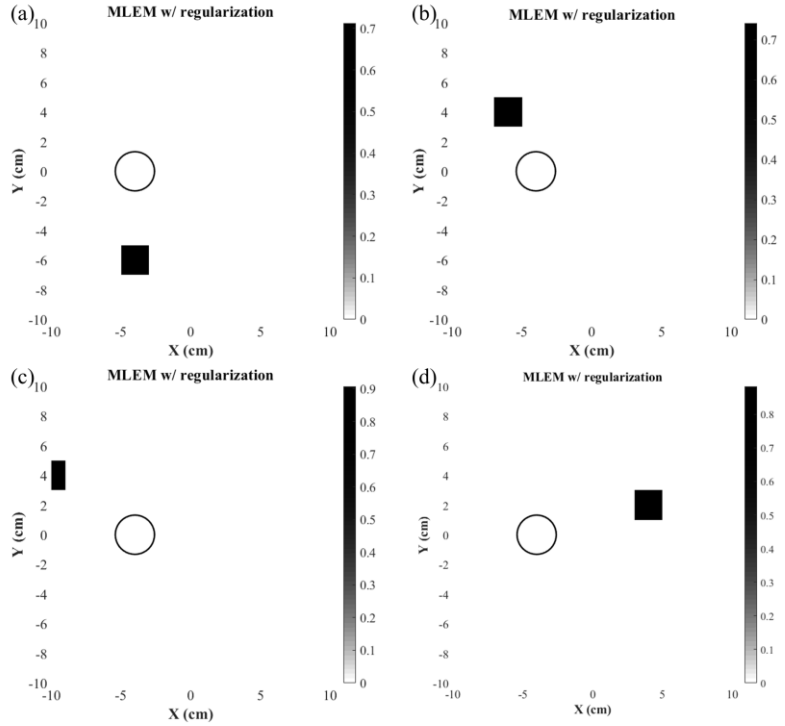

Figure 39. Estimated source position in reconstructed images: (a) 10 sec, (b) 20 sec, (c) 60 sec and (d) 90 sec dwell time at each rotation condition.

Another practical issue is the construction of the system matrix in the MLEM algorithm. The spatial resolution for MLEM method depends on the pixel interval in the system matrix. Constructing the system matrix densely can improve the spatial resolution, however, it requires too much time using Monte Carlo simulation used in present study. To overcome shortcomings of the time-consuming Monte Carlo approach, an analytical model was proposed to quickly obtain modulation patterns for a wide range of source positions. When the source was assumed to exist relatively near the detector face (i.e. 100 cm source-to-front mask distance), Monte Carlo simulated patterns and analytical patterns at each source location tended to show discrepancies due to the magnification effect and the parallel beam approximation. Considering practical application based on RMC system, this type of device is most likely to be used in a mid-range (1-20 meters) or far-field situation where analytical model can be applied to construct system matrix densely. Figure 40 shows the comparison results between measurement, MCNP6.1 and the analytical model developed by MATLAB when the ^{133}Ba source of 3312.2 kBq was located at (-6 cm, 0 cm, 150 cm). Modulation patterns showed good agreements between measurements and simulated patterns obtained by MCNP6.1 and analytical model. This indicates that accurate system matrices can be constructed by analytical model, and it means that spatial resolution of RMC system can be

improved. Based on the analytical model, the system matrix was built at 150 cm source-to-front mask distance case, which has pixel interval of 0.75 cm. As shown in Figure 41, the actual source position was estimated correctly in the reconstructed images. These results demonstrate the possibility of utilizing the RMC system for practical application.

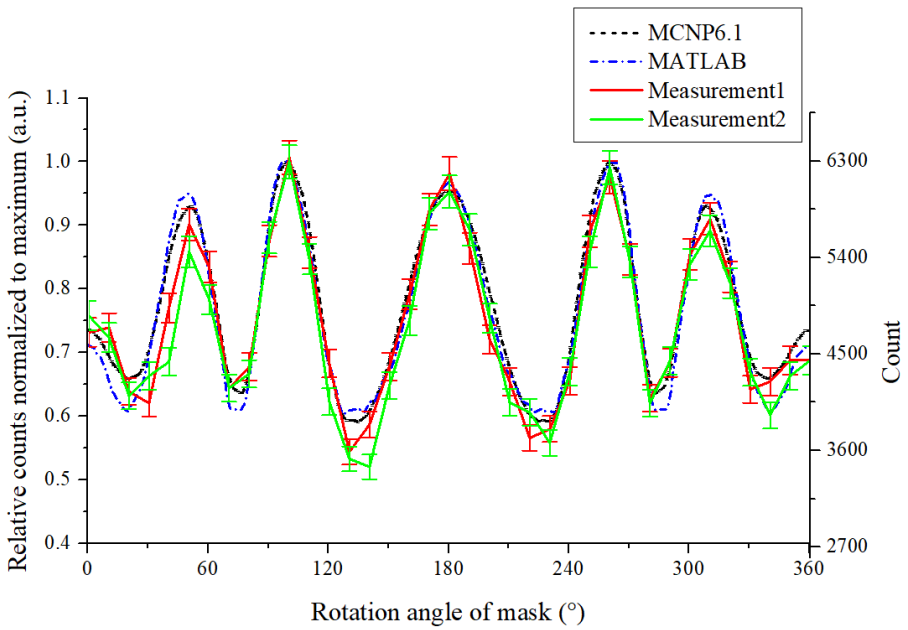

Figure 40. Comparison of modulation patterns obtained by measurement, MCNP6.1 simulation and MATLAB. Dwell time was set to 10 minutes in the measurements.

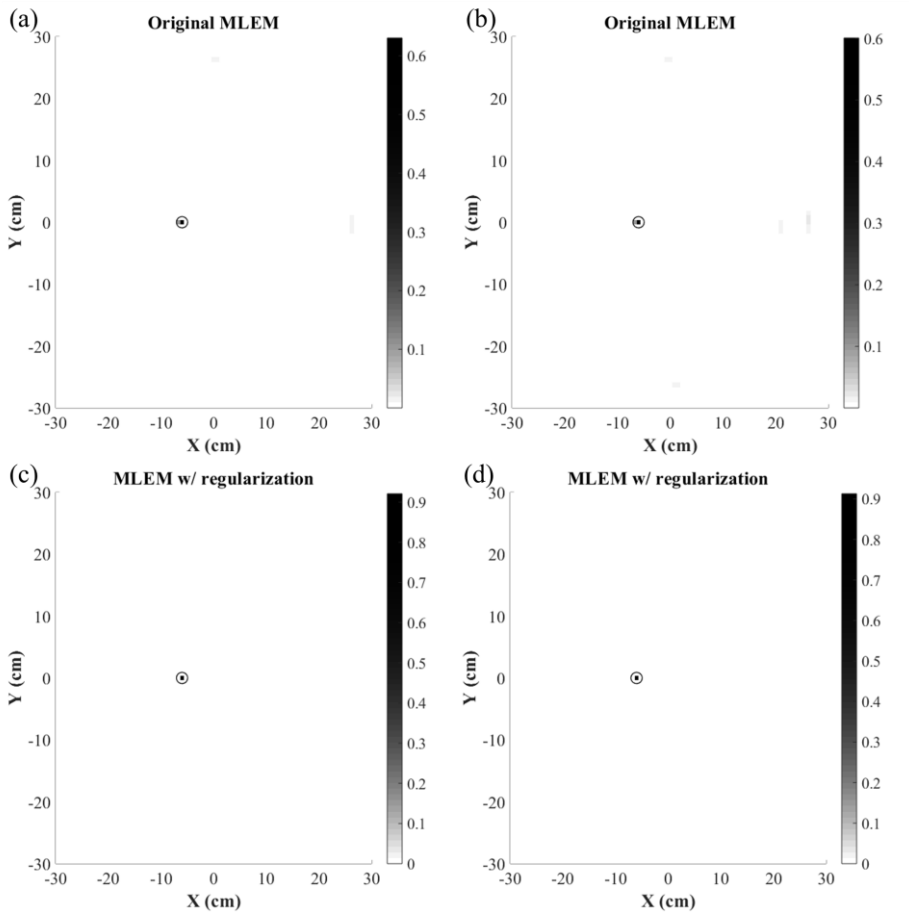

Figure 41. Reconstructed images of measured modulation patterns in Figure 40: (a) measurement1 (original MLEM), (b) measurement2 (original MLEM), (c) measurement1 (MLEM with regularization) and (d) measurement2 (MLEM with regularization).

Chapter 3. Extension of the Field of View for RMC System

3.1. Hemispherical RMC System Design

3.1.1. Optimization of Collimator Mask Design

The mask geometry determines the FOV of the RMC system (refer to Fig. 42), and imaging performance of the system depends on its design parameters. The morphology of the modulation patterns is mainly influenced by the distance between two masks and by the slat/slit configuration. Because an RMC system localizes sources by the difference in pattern morphology, the maximum and minimum points on the patterns should be clearly distinguishable. In this regard, Monte Carlo simulations were performed to investigate a favorable mask design by adjusting a few design parameters for hemispherical RMC (H-RMC).

To evaluate the influence of the slat and slit intervals and outer-to-inner mask distance on the modulation patterns, the modulation patterns for typical source locations at different mask configurations were acquired by MCNP6.1 simulations. With the external collimator fixed at a radius of 9.5 cm, both slat/slit intervals were changed from 4° to 7° and 10° while maintaining the inner mask radius on to 2.5 cm, and then, selected one that appeared to be optimal. Furthermore, the inner mask radius was changed from 2.5 cm to 5 cm and 7.5 cm at each slat/slit case to investigate its influence on the modulation pattern.

The simulation was performed assuming 0.5 cm-thick lead (Pb) collimator masks surround a 1 × 1 × 1 cm^3 CdZnTe (CZT) detector as shown in Figure 42 (b). In order to focus on investigating behavioral characteristics of the resulting modulation patterns depending on the aforementioned design parameters, a low-energy point source emitting 356 keV gamma rays was assumed, which can be mostly blocked by the 0.5 cm-thick Pb collimators, in the simulations. To calculate the gamma response of the CZT, the pulse-height tally (F8) in MCNP6.1 was used to distinguish full-energy absorption events of the gamma rays in the CZT detector for 1.0 × 10^7 histories at each rotational condition with an interval of 1°.

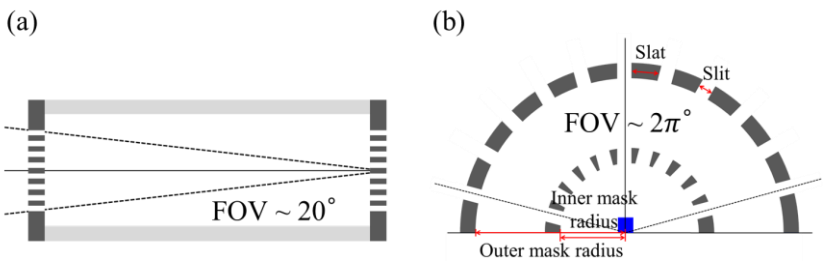

Figure 42. A schematic of RMC systems: (a) conventional RMC and (b) hemispherical RMC. The blue square illustrates a radiation detector.

In order to evaluate the localization performances depending on the collimator mask design of H-RMC, the following four factors were compared: 1) modulation efficiency of the simulated patterns, 2) open-to-total area ratio of the masks, 3) nominal angular resolution defined by the mask geometry and 4) sensitivity of pattern morphology. In the RMC technique, the number of ripples and their specific shapes in the modulation patterns depend on the position of the radiation source. Since the source position was estimate based on the difference between the shape of the measured modulation patterns, each pattern should be easily distinguishable from noises and ones that can be obtained from other positions. In this regard, one would desire modulation patterns which exhibit large differences between the maximum and minimum points, making the characteristic feature of the pattern more distinctive. A quantitative parameter, modulation efficiency, is the relative difference between maximum and minimum counts in the modulation pattern with respect to the maximum count and was calculated [33,46].

Another key factor is the total number of counted particles from the detector. As one of concerns for the RMC technique is the sensitivity of the imager limited by the collimation, one needs to consider the open-to-total area ratio of the masks to achieve adequate sensitivity [14,15]. When the open area made by the slits is large, more particles can pass through the slits of the mask, which

subsequently increases the number of particles counted on the detector. Therefore, the open-to-total area ratio can indirectly represent the overall intrinsic detection efficiency of the RMC system, and is defined as the ratio between the open area and the total area of the collimator mask. Next, the nominal angular resolution of the imager was considered. Conventionally, the nominal angular resolution of the RMC system has been mathematically defined by the ratio of the slit width to the separation distance between the masks [23,33]. The angular resolution was investigated, which was determined by the mask design while changing both the slit width and the separation distance to optimize the mask design for the H-RMC system.

An additional factor to evaluate the performance of the collimator design is the sensitivity of pattern morphology when an additional radiation source is added in the adjacent position. To evaluate the sensitivity of pattern morphology for each mask design, double point sources was assumed, which are half angle of the nominal angular resolution (R/2) apart from each other (i.e. (100 cm, 30°, 0°) and (100 cm, 30° + R/2, 0°)). For quantitative evaluation of morphology change, root mean square deviation (RMSD) was calculated between patterns obtained by a single point source and double point sources. The RMSD was calculated at each rotation condition with an interval of 1°, and then, averaged all 360 values.

A series of Monte Carlo simulations were performed while varying the slat/slit interval widths and inner mask radius as described above. The property of the modulation pattern was evaluated for each design condition by calculating the modulation efficiency at typical source positions such as (100 cm, 30°, 0°) and (100 cm, 60°, 0°). The results of the quantitative evaluation are shown in Table 15. As the system had a longer slat/slit interval or a larger inner mask radius, relative differences between the maxima and minima counts became more significant. This made the features of the modulation pattern much more distinguishable judging by the appearance of pattern (see Table 15). In addition, modulation efficiencies showed a similar trend in the other source positions. In general, the modulation efficiency increased substantially as increasing the slat/slit interval and inner mask radius.

Table 15. Modulation efficiency values for various mask designs at typical source points: P1 (100 cm, 30°, 0°) and P2 (100 cm, 60°, 0°)

Inner mask radius (cm)	Slat/slit interval: 4°		Slat/slit interval: 7°		Slat/slit interval: 10°	
	P1	P2	P1	P2	P1	P2
2.5	0.56	0.47	0.79	0.80	0.81	0.79
5.0	0.51	0.50	0.87	0.83	0.93	0.87
7.5	0.57	0.49	0.94	0.92	0.96	0.93

Another key factor to consider in the collimator mask design is the angular resolution which is expected to change depending on the slat/slit interval and the inner mask radius. Nominal values of the angular resolution that can be mathematically calculated from the mask design are shown in Table 16. Meanwhile, the ratio between the open area and the total area of the mask, which is directly related to nominal sensitivity of the imager, did not show large variations depending on the slat/slit interval.

Table 16. Nominal angular resolution and open-to-total area ratio calculated for each design condition

Slat/slit interval (# of slit)	Inner mask radius (distance between masks, L)					
	2.5 (L=6.5)		5.0 (L=4)		7.5 (L=1.5)	
	Angular resolution	Open area / Total area	Angular resolution	Open area / Total area	Angular resolution	Open area / Total area
4° (20)	6.1°	0.44	10.7°	0.44	15.0°	0.44
7° (12)	9.9°	0.47	17.0°	0.47	23.6°	0.47
10° (8)	25.0°	0.44	39.2°	0.44	49.3°	0.44

Since the RMC system estimates the source position based on morphology of modulation patterns, distinguishable differences will lead to accurate estimation in reconstructed images. Therefore, it can be regarded as a good design to make larger difference on modulation patterns in case where the additional source was added in an adjacent position. Simulation results for slat/slit interval of 7° in Table 17 show generally higher RMSD values, which indicates that the pattern arising from two adjacent source positions can be evaluated accurately.

Based on the results, a 2.5 cm-radius inner mask with a slat/slit interval of 7° would be a good compromise between the modulation efficiency, the angular resolution, the open-to-total area ratio and sensitivity of pattern morphology.

Table 17. Sensitivity of pattern morphology evaluated by root mean square deviation between typical point (S) and its adjacent point: S1 (100 cm, 30°, 0°) and S2 (100 cm, 60°, 0°)

Inner mask radius (cm)	Slat/slit interval: 4°		Slat/slit interval: 7°		Slat/slit interval: 10°	
	S1	S2	S1	S2	S1	S2
2.5	0.15	0.17	0.23	0.32	0.27	0.27
5.0	0.16	0.10	0.31	0.30	0.20	0.12
7.5	0.11	0.04	0.25	0.08	0.17	0.18

3.1.2. Spectroscopic and Mechanical Performance

The H-RMC system mainly consists of collimator masks, a driver tube with bearings, timing pulley/belt and servo motor. The collimator mask is the most important part of RMC technique, and the performance of the imager depends on its design. Based on MCNP6.1 simulation results, the bilateral symmetric mask was fabricated with the optimized slat/slit configuration and size. The interval of both slats and slits was set as 7° and the radius of inner/outer mask as 2.5 cm and 9.5 cm, respectively. In fact, it would be better if it was fabricated using a high-Z material for an effective gamma-ray shielding. However, because of mechanical challenges in the machining process, the prototype was fabricated with a stainless steel based 303 alloy using the wire cutting process, and the thickness of masks was decided to be 0.5 cm.

Considering the size of the detector at the core, a UCP312 bearing unit (MISUIMI, USA) with an internal diameter of 60 mm was chosen. The driver tube was designed with an external diameter of 60 mm and an internal diameter of 48 mm, and the tube was designed to allow easy attachments and detachments of the collimator mask. Therefore, various designs of masks can be easily applied to the H-RMC system, and any type of radiation detectors can be used for RMC as long as their diameter is less than 48 mm.

For rotating masks, the HF-KP053 servo motor (Mitsubishi, Japan) was selected, which allows precise angle control and provides sufficient torque. It has a control resolution of 262,144 pulse/revolution and a maximum torque of 0.48 N·m. In addition, timing pulley and belt were mounted onto the driver tube and servo motor, which was used to transmit the power from a servo motor to rotate the H-RMC. A timing pulley was designed to provide with the conversion factor of 6 to 1 from the motor pulley to the driver tube pulley. Therefore, the motor pulley has to rotate 6° in order to rotate the H-RMC by 1°. Detailed information on the fabrication of H-RMC and its mechanical performance was reported in the previous work [50].

The performance of the RMC-based imager is mainly determined by 1) characteristics of the radiation detector, 2) design of the collimator mask and 3) accuracy of RMC rotation control system. In H-RMC system, a CPG-type CZT detector was used which can be operated at the room temperature without a special cooling system and its schematic configuration is shown in Figure 43. The CPG-type CZT detector stands on as an integrated form including a customized preamplifier inside the detector body. The signal from the preamplifier was amplified and shaped using an Ortec 572A amplifier (Ametek Ortec, USA) with a setting of 0.5 μs shaping time and gain value of 50. The output signal from the amplifier was connected to an Ortec EASY-8K

multichannel analyzer (Ametek Ortec, USA). An Ortec 556 high voltage power supply (Ametek Ortec, USA) was used to bias the CZT detector and was set to -1000 V. With this configuration, the measured energy resolution was 4.4% and 3.7% at 356 keV and 662 keV, respectively. The intrinsic peak efficiency of the detector was determined to be 66.8%, and 22.8% for 356 keV gammas from ^{133}Ba and 662 keV from ^{137}Cs, respectively.

Based on the results from the mask optimization study, a hemispherical mask was fabricated with the slat/slit interval of 7°, of which the separation between the inner mask and the outer mask was 6.5 cm. Both outer and inner masks consisted of 13 slats and 12 slits. Each slit and slat was in the form of a spherical wedge shape which was a portion of a sphere bounded by two semi-disk planes and a spherical lune, and the angle of the wedges was 7°. Since the first and last wedges at the bottom of inner mask had a wedge angle of 9.5°, the H-RMC system had an FOV of approximately 160° in the cross-sectional plane. In addition, the nominal angular resolution of the imager was calculated to be approximately 10°, from the slat/slit width and outer-to-inner mask distance. The collimator masks were designed to be able to rotate at a rate of 1° per second using a servo motor for effective operation at high-level radiation environment, and the rotation system can operate the H-RMC within 0.1° error by a proportional–integral–derivative controller (see Figure 44) [50].

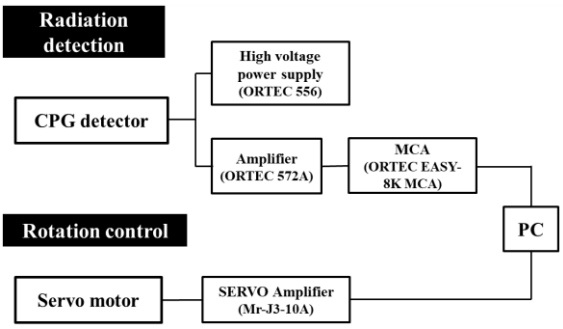

Figure 43. A block diagram of radiation detection and rotation control system configuration in H-RMC system.

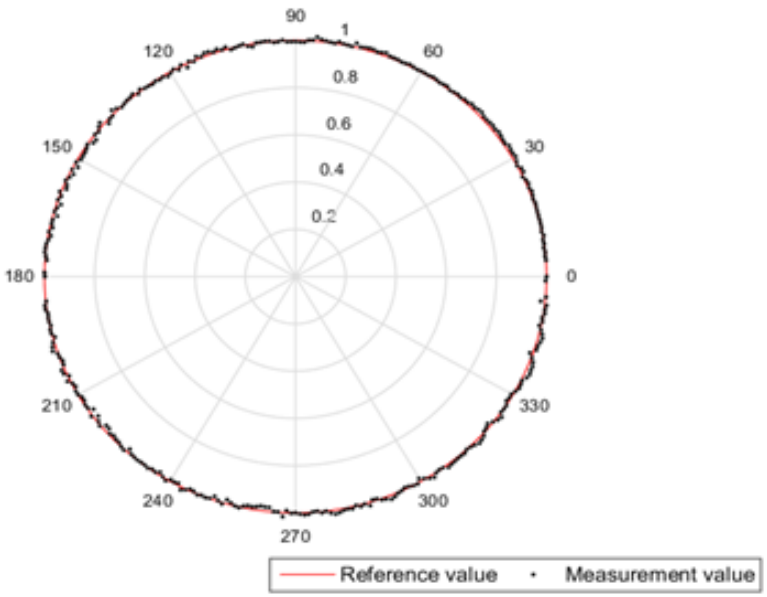

Figure 44. Rotation accuracy test using digital protractor: reference value indicates rotation angle entered in the program [50].

3.2. Evaluation of the Imaging Capability

3.2.1. Data Acquisition and Image reconstruction

Before the measurement experiments, the alignment of the collimator mask is important. Slit alignment was accomplished using an alignment tool (135×210×5 mm^3) and rectangular box as shown in Figure 45 (a). After the alignment tool was mounted to match the center of the mask with the reference line on the tool (see Figure 45 (b), the RMC was rotated until the tool was aligned vertically in the rectangular box (see Figure 45 (c). Then, the level was mounted to the alignment tool in order to double-check the alignment (see Figure 45 (d). This configuration was considered to be the initial position of the collimator masks. After setting the initial position, the H-RMC system measured incoming radiation quanta for a given dwell time, and then, the mask rotated for a certain degree of angle for the next measurement. Using acquired spectra at each rotation angle, the peak area of each characteristic peak specific was calculated to various radionuclides to generate modulation patterns.

For converting the modulation patterns into radiation image of source distribution, the MLEM-based algorithm was used, and the iteration was performed for 1,000 times to assure all calculation were reasonably converge. The original MLEM reconstruction method and MLEM with regularization approach were employed. System matrix was built using MCNP6.1 in the

spherical coordinate system; the radial distance of the source from the detector (r) was set to 50 cm, varying polar angle (θ) and azimuth angle (φ) coordinates with 10° intervals at 356 and 662 keV gamma rays, respectively.

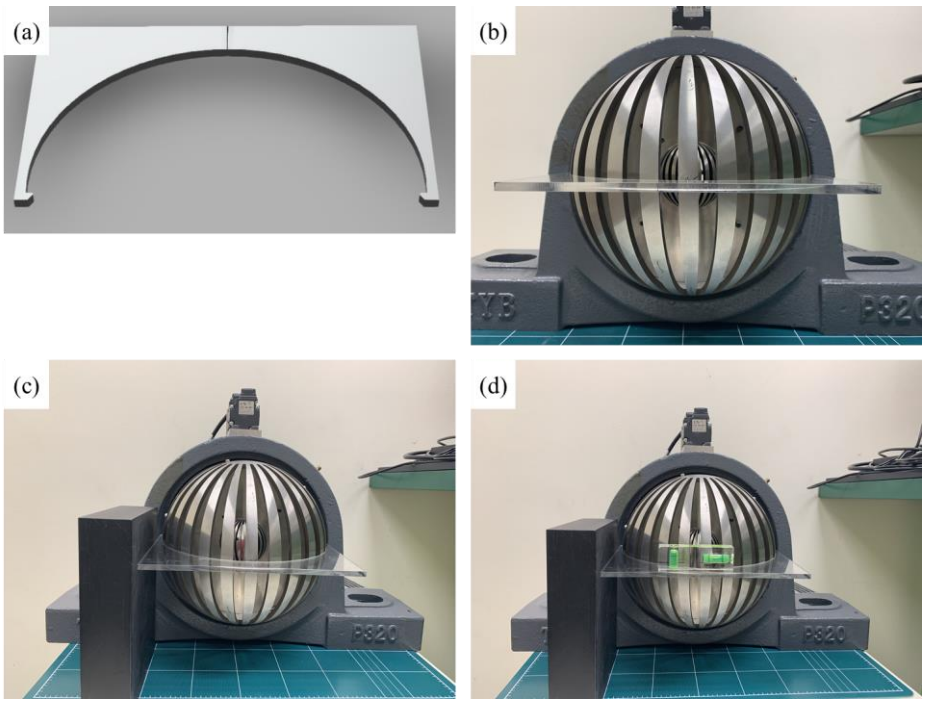

Figure 45. Alignment of the collimator mask using an alignment tool: (a) attachment of the alignment tool, (b) initial position setting and (c) double-check using level.

3.2.2. Localization of Single Gamma-ray Source

For testing the imager performance, measurements were conducted with ^{133}Ba and ^{137}Cs gamma-ray sources as shown in Figure 46. The experiment for two different shapes of source was also performed to assess the effect of source geometry on the imager (see Table 18).

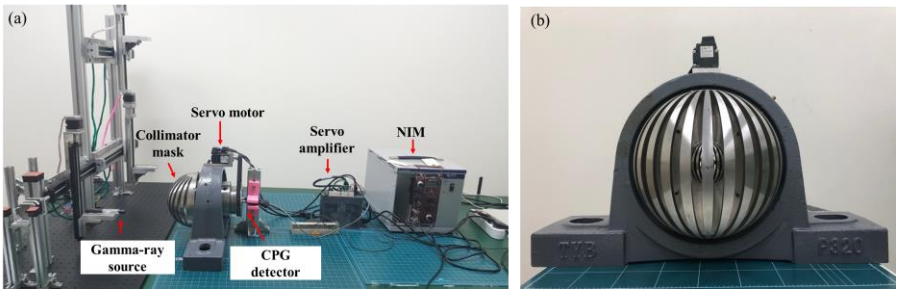

Figure 46. H-RMC system: (a) measurement experiment setup and (b) front view of H-RMC system.

Table 18. A list of gamma-ray sources used in the experiment

Radionuclide	Source type	Activity (kBq)	Reference date
^{133}Ba	R-type (rod source)	393.7	01-Apr-16
	D-type (disk source)	3312.2	01-Aug-18
^{137}Cs	D-type (disk source)	962.4	01-Aug-18

Figure 47 shows modulation patterns obtained by MCNP6.1 and by measurements for 356 keV gammas from a ^{133}Ba source of 393.7 kBq. In this figure, the dashed line represents MCNP6.1 results, and the solid lines represent measured results. Error bars indicate 95% confidence intervals on the results. With a dwell time set to 60 minutes and a rotation interval of 10°, gamma-ray spectra were obtained, and the full-energy photopeak at 356 keV was calculated. Two measured modulation patterns showed the similar trend over the full rotation angles. The maximum and minimum points on the normalized patterns shown in Figure 47. were approximately in agreement between measured and simulated results. Since system matrices in MLEM methods were based on MCNP6.1 simulations, this agreement guaranteed the quality of the reconstructed images.

Figure 48 shows the reconstructed images of the measured modulation patterns using the original MLEM algorithm and the MLEM algorithm with regularization method. The painted pixels marked estimated source positions obtained by the reconstruction algorithm, and the circles indicated the actual source points where the radionuclide was located on the source positioning system. As shown in Figure 48, both algorithms estimated two symmetric points as the true source position due to the bilateral symmetry of the mask pattern, and further estimated values of maximum likelihood estimation (MLE)

appeared the same for the two points. Using this slat/slit configuration, modulation patterns obtained from two symmetrically located sources to the rotation axis appeared the same, (i.e. (25 cm, 30°, 0°) and (25 cm, 30°, 180°)). Therefore, it is difficult to distinguish one from the other in the reconstructed image.

As shown in the reconstructed images, the MLEM with regularization shows less noises that were misrecognized as true than the original MLEM method. As shown in Figure 48 (c) and (d), reconstructed images using the regularization technique still had the intrinsic artifact due to symmetric slat/slit configuration, but neither other noise nor artifact were observed, which led to the increase in the values of SNR and SSIM for 356 keV gammas (Table 19).

Table 19. The signal-to-noise ratio (SNR) and structural similarity (SSIM) index results calculated for each case shown in Figure 48

Single source environment	SNR		SSIM	
	Original MLEM	MLEM with regularization	Original MLEM	MLEM with regularization
Measurement1	22.91	24.44	0.96	0.97
Measurement2	22.36	23.12	0.95	0.96

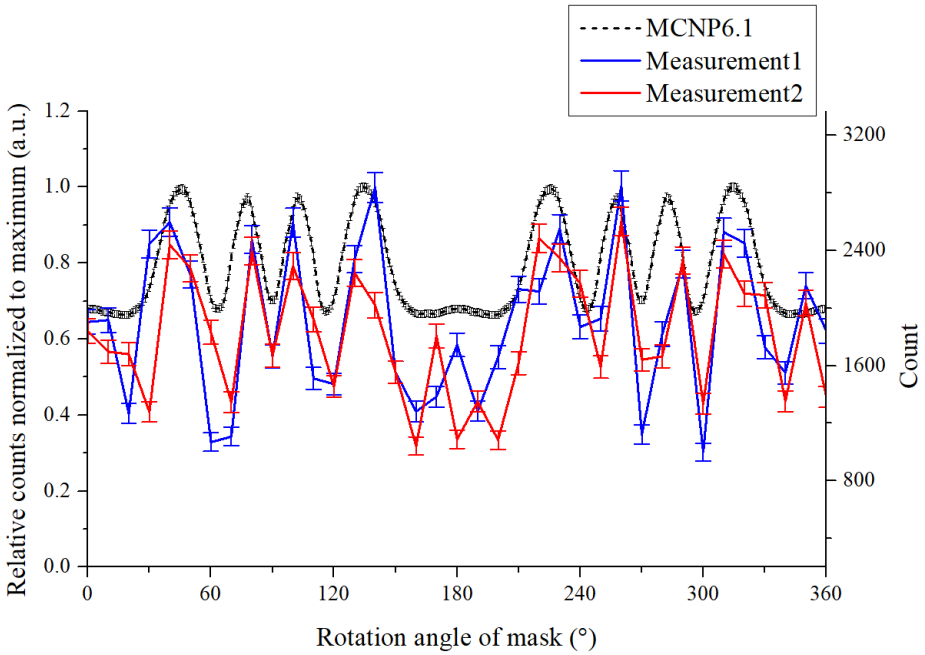

Figure 47. Modulation patterns obtained from the full-energy absorption peak area of 356 keV gamma ray. A 393.7 kBq single ^{133}Ba source was at (25 cm, 30°, 180°).

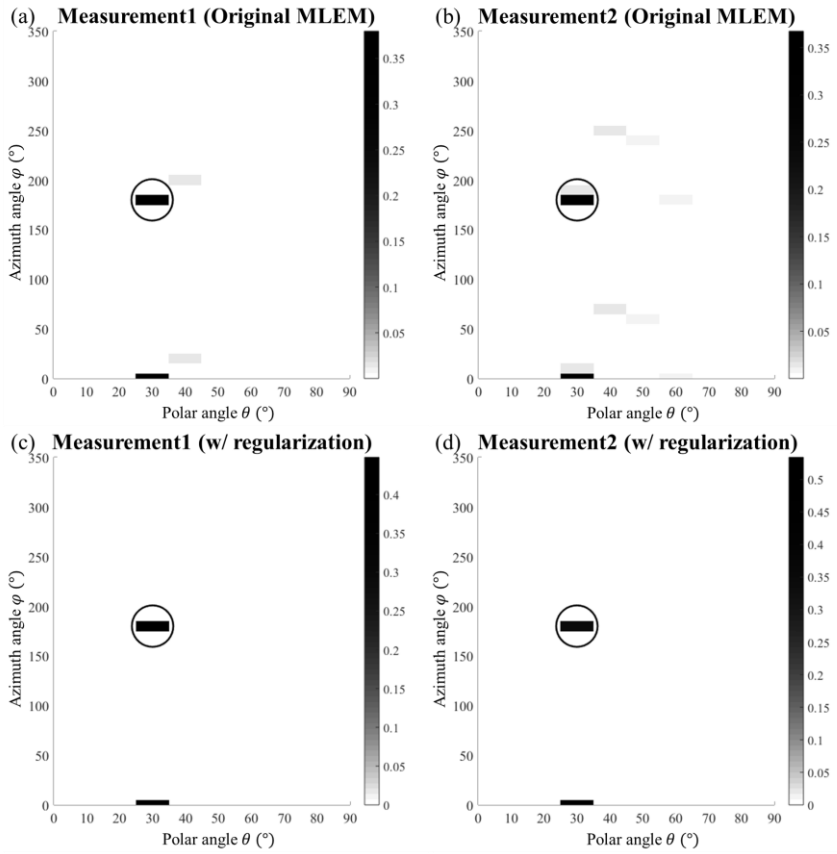

Figure 48. Reconstructed images of measured modulation patterns in Figure 47: (a) measurement1 (original MLEM), (b) measurement2 (original MLEM), (c) measurement1 (MLEM with regularization) and (d) measurement2 (MLEM with regularization).

3.2.3. Localization of Double Gamma-ray Sources

For further evaluation, a double source configuration of two radionuclides together was investigated to test whether they could be visualized in the reconstructed images. Figure 49 shows the modulation pattern when the R-type ^{133}Ba source and D-type ^{137}Cs source were simultaneously used, and error bars indicate 95% confidence intervals of each result. The dwell time was set to 60 minutes with a rotation interval of 10°. The ^{133}Ba source was located at (25 cm, 30°, 180°), the measured modulation pattern showed the similar trend with the MCNP6.1 simulation result (see Figure 49 (a)). However, when ^{137}Cs was located at (25 cm, 40°, 60°), there was a large difference between the measured and simulation results (see Figure 49 (b)). Although there was such a morphological difference in the modulation patterns constructed for the 662 keV peak, the corresponding rotation angles of the maximum and minimum points in both patterns coincided well with each other. Reconstructed images obtained with each measured modulation pattern (Figure 50) are shown in Figure 50, where original-MLEM-based images showed more artifact than the result of the single source case. Although the MLEM with regularization had intrinsic artifacts (i.e., symmetric points), other artifacts were significantly reduced. Therefore, the evaluated performance is superior using regularization were superior to the original, as summarized in Table 20.

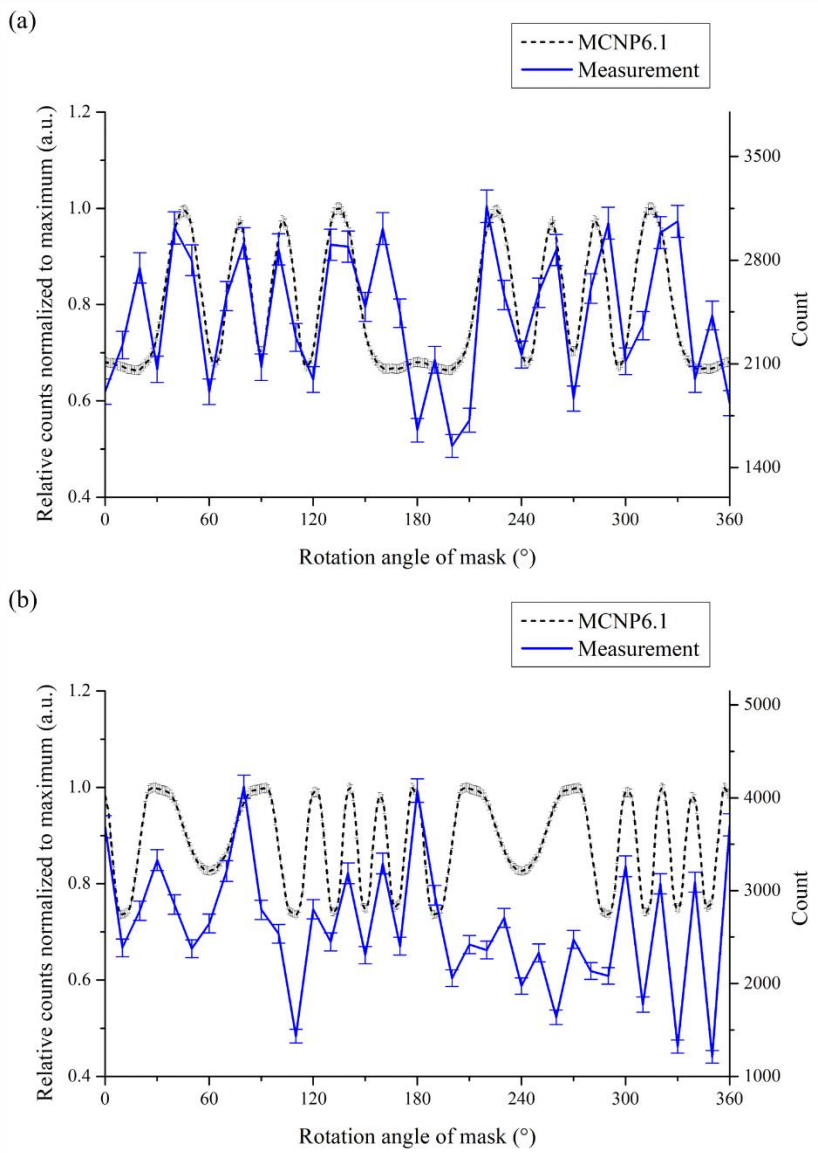

Figure 49. Comparison of modulation patterns obtained by measurement and MCNP6.1. Case1: 393.7 kBq ^{133}Ba position at (25 cm, 30°, 180°) and 962.4 kBq ^{137}Cs (25 cm, 40°, 60°): (a) full-energy absorption peak area of 356 keV gamma ray and (b) full-energy absorption peak area of 662 keV.

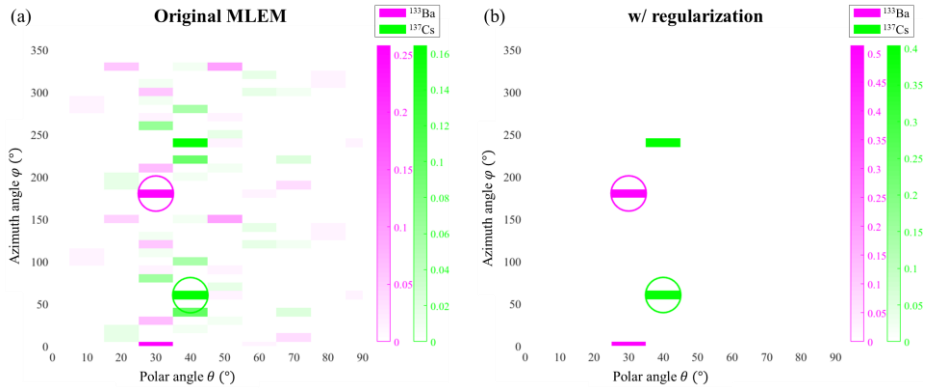

Figure 50. Reconstructed images of measured modulation patterns in Figure 49: (a) original MLEM, (b) MLEM with regularization.

In the second case, the imager was tested with the same radionuclide located at different positions. Two ^{133}Ba sources of 3312.2 kBq and 393.7 kBq were located at (25 cm, 40°, 30°) and (15 cm, 30°, 180°), and the dwell time was set to 40 minutes. Considering the actual source activity and radial distance (r) of each source, the gamma-ray intensity arriving at the detector from one source is calculated to be 3.53 times stronger than one from the other. This means that the number of particles emitted from (25 cm, 40°, 30°) reaching the H-RMC system is 3.53 times more than the number of particles emitted from (15 cm, 30°, 180°). As shown in Figure 51, the maximum and minimum points on the measured modulation pattern almost match with the MCNP6.1 results. Figure 52 also reflected the difference in the intensity between the two sources. Thus, the source intensity ratio could be confirmed by the MLE value estimated from the reconstruction algorithm. The ratio of the estimated MLE values for the two sources at different locations was 4.19 in the MLEM with regularization. Therefore, even if several radioactive materials are mixed, the relative intensity ratio of each radioactive material could be estimated by comparing the MLE values.

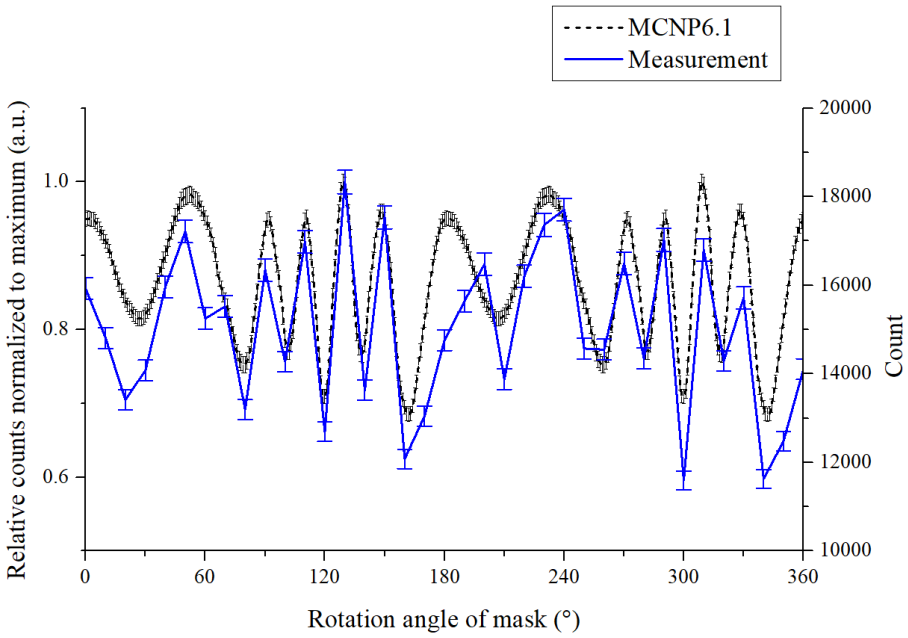

Figure 51. Modulation patterns obtained from the full-energy absorption peak area of 356 keV gamma ray. Case2: 3312.2 kBq ^{133}Ba position at (25 cm, 40°, 30°) and 393.7 kBq ^{133}Ba at (15 cm, 30°, 180°).

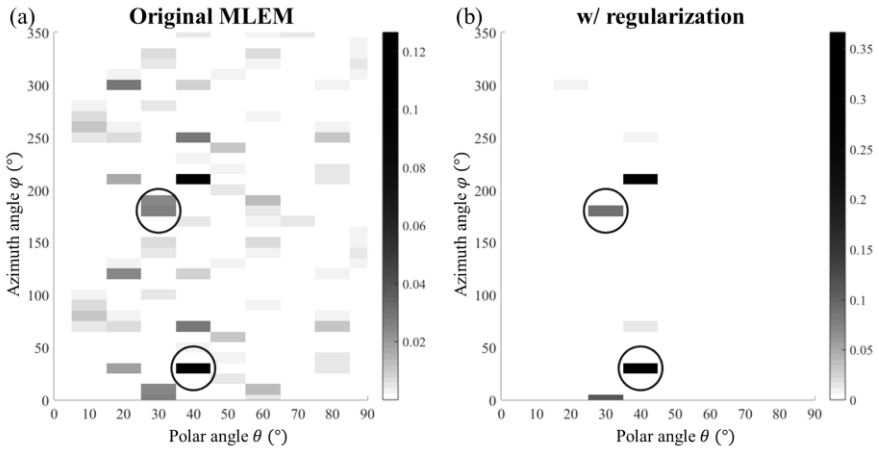

Figure 52. Reconstructed images of measured modulation patterns in Figure 51: (a) original MLEM and (b) MLEM with regularization.

Table 20. The signal-to-noise ratio (SNR) and structural similarity (SSIM) index results calculated for each case shown in Figure 50 and Figure 52

Double source environment	SNR		SSIM	
	Original MLEM	MLEM with regularization	Original MLEM	MLEM with regularization
Case1 (356 keV image)	19.07	25.83	0.92	0.97
Case1 (662 keV image)	14.73	21.09	0.94	0.96
Case2 (356 keV image)	9.26	18.76	0.88	0.92

3.2.4. Localization of Complex Gamma-ray Environment

By adding a ^{137}Cs source of 962.4 kBq to the dual source configuration of two ^{133}Ba sources, the H-RMC system was tested in a more complex radiation environment. The dwell time was set to 40 minutes and the rotation interval of mask was 10°. Figure 53 shows the modulation pattern obtained when two ^{133}Ba sources of different activity and distance (r) and a ^{137}Cs source were mixed. The error bars in the modulation patterns indicate 95% confidence intervals. The measured modulation pattern constructed for the 356 keV full-energy photopeak was very similar trend to the MCNP6.1 result; maximum and minimum points on the measured patterns approximately matched with simulated patterns as shown in Figure 53 (a).

However, in case of the modulation patterns constructed for 662 keV, there existed a large discrepancy between the measured patterns and the simulated patterns as shown in Figure 53 (b). In fact, the modulation efficiency of the 662 keV pattern is ~1.3 times lower that of 356 keV patterns due to the difference in the shielding performance of collimator masks. When modulation efficiency is smaller, it requires more counts to obtain a clear pattern, because the maxima and the minima points in the modulation patterns could be similar numbers in recorded counts. Therefore, if the radiation source has a higher activity or if we measure the source with a longer dwell time, the difference in pattern

morphology between measure and simulated patterns could also be reduced.

Nevertheless, the actual source position was estimated correctly as a point having the largest MLE value using the MLEM algorithm. Further, the MLEM algorithm with regularization technique was able to obtain very clear 2-D radiation distribution with artifact removed. The results are summarized in Table 21. In addition, the ratio of the MLE values of the two source points in Figure 54 (b) was 2.98, which was similar to the intensity ratio of 3.53 from the actual source. Therefore, using the developed system, the position of the radiation sources could be accurately estimated even in a complex gamma-ray environment where multiple sources were present at the same time. However, the inherent ambiguity issue of the source position estimation due to the bilateral symmetric mask was observed in Figure 54.

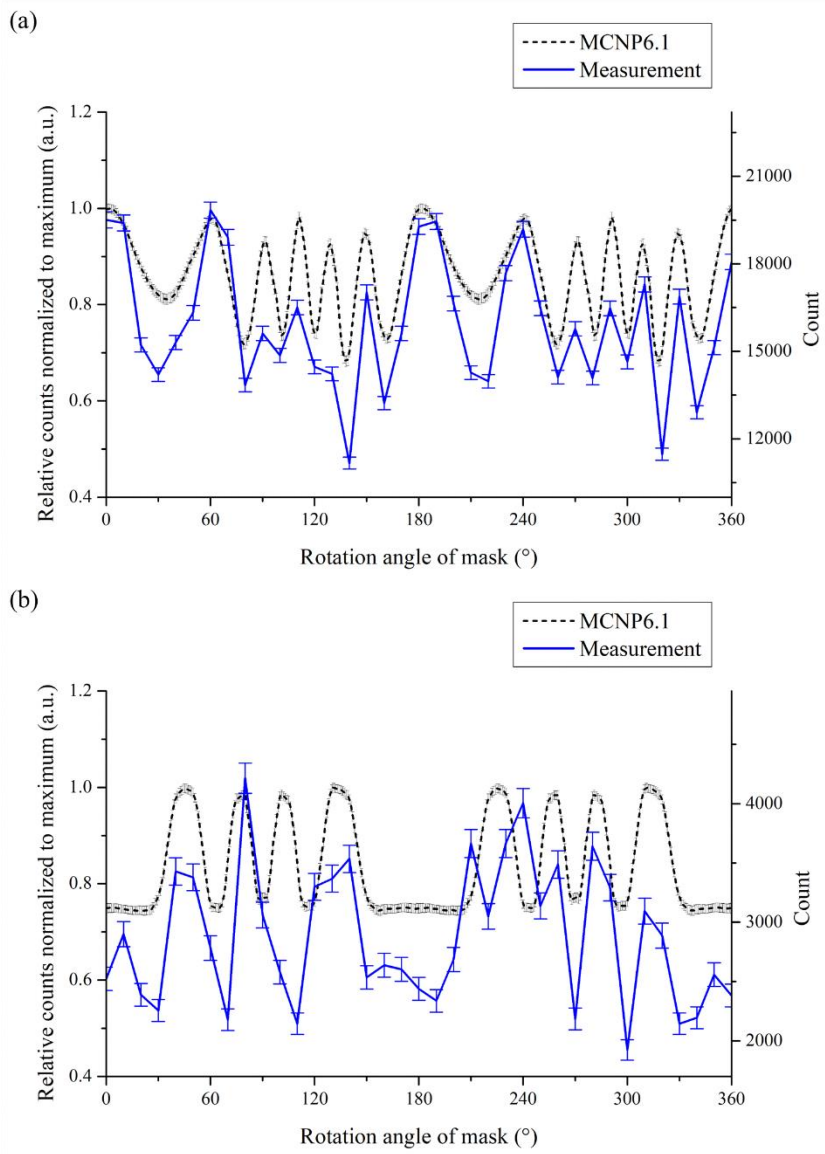

Figure 53. Modulation patterns obtained for 3312.2 kBq ^{133}Ba at (25 cm, 40°, 30°), 393.7 kBq ^{133}Ba at (15 cm, 20°, 180°) and 962.4 kBq ^{137}Cs at (20 cm, 30°, 180°) by calculating the full-energy absorption peak area of: (a) 356 keV and (b) 662 keV gamma rays.

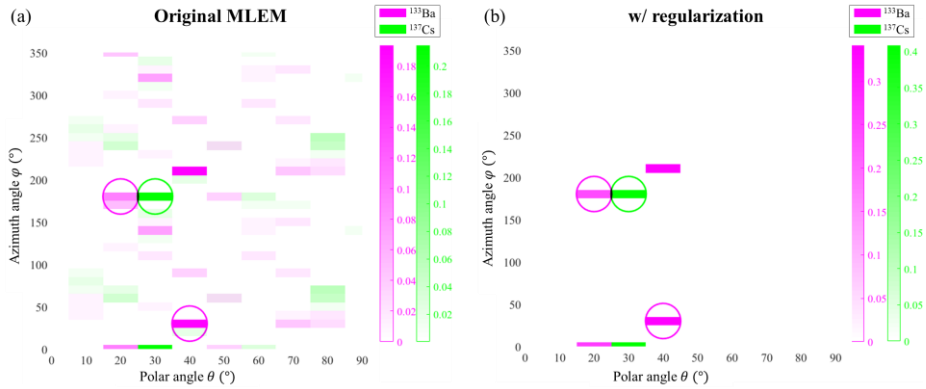

Figure 54. Reconstructed images of measured modulation patterns in Figure 53: (a) original MLEM, (b) MLEM with regularization.

Table 21. The signal-to-noise ratio (SNR) and structural similarity (SSIM) index results calculated for each case shown in Figure 54

Complex gamma-ray environment	SNR		SSIM	
	Original MLEM	MLEM with regularization	Original MLEM	MLEM with regularization
356 keV image	12.69	18.47	0.89	0.92
662 keV image	17.06	23.64	0.93	0.96

3.2.5. Imaging Dynamic Range

Since the RMC system indirectly estimates the source position based on modulation patterns, the dynamic range is closely related to the pattern morphology. If the magnitude of noise is greater than the effects of a weak source on the pattern, the weak source will not be distinguishable. Figure 55 shows simulated modulation patterns in accordance with the change of two ^{133}Ba source intensities. In this figure, a dashed line represents the patterns constructed by a strong source only, and solid lines represent the combined patterns of two ^{133}Ba sources together. Red circles shown in the Figure 55 represent the rotation angles, where the modulation patterns show the most distinctive difference of maxima points shifting from the original. When the relative intensity from the two ^{133}Ba sources was 2.45, the pattern morphology exhibited a distinct difference as large as 10° from the original pattern obtained by a single strong source only. However, when the relative intensity was 9.80, the combined pattern was difficult to distinguish clearly from that of strong source only.

In this regard, the MLEM with regularization approach may inevitably impose slight distortions on patterns in the process of noise suppression, even in the case that the alteration of the pattern is attributed to the true source activity instead of the background noise. The dynamic range of current system

under a specific condition was tested as indicated in Figure 55 and the relative intensity was determined by adjusting the radial distance of the weak source. It was confirmed experimentally that current system could distinguish two sources and estimate source positions correctly when the relative ratio of intensity from the two ^{133}Ba sources was less than 3.53 (see Figure 56). However, when the ratio was more than 3.53, the modulation pattern is primarily dominated by the stronger source, and very little alteration can be made on the modulation pattern by the weaker source. In this case, it is hard to identify the weak source unless a stronger source is found first and removed.

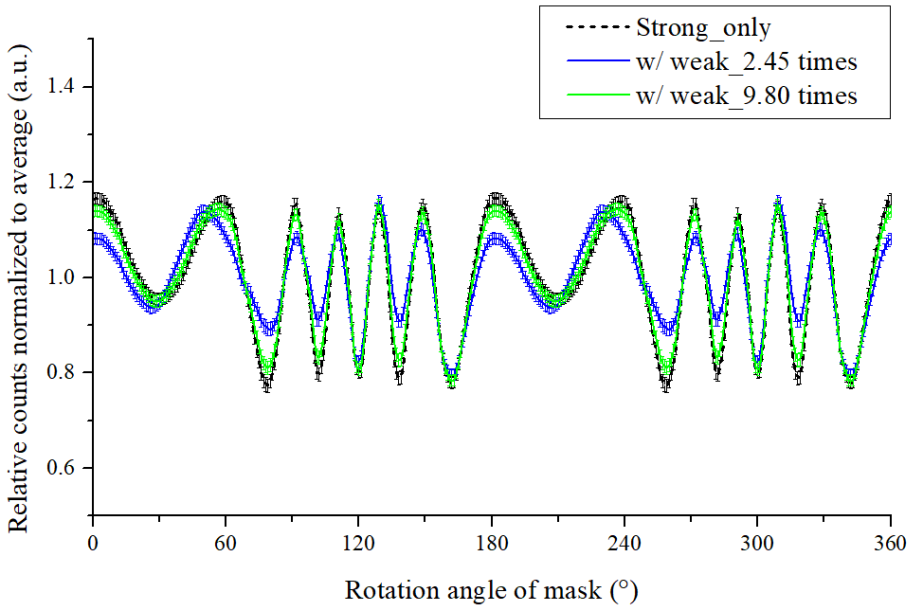

Figure 55. The morphological change of the patterns simulated by MCNP6.1 code. Strong_only indicates that a point source is located at (25 cm, 40°, 30°), and w/ weak_2.45 and 9.80 times indicate that another weak source is added at (25 cm, 30°, 180°).

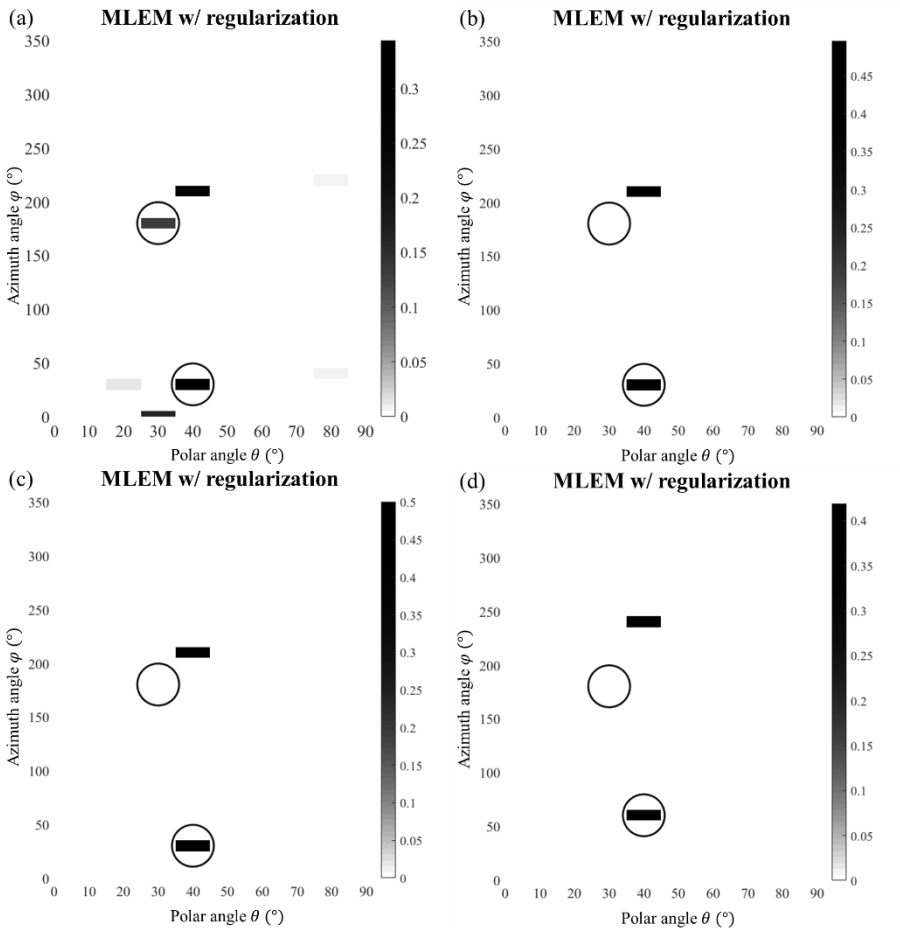

Figure 56. The performance of image reconstruction in accordance with change of two ^{133}Ba sources intensities: (a) 2.45 times, (b) 3.77 times, (c) 4.02 times and (d) intensity ratio of 9.80 times.

3.3. Additional Considerations for Practical Applications

The present chapter focuses on demonstrating the imaging capability of H-RMC system, and a novel hemispherical collimator design that could extend the FOV of 160° in the cross-sectional view. The specifications of the system are presented in the Table 22.

Table 22. Specifications of the H-RMC system (a)

Performance specification of radiation localization system		
Field of view	161° × 161° (cross-sectional view × longitudinal-sectional view)	
Angular resolution	10°	
Data acquisition time (sensitivity)	Localize point source of ^{133}Ba producing ~3 mR/hr in < 5 min	
CZT crystal size	1 cm × 1 cm × 1 cm (cube shape)	
Energy range	30 keV – 1.5 MeV	
Energy resolution	3.78% (@ 662 keV gamma ray)	
Intrinsic detection efficiency	356 keV	66.8%
	662 keV	22.8%

Table 23. Specifications of the H-RMC system (b)

System Specifications / Rotation Control System Performance	
Dimensions	61 cm × 61 cm × 40 cm
Weight	~30 kg (including detector)
Collimator	Stainless steel 303 alloy
Minimum rotation angle	1 °/step
Maximum rotation speed	6,000 r/min
Rated torque	0.16 Nm
Maximum torque	0.48 Nm
Rotation accuracy	< 0.1%
Power supply	External voltage 220 V (rotation control system)

One practical challenge one may encounter in the H-RMC system is the long detection time for constructing the modulation patterns due to the small activity of the source and detector size. Thus, further validation was performed by measurement experiment to check sensitivity of the H-RMC system. A ^{133}Ba gamma-ray source with an activity of 3312.2 kBq was used to check the morphology change in the modulation patterns according to the dwell time increase, and it was located at (25 cm, 30°, 180°) which producing 0.286 mR/hr at the H-RMC system. As shown in Figure 57, the shorter the dwell time, the greater the difference between the measurement and simulation results; however, if the measurement time is increased, the measured patterns became similar with the modulation pattern obtained in MCNP6.1. Nevertheless, reconstruction algorithm could estimate the source position correctly using modulation patterns in Figure 58 (a) even with 1 minute of dwell time. In addition, as shown in Figure 58, both algorithms estimated source position correctly, and the MLEM with regularization shows an artifact-free image that can clearly recognize the true source position. However, if the dwell time was reduced to less than 1 minute, appropriate patterns could not be obtained due to small detector size, and reconstruction algorithm estimates the wrong source position. Thus, by using the experimental results to calculate the sensitivity (i.e. 1 minutes of dwell time), the H-RMC system was found to be able to localize

a ^{133}Ba point source producing around 0.3 mR/hr within 40 minutes and its required time can be reduced proportionally with the exposure rate.

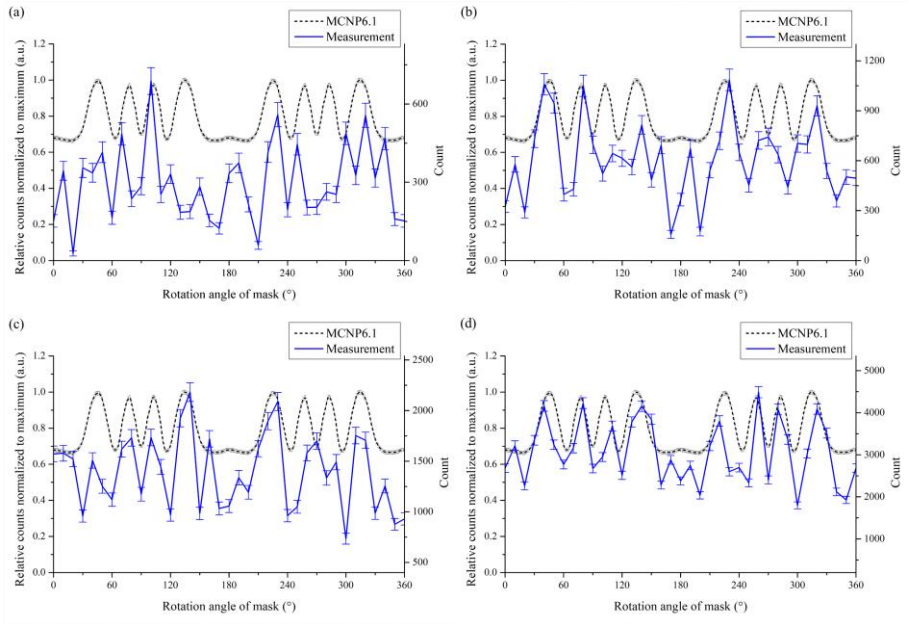

Figure 57. The morphology change in the measured with the increase of dwell time: (a) 1 min, (b) 2 min, (c) 5 min and (d) 10 min dwell time at each rotation condition.

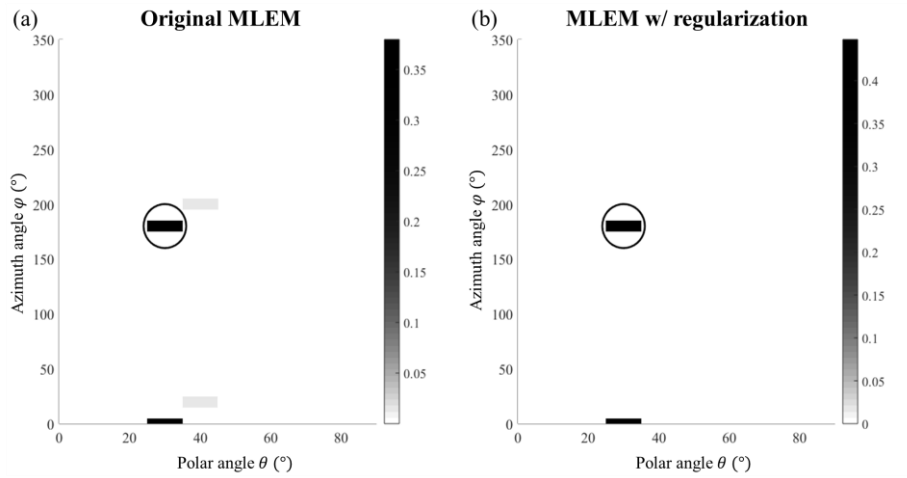

Figure 58. Reconstructed images of measured modulation patterns in Figure 57 (a): (a) original MLEM and (b) MLEM with regularization.

Another challenge in current system is the ambiguity issue of not being able to tell the exact source location between two symmetrically located points, one of which becomes an intrinsic artifact in the reconstructed image. As shown in Figure 59 (a), two symmetric sources located on the modulation patterns are indistinguishable, and this ambiguity can be explained by the periodicity of patterns and the fundamental characteristic of modulation patterns in RMC [23]. Using bilateral symmetric slat and slit configuration in the mask, the period of modulation patterns was 180°. In addition, rotational shift of the source location while keeping the source-to-axis distance the same (i.e. azimuth angle change) will cause a parallel translation of the modulation pattern in angular domain with respect to the rotation angle of the source. Therefore, two symmetric sources located with respect to the rotation axis such as (50 cm, 30°, 0°) and (50 cm, 30°, 180°) will show exactly the same pattern with each other. In fact, even though there exists 180° ambiguity, it can be resolved by making a second measurement at a different position [25]. Moreover, further improvements can be possible if masks have asymmetric slat/slit configuration. Introducing an asymmetric mask design can overcome the challenge given by the present symmetric mask design without compromising the imaging capability. Figure 59 (b) shows the simulated modulation patterns using asymmetric H-RMC system, which rotated the direction of half of the slits of the mask by 90°. With

asymmetric mask, the modulation patterns exhibit the 360° periodicity for the entire rotation, enabling estimation of source position without ambiguity. Therefore, reconstruction algorithm can distinguish modulation patterns in two symmetrically located source positions correctly (see Figure 59 (c) and (d)), and further improvements on the H-RMC system can be expected by applying the asymmetric design.

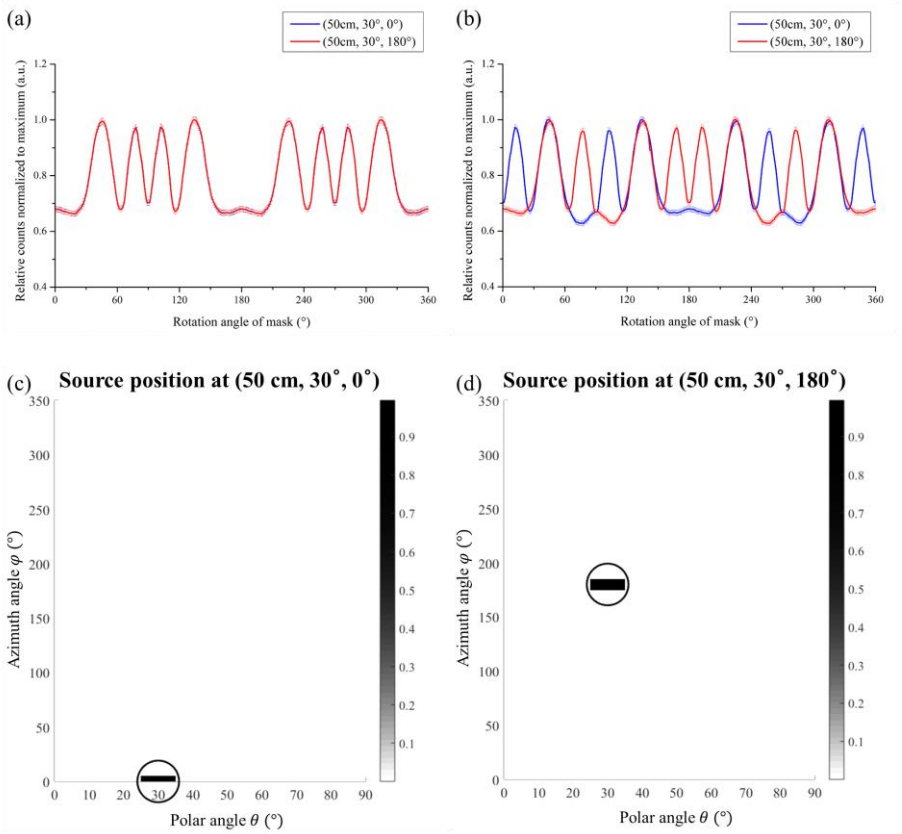

Figure 59. Modulation patterns obtained from MCNP6.1 and their reconstructed images: (a) modulation patterns of symmetric H-RMC system, (b) modulation patterns of asymmetric H-RMC system, (c) and (d) reconstruction images of simulated patterns in (b).

Chapter 4. Conclusion

To further promote the conventional RMC technique, a few enhancements 1) dual-particle localization system and 2) hemispherical collimator—were developed. The RMC system coupled with PSD capable scintillation detector was demonstrated to localize neutron/gamma-ray sources simultaneously. It offered an angular resolution 0.95° and FOV of 18° in the cross-sectional plane. The proposed RMC system could compensate drawbacks of radiation imagers based on the detection of one type of particle only. Furthermore, as a pioneering study on the extension of FOV in the RMC system, a hemispherical RMC system was developed using a CZT detector. It was observed to have a FOV of approximately 160° in the cross-sectional plane and an angular resolution of 10°. Experiments performed in a complex environment involving a few gamma sources placed at different locations were successful in localizing the source site of radioactive materials, and the results demonstrated the imaging capability of H-RMC system. In addition, the MLEM algorithm with regularization technique was validated experimentally by reconstructing images with improved performances compared to the original MLEM. This indicated that developed systems could also be utilized as a practical way to detect radioactive materials in a high-noise environment. Furthermore, since the developed systems can be combined with the various radiation detectors, it could be easily modified to a different modality used for various applications. The RMC-based localization system can be a useful tool in providing an approximate but economical-first-line detection for radioactivity compared with other localization system, thus, it can be utilized for various applications.

REFERENCES

[1] V. Burtniak, Yu. Zabulonov, M. Stokolos, L. Bulavin and V. Krasnoholovets, "The Remote Radiation Monitoring of Highly Radioactive Sports in the Chornobyl Exclusion Zone," *J. Intell. Robot Syst.*, vol. 90, pp. 437-442, 2018.

[2] Wenting Bu, Youyi Ni, Georg Steinhauser, Wang Zheng, Jian Zheng and Naoki Furuta, "The role of mass spectrometry in radioactive contamination assessment after the Fukushima nuclear accident," *J. Anal. At. Spectrom.*, vol. 33, pp. 519-546, 2018.

[3] D. Tomono, T. Mizumoto, A. Takada, S. Komura, Y. Matsuoka, Y. Mizumura, M. Oda and T. Tanimori, "First On-Site True Gamma-Ray Imaging-Spectroscopy of Contamination near Fukushima," *Sci. Rep.* vol. 7, pp. 1-10, 2017.

[4] I. Tsitsimpelisa, C.J. Taylora, B. Lennox and M. J. Joycea, "A review of ground-based robotic systems for the characterization of nuclear environments," *Prog. Nucl. Energy*, vol. 111, pp. 109-124, 2019.

[5] P.G. Martin, J. Moore, J.S. Fardoulis, O.D. Payton and T.B. Scott, "Radiological Assessment on Interest Areas on the Sellafield Nuclear Site via Unmanned Aerial Vehicle," *Remote Sens*., vol. 913, pp. 1-10, 2016.

[6] P.T Durrant, M. Dallimore, I.D Jupp and D. Ramsden, "The application of pinhole and coded aperture imagingin the nuclear environment," *Nucl. Instr. and Meth. A*, vol. 422, pp. 667-671, 1999.

[7] J.E. McKisson, P.S. Haskins, G.W. Phillips, S.E. King, R.A. August, R.B. Piercey and R.C. Mania, "Demonstration of Three-Dimensional Imaging with a Germanium Compton Camera," *IEEE Trans. Nucl. Sci*. vol. 41, pp. 1221-1224, 1994.

[8] C.J. Baek, S.J. Lee, Y. Choi and Y.H. Chung, "Optimization of Large-Angle Pinhole Collimator for Environmental Monitoring System," *IEEE Trans. Nucl.*

Sci, vol. 57, pp. 1404-1408, 2010.

[9] C.G. Wahl, W.R. Kaye, W. Wang, F. Zhang, J.M. Jaworski, A. King, Y.A. Boucher and Z. He, "The Polaris-H imaging spectrometer," *Nucl. Instr. and Meth. A*, vol. 784, pp. 377-381, 2015.

[10] M. Gmar, M. Agelou, F. Carrel and V. Schoepff, "GAMPIX: A new generation of gamma camera," *Nucl. Instr. and Meth. A*, vol. 652, pp. 638-640, 2011.

[11] H.O. Anger, "Scintillation Camera,' *Rev. Sci. Instrum*., vol. 29, pp. 27-33, 1958.

[12] G.A. Kastis, H.B. Barber, H.H. Barrett, S.J. Balzer, D. Lu, D.G. Marks, G. Stevenson, J.M. Woolfenden, M. Appleby and J. Tueller, "Gamma-Ray Imaging Using a CdZnTe Pixel Array and a High-Resolution, Parallel-Hole Collimator," *IEEE Trans. Nucl. Sci*, vol. 47, pp. 1923-1927, 2000.

[13] O. Gal, M. Gmar, O.P. Ivanov, F. Laine, F. Lamadie, C.L. Goaller, C. Mahe, E. Manach, V.E. Stepanov, "Development of a portable gamma camera with coded aperture," *Nucl. Instr. and Meth. A*, vol. 563, pp. 233-237, 2006.

[14] B.S. Budden, G.L. Case, M.L. Chery, "Angular resolution obtained with a $LaBr_3$-based rotational modulator," *in Conf. SPIE*, San Diego, CA, 2009, pp. 1-10.

[15] B.S. Budden, G.L. Case, M.L. Chery, "Image reconstruction with a $LaBr_3$-based rotational modulator," *Nucl. Instr. and Meth. A*, vol. 652, pp. 610-614, 2011.

[16] E.E. Fenimore and T.M. Cannon, "Coded aperture imaging with uniformly redundant arrays," *Appl. Opt.* vol. 17, pp. 337-347, 1978.

[17] S.R. Gottesman and E.E. Fenimore, "New family of binary arrays for coded aperture imaging," *Appl. Opt.* vol. 20, pp. 4344-4352, 1989.

[18] W.R. Cook, M. Finger, T. A. Prince and E.C. Stone, “Gamma-Ray Imaging with a Rotating Hexagonal Uniformly Redundant Array,” *IEEE Trans. Nucl. Sci*, vol. 31, pp. 771-775, 1984.

[19] J.E.M. Goldsmitha, M.D. Gerling and J.S. Brennan, “A compact neutron scatter camera for field deployment,” *Rev. Sci. Instrum*., vol. 87, pp. 1-9, 2016.

[20] A. Poitrasson-Rivièren, M.C. Hamel, J.K. Polack, M. Flaska, S.D. Clarke and S.A. Pozzi, “Dual-particle imaging system based on simultaneous detectionof photon and neutron collision events,” *Nucl. Instr. and Meth. A*, vol. 760, pp. 40-45, 2014.

[21] MIRION, iPIX datasheet, 2019. [Online] Available: https://mirion.s3.amazonaws.com/cms4_mirion/files/pdf/spec-sheets/doc010883en-d_ipix-ultra-portable-gamma-ray-imaging-system.pdf?1556197349

[22] H3D, H400 datasheet, 2019. [Online] Available: https://h3dgamma.com/H400Specs.pdf?

[23] H.S. Kim, Y. Shin, G. Lee, S.J. Ye and G. Kim, “Radiation imaging with rotational modulation collimator (RMC) coupled to a Cs_2LiYCl_6:Ce (CLYC) detector,” *J. Korean Phys. Soc*., vol. 69, pp. 1644-1650, 2016.

[24] M. Oda, “High-Resolution X-Ray Collimator with Broad Field of View for Astronomical Use,” Appl. Opt., vol. 4, pp. 143, 1965.

[25] H.W. Schnopper, R.I. Thompson and S. Watt, “Predicted Performance of a Rotating Modulation Collimator for Locating Celestial X-Ray Sources,” *Space Sci. Rev*., vol. 8, pp. 534-542, 1968.

[26] H.W. Schnopper, H.V. Bradt., S. Rappaport, E. Boughan, B. Burnett, R. Doxsey, W. Mayer and S. Watt, “Precise Location of Sagittarius X-Ray Sources with a Rocket-Borne Rotating Modulation Collimator,” *Astrophys. J*., vol. 161,

pp. 161-167, 1970.

[27] A.M. Cruise and A.P. Willmore, “The Analysis of Data from Rotation Modulation Collimators” *Mon. Notices Royal Astron. Soc*., vol. 70, pp. 165-175, 1975.

[28] K. Makishima, S. Miyamoto, T. Murakami, J. Nishimura, M. Oda, Y. Ogawara and Y. Tawara, “Modulation collimator as an imaging device,” *New instrum. space astron*., p. 277-289 1978.

[29] L.N. Mertz, G.H. Nakano and J.R. Kilner, “Rotational aperture synthesis for x rays,” *J. Opt. Soc. Am. A*, vol. 3, pp. 2167-2170, 1986.

[30] T.R. Fisher, J.W. Hamilton, J.D. Hawley, J.R. Kilner, M.J. Murphy and G.H. Nakanon, “Imaging of Gamma Rays with the WINKLER High-Resolution Germanium Spectrometer,” *IEEE Trans. Nucl. Sci*, vol. 37, pp. 1483-1488, 1990.

[31] G.J. Hurford et al., “The RHESSI Imaging Concept,” *Solar Phys*., vol. 210, pp. 61-86, 2002.

[32] A. C. Sharma et al., “Design and Development of a High-Energy Gamma Camera for Use with NSECT-Imaging: Feasibility for Breast Imaging,” *IEEE Trans. Nucl. Sci.* vol. 54, pp. 1498-1505, 2007.

[33] B.R. Kowash, D.K. Wehe and J.A. Fessler, “A rotating modulation imager for locating mid-range point sources,” *Nucl. Instr. and Meth. A*, vol. 602, pp. 477-483, 2009.

[34] B.R. Kowash and D.K. Wehe, “A unified near-and far-field imaging model for rotating modulation collimators,” *Nucl. Instr. and Meth. A*, vol. 637, pp. 178-184, 2011.

[35] Nathan O. Boyce, “Thermal neutron point source imaging using a rotating modulation collimator (RMC),” M.S. thesis, Dept. Eng. Phys., Air Force

Institute of Technology Air University, OH, USA, 2010.

[36] D.T. Willcox, “Adaptive Imaging Methods using a Rotating Modulation Collimator (RMC),” M.S. thesis, Dept. Eng. Phys., Air Force Institute of Technology Air University, OH, USA, 2011.

[37] J. Glodo, R. Hawrami, and K.S. Shah, “Development of Cs_2LiYCl_6 scintillator,” *J. Crys., Grow*., vol. 379, pp. 73-78, 2013.

[38] H.S. Kim, M.B. Smith, M.R. Koslowsky, S.W. Kwak, S.J. Ye and G. Kim, “Characterization of a CLYC Detector and Validation of the Monte Carlo Simulation by Measurement Experiments,” *J. Radiat. Prot. Res*., vol. 42, 48-55, 2017.

[39] M.B. Smith, T. Achtzehn, H.R. Andrews, E.T.H. Clifford, H. Ing, and V.D. Kovaltchouk, “Fast Neutron Spectroscopy Using Cs_2LiYCl_6:Ce (CLYC) Scintillator,” *IEEE Trans. Nucl. Sci*. vol. 60, pp. 855-859, 2013.

[40] T. Goorley et al., “Initial MCNP6 Release Overview,” *Nucl. Technol*. vol. 180, pp. 298-315, 2012.

[41] U. Rizwan, A. Chester, T. Domingo, T. Starosta, J. Williams, P. Voss, “A method for establishing absolute full-energy peak efficiency and its confidence interval for HPGe detectors,” *Nucl. Instrum. Methods A*., vol. 802, pp. 102-112. 2015.

[42] B. S. McDonald, M. J. Myjak, W. K. Hensley, and J. E. Smart, “System Modeling and Design Optimization for a Next-Generation Unattended Sensor,” *IEEE Trans. Nucl. Sci*., vol. 60, pp. 1102-1106, 2013.

[43] J.M. Verbeke, C. Hagmann, D. Wriht, “Simulation of Neutron and Gamma Ray Emission from Fission and Photofission,” Lawrence Livermore National Laboratory, Livermore, CA, UCRL-AR-228518, 2014.

[44] M.M. Bourne, C. Mussi, E.C. Miller, S.D. Clarke, P. A. Pozzi and A.

Gueorguiev, “Characterization of the CLYC detector for neutron and photon detection,” *Nucl. Instrum. Methods A*., vol. 736, pp. 124-127, 2014.

[45] H.S. Kim, H.Y. Choi, G. Lee, S.J. Ye, M. B. Smith, G. Kim, “A Monte Carlo Simulation Study for the Gamma-Ray/Neutron Dual-Particle Imager using Rotational Modulation Collimator (RMC),” *J. Radiol. Prot*., vol. 38, pp. 299-399, 2018.

[46] H.S Kim, S.J. Ye, G. Lee and G. Kim, “Optimization of the Collimator Mask for the Rotational Modulation Collimator-based Gamma-Ray/Neutron Dual-Particle Imager,” *Curr. Appl. Phys*., vol. 19, pp. 856-865, 2019.

[47] Y. Shin, G. Kim and G. Lee, “Regularizing RMC images for locating mid-range point sources,” *JINST*, vol. 11, pp. 1-8, 2016.

[48] R.C. Gonzalez, R.E. Woods, “Image error measures,” in Digital Image Processing, 3rd ed., NY, USA: John Wiley & Sons, Inc., 2007, pp. 715-716.

[49] Z. Wang, A.C. Bovik, H.R. Sheikh and E.P. Simoncelli, “Image Quality Assessment: From Error Visibility to Structural Similarity,” *IEEE Trans. Image Proc*., vol. 13, pp. 600-612. 2004.

[50] M. Na, S. Lee, G. Kim, H.S. Kim, J. Rho and J.G. Ok, “Development of a hemispherical rotational modulation collimator system for imaging spatial distribution of radiation sources,” *JINST*, vol. 12, pp. 1-7, 2017.

Abstract (in Korean)

국 문 초 록

회전 변조 집속기 기반 영상화 기술은 기계적 집속을 이용하는 기법 중 하나로 단일 검출기 앞에서 동시에 회전하는 두 개의 집속기로 구성된다. 이 기술은 위치 민감형 검출기가 필요 없기 때문에 시스템의 복잡성과 비용을 줄일 수 있는 장점이 있다. 그러나 기존의 회전 변조 집속기 기법은 단일 입자 영상화만 가능하였고, 원기둥 형태의 구조로 인해 시야각이 좁은 한계점이 있었다. 본 학위논문은 회전 변조 집속기 기법에 대한 추가적인 탐구를 목표로 하여, 크게 두 가지 측면에서 회전 변조 집속기 영상화 기법을 개선하였다. 그 첫 번째 연구 내용으로서, 회전 변조 집속기 기법에 신호 파형 구분법이 적용 가능한 섬광 계측기를 접목하여 중성자와 감마선을 동시에 탐지할 수 있는 이중입자 위치 추정 시스템을 계발하였다. 몬테 카를로 전산 모사를 이용하여 설계 파라미터를 최적화하였고, 기존의 좌우 대칭형태의 집속기 구조가 가지는 180° 대칭 위치의 선원 추정 모호성 문제를 해결하기 위해서 새로운 비대칭형 집속기를 제안하였다. 방사성 물질의 위치 추정을 위해서 최대 우도 추정 기댓값 극대화 기법에 기반한 영상 재구성 방법론을 확립하였고, 개발된 장비의 영상화 능력은 측정 실험을

통해 검증되었다. 개발된 이중입자 위치 추정 시스템의 각 분해능은 0.95° 이고, 시야각은 시스템의 횡단면을 기준으로 18° 이다. 두 번째 연구 내용으로서, 일반적인 회전 변조 집속기 디자인의 좁은 시야각 문제를 해결하기 위해 반구 형태의 집속기 디자인을 개발하였다. 몬테 카를로 전산 모사를 이용하여 설계 파라미터를 최적화하였고, 최대 우도 추정 기댓값 극대화 기법에 기반한 영상 재구성 방법론을 적용하여 방사성 물질의 분포를 추정하였다. 시스템의 영상화 능력을 평가하기 위해 측정 실험을 수행하였으며, 개발된 반구형 회전 변조 집속기는 설계되고 시뮬레이션된 것처럼 유효한 것을 확인하였다. 시스템의 시야각은 횡단면을 기준으로 160° 이고 각 분해능은 10° 이다. 결론적으로, 본 연구를 통해 회전 변조 집속기 기법은 이중입자 위치 추정 시스템으로 개선되었으며, 시야각을 약 2π 영역까지 확장시킬 수 있는 방법이 제안되었다. 이러한 개선점이 회전 변조 집속기 기법에 적용된다면 회전 변조 집속기 기반 영상화 시스템이 방사선 안전 및 핵안보 분야에서 보다 실용적이고 유용하게 활용될 수 있을 것이라 기대한다.

주요어: 회전 변조 집속기, 중성자/감마선원 위치 추정, 신호 파형 구분법, 반구형 회전 변조 집속기, 최대 우도 추정 기댓값 극대화

학 번: 2013-23762